

ABSTRACT

Title of Dissertation: Application of Plasmon Resonances to Surface Enhanced Raman Scattering (SERS), Heat-Assisted Magnetic Recording (HAMR), and All-Optical Magnetic Recording

Ling Hung, Doctor of Philosophy, 2013

Dissertation directed by: Professor Isaak Mayergoyz
Department of Electrical and Computer Engineering,
UMIACS and AppEl Center

In this work, we perform the analytical and numerical analyses of the plasmon modes in different metallic nanostructures for the applications to surface-enhanced Raman scattering (SERS), heat-assisted magnetic recording (HAMR) and all-optical magnetic recording. We start with the introduction of physical origin of plasmon resonances in nanoparticles and the eigenmode analysis technique adopted throughout this work in Chap. 1. The excitation of the plasmon modes in nanoparticles subject to optical radiation is also presented. In Chap. 2, we study the dispersion in the SERS enhancement factors with silver nanocube dimers. We perform the mode analysis and calculated the resonance wavelengths of the dipolar plasmon modes in silver nanocube dimers with different configurations. The results show that the SERS enhancement factors are related to the resonance frequencies of the dimers, which are determined by their gap distances and orientations. In Chap. 3, we analytically derive the formula for the computation of resonance permittivities of

plasmon modes in spheroidal nanoshells. The dipolar plasmon modes in spheroidal nanoshells possess rotational symmetry which preserves the helicity of circularly polarized light, and consequently, they are useful in all-optical magnetic recording. We have also derived the formulas which indicate how the dipolar plasmon modes in ellipsoidal nanoshells can be excited by uniformly incident field. Light intensities of the optical spots generated by the circularly polarized plasmon modes in spherical nanoshells are computed and compared with those generated by circularly polarized plasmon modes in spheroidal nanoshells. In Chap. 4, we study the plasmon resonances in T-shaped aperture metallic nanofilms and lollipop metallic nanodisks placed nearby different dielectric substrates used in heat-assisted magnetic recording. We developed a constrained eigenvalue problem for specific coupled boundary integral equations to take into account the effect of the surrounding finite dielectric objects. By solving this problem, the resonance frequencies of such metallic nanostructures as well as the corresponding plasmon modes can be computed. The effect of heat sink layers on the plasmon resonances is also discussed. Finally, in Chap. 5, we study the radiation corrections of plasmon resonances in nanoparticles. The red-shifts in resonance frequencies of dipolar plasmon modes with nanocube size are computed and compared with experimental measurement. The results suggest that different dipolar modes have different sensitivities to the rounding of the cube corners and edges.

Application of Plasmon Resonances to Surface Enhanced Raman
Scattering (SERS), Heat-Assisted Magnetic Recording(HAMR),
and All-Optical Magnetic Recording

by

Ling Hung

Dissertation submitted to the Faculty of the Graduate School of the
University of Maryland, College Park in partial fulfillment
of the requirements for the degree of
Doctor of Philosophy
2013

Advisory Committee:

Professor Isaak Mayergoyz, Chair/Advisor

Professor Oded Rabin

Professor Thomas E. Murphy

Professor Edo Waks

Professor Lourdes G. Salamanca-Riba, Dean's Representative

© Copyright by
Ling Hung
2013

Dedication

To my wife Xiaoshu and my parents.

Acknowledgments

First and foremost, I'd like to thank my advisor, Professor Isaak D. Mayergoyz, for giving me an invaluable opportunity to work on extremely interesting and challenging projects. For the past four years, Professor Mayergoyz has always made himself available for guide and advice, and there has never been an occasion when I got lost in the research and he was not there to give me support. It is from him that I learned the altitude and attitude of doing scientific research. It is also from him that I realized the importance of developing my own memory and conveying my knowledge clearly and concisely. It is my pleasure to work with and learn from such an extraordinary and outstanding individual. Thanks to Prof. Mayergoyz, I have overcome my disadvantages and weakness, and developed myself as a responsible and professional scientist. If I were to use a sentence to express my gratitude to him, I would say "If I have seen further and further, it is by standing on the shoulder of a giant."

I would also like to thank Professor Oded Rabin and his student Seung Yong Lee, especially Professor Rabin for providing invaluable insights and assistance into this work. This research thesis would not have been possible without their extraordinary experimental expertise. Thanks are due to Professor Thomas E. Murphy, Professor Edo Waks and Professor Lourdes G. Salamanca-Riba for agreeing to serve on my thesis committee and for sparing their invaluable time reviewing the manuscript.

My colleagues at the magnetics laboratory have enriched my graduate life in many ways and deserve a special mention. Garrett Lang introduced me the simu-

lation codes developed by Professor Mayergoyz's previous student Zhengyu Zhang. David Bowen assisted me in adapting my working environment in this lab. Ziyu Liu and Andrew Lee have provided their expertise in magnetization dynamics and the knowledge in GPU computing, which helped me understand my research more and increased my numerical computation speed significantly. I would also like to specially thank Dr. Patrick McAvoy, for sharing his abundant knowledge and experience in many areas. My discussions with him were always fruitful and inspired me in many aspects. I am also greatly thankful for his improvement of the manuscript of this dissertation.

I would like to convey my thanks to Steve Tjoa, who was extremely helpful to assist me in settling down my life in United States. I also would like to thank all my housemates at my past places of residence. They have been very supportive in many aspects in my daily life, and I cherish the friendships with them.

I would like to acknowledge Mr. Zhou-Huang Huang, chairman of Suyin Corporation. It was him that I had this opportunity to study abroad, experience a new life, and meet the people from all over the world. His support is greatly appreciated.

I owe my deepest thanks to my family - my mother and father who have always stood by me and guided me through my career, and have pulled me through against difficult moments at times.

Finally, I would like to express my deepest thanks to my wife Xiaoshu Zhu. Without her endless love, I would have not come this far and finished my PhD research. I thank her with my whole heart for her understanding, support, and company at all times. I am happy because of having you.

It is impossible to remember all, and I apologize to those I've inadvertently left out.

Table of Contents

| | |
|--|-----|
| Dedication | ii |
| Acknowledgements | iii |
| Table of Contents | vi |
| List of Tables | ix |
| List of Figures | x |
| 1 Plasmon Resonances in Nanoparticles | 1 |
| 1.1 The Physical Origin of Plasmon Resonance | 1 |
| 1.2 Analytical Solutions of Plasmon Resonances in Nanoparticles | 3 |
| 1.2.1 Example I: Two Adjacent Spherical Nanoparticles | 5 |
| 1.2.2 Example II: Toroidal Nano-rings | 12 |
| 1.3 Mode Analysis of the Plasmon Resonances in Nanoparticles | 16 |
| 1.4 Excitation of Plasmon Modes in Metallic Nanoparticles | 23 |
| 1.5 Computation of Extinction Cross Sections of Metallic Nanoparticles Subject to Optical Radiation | 26 |
| 1.6 Overview of Dissertation Contents | 30 |
| 2 Application of Plasmon Resonances to Surface-Enhanced Raman Scattering (SERS) | 33 |
| 2.1 Introduction | 33 |
| 2.2 Mode Analysis of AgNC Clusters | 35 |
| 2.2.1 Monomers | 35 |
| 2.2.2 Dimers | 38 |
| 2.3 Experimental Method | 41 |
| 2.3.1 Preparation of AgNC Clusters on Patterned Substrate | 41 |
| 2.3.2 Identification of the AgNC Clusters | 43 |
| 2.3.3 Raman Spectra Analysis and Calculation of the SERS Sub- strate Enhancement Factor | 44 |
| 2.4 Conclusion | 46 |
| 3 Application of Plasmon Resonances to All-optical Magnetic Recording | 50 |
| 3.1 Overview | 50 |
| 3.2 Introduction of Ellipsoidal Harmonics | 51 |
| 3.2.1 Ellipsoidal Coordinate System | 51 |
| 3.2.2 Lamé Equations and Lamé Functions | 52 |
| 3.2.3 Ellipsoidal Harmonics | 53 |
| 3.3 Boundary Value Problem in an Ellipsoidal Nanoshell | 54 |
| 3.3.1 Dipolar Plasmon Modes in an Ellipsoidal Nanoshell | 56 |
| 3.3.2 Excitation of the Dipolar Plasmon Modes in an Ellipsoidal Shell | 61 |

| | | |
|---------|--|-----|
| 3.3.2.1 | On-resonance excitation | 63 |
| 3.3.2.2 | Off-resonance excitation | 63 |
| 3.4 | Results and Discussion | 64 |
| 4 | Application of Plasmon Resonances to Heat-Assisted Magnetic Recording (HAMR) | 67 |
| 4.1 | Overview | 67 |
| 4.2 | Constrained Eigenvalue Problem | 70 |
| 4.3 | Results Discussion | 73 |
| 4.3.1 | T-shaped Apertures | 74 |
| 4.3.2 | Lollipop Nanodisks | 76 |
| 4.4 | Effect of Heat Sink Layers | 80 |
| 4.5 | Conclusions | 83 |
| 5 | Radiation Corrections for Plasmon Resonances in Nanoparticles | 87 |
| 5.1 | Introduction | 87 |
| 5.2 | Second-Order Corrections | 88 |
| 5.2.1 | Theoretical Modeling | 88 |
| 5.2.2 | Samples of Numerical Simulation Results | 90 |
| 5.3 | Dipolar Plasmon Modes in Silver Nanocubes | 94 |
| 5.3.1 | Experimental Measurement | 94 |
| 5.3.2 | Numerical Simulation | 96 |
| 5.4 | Results and Discussions | 100 |
| 6 | Conclusion and Future Work | 107 |
| A | Non-Uniform Excitation of Plasmon Resonances by a Single Molecule | 110 |
| | Bibliography | 122 |

List of Journal Publications

1. L. Hung, G. Lang, P. McAvoy, C. Krafft, I. Mayergoyz, “Circularly Polarized Plasmon Modes in Spheroidal Nanoshells for Applications to All-Optical Magnetic Recording,” *J. Appl. Phys.* Vol. 111, 07A915, 2012
2. G. Lang, D. Bowen, L. Hung, C. Krafft, I. Mayergoyz, “Anisotropy study of garnet films grown over substrates populated with gold nanoparticles,” *J. Appl. Phys.* Vol. 111, 07A505, 2012
3. S. Y. Lee, L. Hung, G. S. Lang, J. E. Cornett, I. D. Mayergoyz, O. Rabin, “Dispersion in the SERS Enhancement with Silver Nanocube Dimers,” *ACS NANO*, Vol. 4, Issue 2, pp. 5763-5772 (2010).
4. I. D. Mayergoyz, G. Lang, L. Hung, S. Tkachuk, C. Krafft, “Plasmon Resonance Enhancement of Magneto-optic Effects in Garnets,” *J. Appl. Phys.* Vol. 107, 09A925 (2010).

List of Conference Presentations

1. L. Hung, P. McAvoy, C. Krafft, I. Mayergoyz, “Analysis of Plasmon Resonances in Metallic nanostructures with Heat Sink Used in Heat-Assisted Magnetic Recording,” *12th Joint MMM/Intermag Conference* 2013.
2. L. Hung, G. Lang, P. McAvoy, C. Krafft, I. Mayergoyz, “Application of Plasmon Resonances in Metallic Nanostructures to Heat-Assisted Magnetic Recording,” *IEEE International Magnetism Conference (INTERMAG)* 2012.
3. L. Hung, G. Lang, P. McAvoy, C. Krafft, I. Mayergoyz, “Circularly Polarized Plasmon Modes in Spheroidal Nanoshells for Applications to All-Optical Magnetic Recording,” *56th Conference on Magnetism and Magnetic Materials (MMM)* 2011.
4. G. Lang, D. Bowen, L. Hung, C. Krafft, I. Mayergoyz, “Anisotropy study of garnet films grown over substrates populated with gold nanoparticles,” *56th Conference on Magnetism and Magnetic Materials (MMM)* 2011.

List of Tables

| | | |
|-----|---|-----|
| 2.1 | Calculated SERS enhancement factors for AgNC monomer on silicon for different incident wavelength and Raman scattering wavelength with different cube orientations. | 38 |
| 2.2 | Calculated resonance wavelengths for 80 nm silver nanocube dimers on silicon substrate. | 40 |
| 2.3 | Calculated SERS enhancement factors for 80 nm silver nanocube dimers on silicon substrate (Incident wavelength = 633 nm; scattered wavelength = 678 nm). | 40 |
| 2.4 | Details of assignment of the dimer type as EE, FE, or FF based on geometrical factors. | 43 |
| 2.5 | Parameters obtained from the Weibull distribution model. | 45 |
| 2.6 | Calculated resonance wavelengths and SERS enhancement factors for 100 nm silver nanocube face-to-face dimers on silicon (Incident wavelength = 514 nm; scattered wavelength = 560 nm). | 46 |
| 5.1 | Comparison for resonance wavelengths of gold nanorings placed on glass substrate. | 93 |
| 5.2 | Comparison for resonance wavelengths of silver nanocubes immersed in water. | 93 |
| 5.3 | Comparison for resonance wavelengths of silver nanocubes placed on glass substrate. | 93 |
| 5.4 | Calculated surface charge distributions for the eight strongest dipole plasmon modes and the corresponding resonance wavelengths for a single silver cube in water with 864 square patches. | 98 |
| 5.5 | Calculated surface charge distributions for the eight strongest dipole plasmon modes and the corresponding resonance wavelengths for a single silver cube in water with 38400 square patches. | 99 |
| 5.6 | Calculated resonance permittivities, resonance wavelengths, and dipole moments for dipolar modes D1-D8. | 102 |

List of Figures

| | | |
|------|--|----|
| 1.1 | Schematic illustration of total field inside a particle with (a) positive permittivity; (b) negative permittivity. | 2 |
| 1.2 | (a) Toroid after rotating along y-axis; (b) Bispheres after rotating along x-axis. | 5 |
| 1.3 | Schematic illustration of two spheres. | 5 |
| 1.4 | Schematic of a toroidal nano-ring. | 13 |
| 1.5 | The metallic nanoparticle bounded by surface S | 17 |
| 1.6 | Dispersion relation of gold measured by Johnson and Christy. | 19 |
| 1.7 | Dispersion relation of silver measured by Johnson and Christy. | 19 |
| 1.8 | Plasmon modes in toroids with $x_0/R = 10$: (a) $n = 0, m = 1$; (b) $n = 0, m = 2$; (c) $n = 0, m = 3$ | 22 |
| 1.9 | Comparison of resonance permittivities calculated by the eigenmode method and analytical solution for mode $m = 1, m = 2, m = 3$ ($n = 0$ for all). | 22 |
| 1.10 | The ratio of real to imaginary parts of dielectric permittivity of silver. | 25 |
| 1.11 | The ratio of real to imaginary parts of dielectric permittivity of gold. | 25 |
| 1.12 | Computed $C(\omega_0)$ for spherical nanoshell (outer radius/inner radius = 4/3) with dielectric core permittivity $\epsilon_c = 11.32$ | 26 |
| 1.13 | The comparison between calculated extinction cross section and Mie theory for a single silver sphere in vacuum environment. | 29 |
| 1.14 | The calculated extinction cross section spectrum for a single silver cube in water environment. | 29 |
| | | |
| 2.1 | Schematic illustration of Raman and Rayleigh scattering. | 34 |
| 2.2 | Calculated charge distribution for dipolar plasmon mode in AgNC monomer on silicon substrate. Red color and blue color represent the positive charges and negative charges, respectively. | 36 |
| 2.3 | Calculated $C(\omega_0)$ for dipolar plasmon mode in AgNC monomer on silicon substrate. Green (dashed) line represents the wavelength of incident laser and red (dot) line represents Raman-shifted wavelength. | 38 |
| 2.4 | Schematic illustration of three configurations of dimers. | 39 |
| 2.6 | Schematic illustration of vertical deposition. With the patterned substrate being slowly pulled out, the AgNC clusters fall into the pores due to capillary force. | 42 |
| 2.7 | (a) SEM image of the patterned substrate before the vertical deposition process; (b) and (c) show dimers of AgNCs (average edge length = 80 nm) that have been formed in the cavities of the patterned substrate. | 42 |
| 2.5 | Calculated charge distributions for (a) edge-to-edge dimers; (b) edge-to-face dimers; and (c) face-to-face dimers with 4 nm gap. Red color and blue color represent the positive charges and negative charges, respectively. | 48 |

| | | |
|------|---|----|
| 2.8 | Schematic of a general configuration for one dimer. | 49 |
| 2.9 | SERS substrate enhancement factors for EE dimers (blue), FE dimers (red), and FF dimers (green). Inset: Experimental cumulative fractions and fit to the Weibull distribution model (solid circles, experimental data; solid lines, fit values; the colors have the same meaning as above). | 49 |
| 3.1 | Schematic of ellipsoidal shell. | 54 |
| 3.2 | Plasmon resonance permittivity ε_2^- vs. shell thickness for various dielectric core permittivities $\tilde{\varepsilon}$ | 60 |
| 3.3 | Plasmon resonance permittivities of longitudinal dipolar plasmon mode and transverse dipolar plasmon mode vs. aspect ratio for silicon core $\tilde{\varepsilon} = 11.7\varepsilon_0$ and fixed thickness δ/b_1 | 60 |
| 3.4 | Schematic of ellipsoidal shell. | 61 |
| 3.5 | Light intensity of optical spots produced by the circularly polarized dipolar plasmon modes in (a) spherical, and (b) spheroidal nanoshells. | 65 |
| 3.6 | Radial variations of normalized light intensities generated by circularly polarized dipolar plasmon modes in spherical and spheroidal nanoshells. | 66 |
| 4.1 | Schematic illustration of recording head design in HAMR. | 70 |
| 4.2 | (a) The metallic nanoparticle of arbitrary shape with permittivity $\varepsilon(\omega)$ located near a dielectric object of arbitrary shape with permittivity $\tilde{\varepsilon}$; (b) The equivalent model with surface charges σ_1 and σ_2 distributed in free space. | 71 |
| 4.3 | (a) Metallic nanofilm with T-shaped aperture attached on glass substrate ($\tilde{\varepsilon} = 2.25\varepsilon_0$); (b) Lollipop metallic nanodisk placed next to Ta_2O_5 substrate ($\tilde{\varepsilon} = 4.6\varepsilon_0$) | 74 |
| 4.4 | (a) Plasmon mode for T-shaped aperture; (b) Surface charges distributed on glass substrate. | 76 |
| 4.5 | (a) Plasmon mode for lollipop metallic nanodisks; (b) Surface charges distributed on Ta_2O_5 substrate. | 78 |
| 4.6 | Light intensity enhancement generated by the plasmon mode in (a) T-shaped gold aperture and (b) lollipop gold nanodisk at the distance of 15 nm below. | 79 |
| 4.7 | (a) T-shaped perforated metallic nanofilms with plasmonic metal as heat sink; (b) Lollipop metallic nanodisks with plasmonic metal as heat sink. | 81 |
| 4.8 | Dispersion relations of real parts of dielectric permittivities for gold and copper given by [113]. | 82 |
| 4.9 | Surface charges distributed on heat sink layers for (a) T-aperture case and (b) lollipop disk case. | 84 |
| 4.10 | Light intensity enhancement calculated at (a) 15 nm below the bottom face of T-shaped gold aperture and (b) 15 nm below the peg of lollipop gold nanodisk in the presence of gold heat sink layers. | 86 |

| | | |
|------|---|-----|
| 5.1 | Determination of resonance wavelengths for radiation correction in formula (5.7) of a dipolar plasmon mode (Mode D1) in a single silver cube with various cube sizes. | 90 |
| 5.2 | Comparison between the calculation of the resonance permittivity of the dipole plasmon modes using second-order radiation corrections (open circles) and Mie theory (solid line) for spherical nanoparticles in water as a function of nanosphere dimension. | 91 |
| 5.3 | Comparison of the calculated dipole plasmon resonance wavelength of spherical nanoparticles in water computed by using second-order radiation corrections (open circles) and Mie theory (solid line). Data presented for (a) silver and (b) gold dispersion relations. | 92 |
| 5.4 | (a-c) SEM image of nanocubes. (a) An ensemble of silver nanocubes. Scale bar: 500 nm. (b) A small nanocube with rounded corners. (c) A large nanocube with sharp corners. (d) Absorption spectra of five types of silver nanocubes (in water). As the size of the nanocube increases, the absorbance peaks due to plasmon resonances shift to longer wavelengths. | 96 |
| 5.5 | Comparison between calculated (solid lines) and measured (open symbols) resonance wavelengths for five dipole plasmon modes of silver nanocubes. The solid symbols is experimental data for the major plasmon resonance wavelength from [101] and [102] | 100 |
| 5.6 | The fitting of experimental data by computational results for nanocubes with ideal sharp corners and for cubes with rounded corners. | 104 |
| 5.7 | Calculated resonance wavelengths of main dipole mode for face-to-face dimers with various cube sides and gaps. | 105 |
| A.1 | A molecule nearby a metallic nanoparticle | 111 |
| A.2 | Charge distribution for dipole mode. | 116 |
| A.3 | Computed $A_k(m, \omega_s)$ on xy -plane for dipole mode. | 116 |
| A.4 | Computed $A_k(m, \omega_s)$ on xz -plane for dipole mode. | 117 |
| A.5 | Computed $A_k(m, \omega_s)$ on yz -plane for dipole mode. | 117 |
| A.6 | Charge distribution for quadrupole mode. | 118 |
| A.7 | Computed $A_k(m, \omega_s)$ on xy -plane for quadrupole mode. | 118 |
| A.8 | Computed $A_k(m, \omega_s)$ on xz -plane for quadrupole mode. | 119 |
| A.9 | Computed $A_k(m, \omega_s)$ on yz -plane for quadrupole mode. | 119 |
| A.10 | Charge distribution for octupole mode. | 120 |
| A.11 | Computed $A_k(m, \omega_s)$ on xy -plane for octupole mode. | 120 |
| A.12 | Computed $A_k(m, \omega_s)$ on xz -plane for octupole mode. | 121 |
| A.13 | Computed $A_k(m, \omega_s)$ on yz -plane for octupole mode. | 121 |

Chapter 1

Plasmon Resonances in Nanoparticles

1.1 The Physical Origin of Plasmon Resonance

Plasmon resonances give a strongly localized and well defined color to specific metallic nanoparticles. This physical phenomenon has already been used for a long time throughout human history. Back in the Middle Ages, medieval artisans have used various metallic nanoparticles as colorants in stained glass windows, ceramics and enamel pottery. They accidentally became nanotechnologists without understanding the physical mechanisms behind the beautiful colors of these small metallic particles. If we have a bulk metal subject to optical radiation, we know the electric field inside the metal is attenuated, and the attenuation length (or skin depth) is controlled by the material property of the metal and the radiation frequency. In this situation, no special physical phenomena happen. However, if we cut this bulk metal into very small pieces down to nanoscale, extraordinary optical phenomenon start to appear such that they become very powerful localized light sources. A question can be asked: Why does this phenomenon only occur in the nanoscale metallic particles? Experiments show that metallic nanoparticles may exhibit resonance behavior at certain frequencies under the two conditions. First, the free-space wavelength is large in comparison with particle dimensions. This condition clearly suggests that these resonances are electrostatic in nature. Second, particle dielectric permittivity

has to be negative. If we consider a particle with positive dielectric permittivity, the depolarization field in the particle is opposite to the incident field. In this situation, the total electric field inside the particle is less than the incident field. However, if the particle has negative permittivity, the depolarization field in the particle is along the incident field, and consequently, the total field inside the particle is larger than the incident field (see Figure 1.1). In electrostatics, this condition implies that the source-free electrostatic field may exist since the uniqueness theorem in electrostatic is no longer valid.

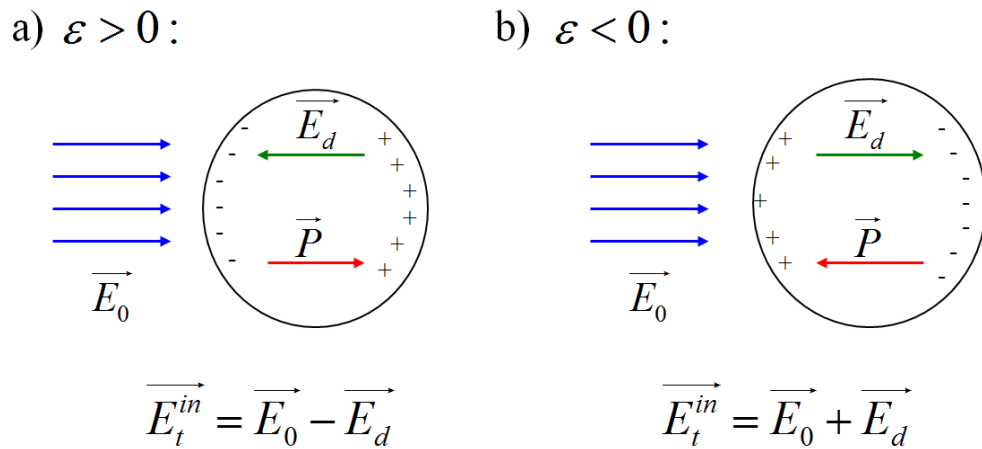


Figure 1.1: Schematic illustration of total field inside a particle with (a) positive permittivity; (b) negative permittivity.

For these two reasons, source-free electrostatic fields may appear for certain negative values of dielectric permittivity, and this source-free electrostatic fields are resonant plasmon modes. As one can see, the above two resonance conditions can be simultaneously and naturally realized in metallic particles at the nanoscale. Therefore, plasmon resonances in metallic nanoparticles are intrinsically nanoscale phenomena. These resonances result in powerful localized sources of light that are useful

in scanning near-field optical microscopy ([2][3]), nanolithography [4], and in biosensor applications ([5][6]). It is also believed that strong local electromagnetic fields associated with these resonances may play an important role in surface-enhanced Raman scattering (SERS) ([7][10]). Furthermore, it is anticipated that these resonances may be instrumental in the emerging field of nanophotonics where resonant nanoparticles will be used to guide and switch light at the nanoscale ([11]-[14]). In this way, these resonances may pave the way to all-optical computing where information transmission and processing occur entirely at the optical level. Finally, the utilization of resonant nanoparticles may also dramatically reduce the physical bit size for the next generation of optical data storage disks ([15][16]).

1.2 Analytical Solutions of Plasmon Resonances in Nanoparticles

Resonances in metallic nanoparticles are often found experimentally by measuring the extinction cross section spectrum or numerically by using the finite-difference-time-domain (FDTD) technique. However, plasmon resonances can be analytically studied for the metallic nanoparticle with simple geometries. The analytical results are based on the method of separation of variables in different coordinate systems. In this method, possible solutions of the Laplace equation are expressed as products of functions, and these product solutions are plasmon modes. The specific resonance values of permittivity can be found from the interface boundary conditions.

It is apparent that these analytical solutions can be used as test examples for nu-

merical computations. Most of these analytical solutions for various nanoparticles are covered in Prof. Mayergoyz’s book [1]. Here, we present two examples of these analytical solutions which are both based on bipolar coordinates. Bipolar coordinates are a two-dimensional orthogonal coordinate system consisting of the circles whose centers are located on two orthogonal poles. They are commonly described by the following equations:

$$(x - a \coth \eta)^2 + y^2 = \frac{a^2}{\sinh^2 \eta} \quad (1.1)$$

$$x^2 + (y - a \cot \xi)^2 = \frac{a^2}{\sin^2 \xi}, \quad (1.2)$$

where $-\infty < \eta < \infty$ and $0 \leq \xi \leq 2\pi$. $\eta = \text{const.}$ represents a circle centered at $x = a \coth \eta$, and $\xi = \text{const.}$ represents a circle centered at $y = a \cot \xi$. Physically, the centers of the circles, which are separated by one pole, can be treated as where the two point charges with opposite signs are located. Then, different ξ values give us the electric field lines between these two points, and the η provides the equipotential lines. In addition, bipolar coordinates are the basis of the formation of other, three-dimensional, orthogonal coordinates. By rotating the bipolar coordinates about the x -axis, one can obtain the so-called “bispherical coordinates”. By rotating the bipolar coordinates about the y -axis, one can obtain the “toroidal coordinates”. Finally, there are so-called “bipolar cylindrical coordinates” which are formed by projecting the bipolar coordinates on a $z = \text{const.}$ plane. We first start with the case of two adjacent spherical nanoparticles.

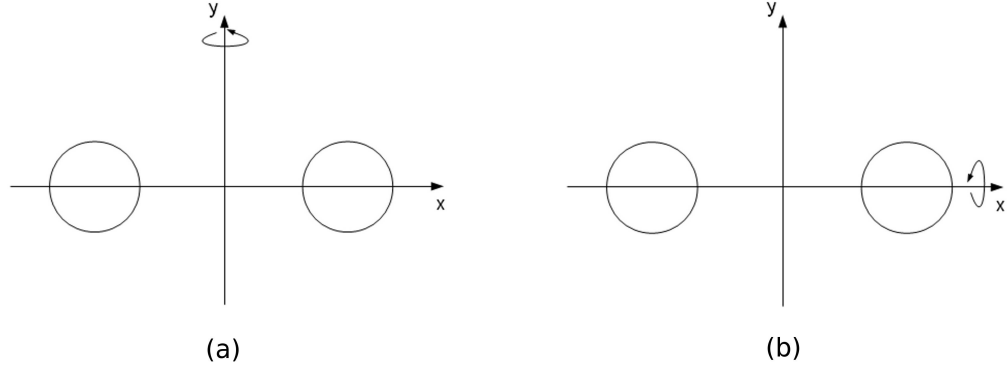


Figure 1.2: (a) Toroid after rotating along y-axis; (b) Bispheres after rotating along x-axis.

1.2.1 Example I: Two Adjacent Spherical Nanoparticles

Plasmon modes in two adjacent spherical nanoparticles can be analyzed by employing bispherical coordinates ([17][18]). The bispherical coordinates (μ, η, ϕ) are related to Cartesian coordinates by the formulas

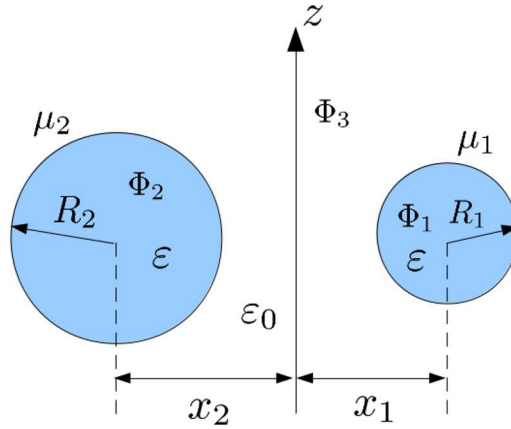


Figure 1.3: Schematic illustration of two spheres.

$$x = \frac{a \sin \eta \cos \phi}{\cosh \mu - \cos \eta}, \quad y = \frac{a \sin \eta \sin \phi}{\cosh \mu - \cos \eta}, \quad z = \frac{a \sinh \mu}{\cosh \mu - \cos \eta}. \quad (1.3)$$

Figure 1.3 shows the schematic illustration of two adjacent spheres. By properly choosing bispherical coordinates, the boundaries of two spheres coincide with the

coordinate surfaces $\mu = \mu_1$ and $\mu = \mu_2$, where $\mu_1 > 0$ and $\mu_2 < 0$. The radii and centers of the two spheres can be determined by the formulas

$$R_1 = \frac{a}{\sinh \mu_1}, \quad x_1 = a \coth \mu_1; \quad R_2 = \frac{a}{|\sinh \mu_2|}, \quad x_2 = a \coth \mu_2. \quad (1.4)$$

To analyze plasmon modes in this problem, we make use of the scalar potential Φ of the displacement field \mathbf{D} ,

$$\mathbf{D} = -\nabla \Phi. \quad (1.5)$$

The plasmon modes in two adjacent spherical nanoparticles are the nanozero solutions to the following homogeneous boundary value problem:

$$\nabla^2 \Phi_k = 0, \quad (k = 1, 2, 3) \quad (1.6)$$

$$\frac{\Phi_1}{\varepsilon} \Big|_{\mu_1} = \frac{\Phi_3}{\varepsilon_0} \Big|_{\mu_1}, \quad \frac{\Phi_2}{\varepsilon} \Big|_{\mu_2} = \frac{\Phi_3}{\varepsilon_0} \Big|_{\mu_2} \quad (1.7)$$

$$\frac{1}{h_\mu} \frac{\partial \Phi_1}{\partial \mu} \Big|_{\mu_1} = \frac{1}{h_\mu} \frac{\partial \Phi_3}{\partial \mu} \Big|_{\mu_1} \quad (1.8)$$

$$\frac{1}{h_\mu} \frac{\partial \Phi_2}{\partial \mu} \Big|_{\mu_2} = \frac{1}{h_\mu} \frac{\partial \Phi_3}{\partial \mu} \Big|_{\mu_2}, \quad (1.9)$$

where h_μ is one of the metric coefficients in the bispherical coordinate system. By using the method of separation of variables in bispherical coordinates, the solutions of the Laplace equations for each region can be expressed in the following:

$$\Phi_1 = \sqrt{\cosh \mu - \cos \eta} \sum_{n=0}^{\infty} \sum_{m=-n}^n A_{mn} e^{-(n+\frac{1}{2})\mu} P_n^m(\cos \eta) e^{jm\varphi} \quad (1.10)$$

$$\Phi_2 = \sqrt{\cosh \mu - \cos \eta} \sum_{n=0}^{\infty} \sum_{m=-n}^n B_{mn} e^{(n+\frac{1}{2})\mu} P_n^m(\cos \eta) e^{jm\varphi} \quad (1.11)$$

$$\Phi_3 = \sqrt{\cosh \mu - \cos \eta} \sum_{n=0}^{\infty} \sum_{m=-n}^n \left[C_{mn} e^{-(n+\frac{1}{2})\mu} + D_{mn} e^{(n+\frac{1}{2})\mu} \right] P_n^m(\cos \eta) e^{jm\varphi}. \quad (1.12)$$

P_n^m is known as the associated Legendre function of degree n and order m , where n is a positive integer and $m = 0, \dots, n$. Apparently the one-dimensional case, where Φ_k ($k = 1, 2, 3$) is a function of η only or φ only, cannot occur in bispherical coordinates. The square-root factor makes a one-dimensional solution impossible. Nevertheless, some results can still be obtained. From boundary conditions (1.7), we have

$$A_{mn} = \frac{\varepsilon}{\varepsilon_0} [C_{mn} + D_{mn}e^{(2n+1)\mu_1}] \quad (1.13)$$

$$B_{mn} = \frac{\varepsilon}{\varepsilon_0} [C_{mn}e^{-(2n+1)\mu_2} + D_{mn}]. \quad (1.14)$$

From boundary conditions (1.8), we have

$$\begin{aligned} & \frac{\sinh \mu_1}{2} \sum_{n=0}^{\infty} \sum_{m=-n}^n A_{mn} e^{-(n+\frac{1}{2})\mu} P_n^m(\cos \eta) e^{jm\varphi} \\ & - \cosh \mu_1 \sum_{n=0}^{\infty} \sum_{m=-n}^n (n + \frac{1}{2}) A_{mn} e^{-(n+\frac{1}{2})\mu} P_n^m(\cos \eta) e^{jm\varphi} \\ & + \sum_{n=0}^{\infty} \sum_{m=-n}^n (n + \frac{1}{2}) A_{mn} e^{-(n+\frac{1}{2})\mu} \cos \eta P_n^m(\cos \eta) e^{jm\varphi} = \\ & \frac{\sinh \mu_1}{2} \sum_{n=0}^{\infty} \sum_{m=-n}^n [C_{mn} e^{-(n+\frac{1}{2})\mu} + D_{mn} e^{(n+\frac{1}{2})\mu}] e^{-(n+\frac{1}{2})\mu} P_n^m(\cos \eta) e^{jm\varphi} \\ & - \cosh \mu_1 \sum_{n=0}^{\infty} \sum_{m=-n}^n (n + \frac{1}{2}) [C_{mn} e^{-(n+\frac{1}{2})\mu} - D_{mn} e^{(n+\frac{1}{2})\mu}] e^{-(n+\frac{1}{2})\mu} P_n^m(\cos \eta) e^{jm\varphi} \\ & + \sum_{n=0}^{\infty} \sum_{m=-n}^n (n + \frac{1}{2}) [C_{mn} e^{-(n+\frac{1}{2})\mu} - D_{mn} e^{(n+\frac{1}{2})\mu}] e^{-(n+\frac{1}{2})\mu} \cos \eta P_n^m(\cos \eta) e^{jm\varphi}. \end{aligned} \quad (1.15)$$

By using the recurrence relation and the definition of spherical harmonics, the left-hand side of (1.15) can be rewritten as

$$\begin{aligned}
& \sum_{n=0}^{\infty} \sum_{m=-n}^n A_{mn} e^{-(n+\frac{1}{2})\mu_1} [\sinh \mu_1 - (2n+1) \cosh \mu_1] \frac{1}{\sqrt{\frac{2n+1}{4\pi} \frac{(n-m)!}{(n+m)!}}} Y_{mn} + \\
& \sum_{n=0}^{\infty} \sum_{m=-n}^n A_{mn} e^{-(n+\frac{1}{2})\mu_1} (n+1-m) \frac{1}{\sqrt{\frac{2(n+1)+1}{4\pi} \frac{((n+1)-m)!}{((n+1)+m)!}}} Y_{mn+1} + \\
& \sum_{n=0}^{\infty} \sum_{m=-n}^n A_{mn} e^{-(n+\frac{1}{2})\mu_1} (n+m) \frac{1}{\sqrt{\frac{2(n-1)+1}{4\pi} \frac{((n-1)-m)!}{((n-1)+m)!}}} Y_{mn-1},
\end{aligned} \tag{1.16}$$

where Y_{mn} are known as spherical harmonics. Similar manipulation can be applied to the right-hand side of (1.15). Next, in order to identify the coefficients of Y_{mn} , we exploit the orthogonality of spherical harmonics by multiplying Y_{mn} on both sides of (1.15) and integrating over η and φ . In this way, we obtain

$$\begin{aligned}
& (n-m)A_{mn-1}e^{-(n-\frac{1}{2})\mu_1} + [\sinh \mu_1 - (2n+1) \cosh \mu_1]A_{mn}e^{-(n+\frac{1}{2})\mu_1} \\
& + (n+1+m)A_{mn+1}e^{-(n+\frac{3}{2})\mu_1} \\
& = (n-m)C_{mn-1}e^{-(n-\frac{1}{2})\mu_1} + [\sinh \mu_1 - (2n+1) \cosh \mu_1]C_{mn}e^{-(n+\frac{1}{2})\mu_1} \\
& + (n+1+m)C_{mn+1}e^{-(n+\frac{3}{2})\mu_1} - (n-m)D_{mn-1}e^{(n-\frac{1}{2})\mu_1} \\
& + [\sinh \mu_1 + (2n+1) \cosh \mu_1]D_{mn}e^{(n+\frac{1}{2})\mu_1} - (n+1+m)D_{mn+1}e^{(n+\frac{3}{2})\mu_1}.
\end{aligned} \tag{1.17}$$

Now we define the following coefficients:

$$\begin{aligned}
a_{mn} &= A_{mn}e^{-(n+\frac{1}{2})\mu_1} \quad , \quad b_{mn} = B_{mn}e^{(n+\frac{1}{2})\mu_2} \quad , \quad c_{mn}^1 = C_{mn}e^{-(n+\frac{1}{2})\mu_1} \\
c_{mn}^2 &= C_{mn}e^{-(n+\frac{1}{2})\mu_2} \quad , \quad d_{mn}^1 = D_{mn}e^{(n+\frac{1}{2})\mu_1} \quad , \quad d_{mn}^2 = D_{mn}e^{(n+\frac{1}{2})\mu_2}.
\end{aligned} \tag{1.18}$$

In such a way, (1.17) becomes

$$\begin{aligned}
& (n-m)a_{mn-1} + [\sinh \mu_1 - (2n+1) \cosh \mu_1]a_{mn} + (n+1+m)a_{mn+1} \\
& = (n-m)c_{mn-1}^1 + [\sinh \mu_1 - (2n+1) \cosh \mu_1]c_{mn}^1 + (n+1+m)c_{mn+1}^1 \\
& - (n-m)d_{mn-1}^1 + [\sinh \mu_1 + (2n+1) \cosh \mu_1]d_{mn}^1 - (n+1+m)d_{mn+1}^1.
\end{aligned} \tag{1.19}$$

Similar to (1.19), (1.17) is expressed as

$$\begin{aligned}
& (n-m)c_{mn-1}^2 + [\sinh \mu_2 - (2n+1) \cosh \mu_2]c_{mn}^2 + (n+1+m)c_{mn+1}^2 \\
& - (n-m)d_{mn-1}^2 + [\sinh \mu_2 + (2n+1) \cosh \mu_2]d_{mn}^2 - (n+1+m)d_{mn+1}^2 \quad (1.20) \\
& = -(n-m)b_{mn-1} + [\sinh \mu_2 + (2n+1) \cosh \mu_2]b_{mn} - (n+1+m)b_{mn+1}.
\end{aligned}$$

By defining the coefficients in (1.18), (1.13) and (1.14) can also be reduced to

$$a_{mn} = \frac{\varepsilon}{\varepsilon_0}(c_{mn}^1 + d_{mn}^1) \quad (1.21)$$

$$b_{mn} = \frac{\varepsilon}{\varepsilon_0}(c_{mn}^2 + d_{mn}^2). \quad (1.22)$$

The relations between c_{mn}^1 and c_{mn}^2 as well as d_{mn}^1 and d_{mn}^2 are

$$c_{mn}^2 = c_{mn}^1 e^{(n+\frac{1}{2})(\mu_1-\mu_2)} \quad (1.23)$$

$$d_{mn}^2 = d_{mn}^1 e^{-(n+\frac{1}{2})(\mu_1-\mu_2)}. \quad (1.24)$$

For different n , (1.19)-(1.24) constitute a set of homogeneous equations for a_{mn} , b_{mn} , c_{mn}^1 , and d_{mn}^1 . Therefore, we define the following vectors:

$$\begin{aligned}
\vec{a}_m &= [a_{m0}, a_{m1}, a_{m2}, \dots, a_{mn}] \quad , \quad \vec{b}_m = [b_{m0}, b_{m1}, b_{m2}, \dots, b_{mn}] \\
\vec{c}_m^1 &= [c_{m0}^1, c_{m1}^1, c_{m2}^1, \dots, c_{mn}^1] \quad , \quad \vec{c}_m^2 = [c_{m0}^2, c_{m1}^2, c_{m2}^2, \dots, c_{mn}^2] \\
\vec{d}_m^1 &= [d_{m0}^1, d_{m1}^1, d_{m2}^1, \dots, d_{mn}^1] \quad , \quad \vec{d}_m^2 = [d_{m0}^2, d_{m1}^2, d_{m2}^2, \dots, d_{mn}^2]. \quad (1.25)
\end{aligned}$$

Then (1.19)-(1.24) for all n can be expressed in the following:

$$T(\mu_1)\vec{a}_m = T(\mu_1)\vec{c}_m^1 - T(-\mu_1)\vec{d}_m^1 \quad (1.26)$$

$$\vec{a}_m = \frac{\varepsilon}{\varepsilon_0}(\vec{c}_m^1 + \vec{d}_m^1) \quad (1.27)$$

$$-T(-\mu_2)\vec{b}_m = T(\mu_2)\vec{c}_m^2 - T(-\mu_2)\vec{d}_m^2 \quad (1.28)$$

$$\vec{b}_m = \frac{\varepsilon}{\varepsilon_0}(\vec{c}_m^2 + \vec{d}_m^2), \quad (1.29)$$

$$\text{where } \vec{c}_m^2 = I\vec{c}_m^1, \quad \vec{d}_m^2 = I^{-1}\vec{d}_m^1, \quad (1.30)$$

where

$$T(\mu) = \begin{bmatrix} \sinh \mu - \cosh \mu & 1 + m & & & \\ 1 - m & \sinh \mu - 3 \cosh \mu & 2 + m & & \\ & 2 - m & \ddots & & n + m \\ & & n - m & \sinh \mu - (2n + 1) \cosh \mu & \\ & & & & \end{bmatrix} \quad (1.31)$$

$$I = \begin{bmatrix} e^{\frac{1}{2}(\mu_1 - \mu_2)} & & & & \\ & e^{\frac{3}{2}(\mu_1 - \mu_2)} & & & \\ & & \ddots & & \\ & & & \ddots & \\ & & & & e^{(n + \frac{1}{2})(\mu_1 - \mu_2)} \end{bmatrix}. \quad (1.32)$$

It can be seen that I is a diagonal matrix, while $T(\mu)$ is a tridiagonal matrix. In the following derivation, we have to deal with $T(-\mu)^{-1}$, the inverse of a tridiagonal matrix. By using the method proposed and published by R. A. Usmani in 1993 [19], one can easily obtain the inverse of a tridiagonal matrix. Considering (1.30), we

rewrite (1.28), (1.29), and (1.26) as follows:

$$\begin{aligned}\vec{b}_m &= \vec{d}_m^2 - T(-\mu_2)^{-1}T(\mu_2)\vec{c}_m^2 \\ &= I^{-1}\vec{d}_m^1 - T(-\mu_2)^{-1}T(\mu_2)I\vec{c}_m^1\end{aligned}\quad (1.33)$$

$$\vec{b}_m = \frac{\varepsilon}{\varepsilon_0}(I\vec{c}_m^1 + I^{-1}\vec{d}_m^1)\quad (1.34)$$

$$\vec{a}_m = \vec{c}_m^1 - T(\mu_1)^{-1}T(-\mu_1)\vec{d}_m^1.\quad (1.35)$$

After some straightforward transformations and substitutions of the above equations, we obtain the following two coupled equations:

$$\frac{\varepsilon}{\varepsilon_0}\vec{c}_m^1 = (I - I^{-1})^{-1} \left[-T(-\mu_2)^{-1}T(\mu_2)I + I^{-1} \right] \vec{c}_m^1 + (I^{-1} + I^{-1}T(\mu_1)^{-1}T(-\mu_1))\vec{d}_m^1\quad (1.36)$$

$$\frac{\varepsilon}{\varepsilon_0}\vec{d}_m^1 = (I - I^{-1})^{-1} \left[(I + T(-\mu_2)^{-1}T(\mu_2)I)\vec{c}_m^1 - (IT(\mu_1)^{-1}T(-\mu_1) + I^{-1})\vec{d}_m^1 \right].\quad (1.37)$$

By defining vector X as follows,

$$X = \begin{bmatrix} \vec{c}_m^1 \\ \vec{d}_m^1 \end{bmatrix},\quad (1.38)$$

(1.36) and (1.37) can be incorporated into the following matrix representation:

$$\frac{\varepsilon}{\varepsilon_0}X = \begin{bmatrix} T_1 & T_2 \\ T_3 & T_4 \end{bmatrix} X,\quad (1.39)$$

where

$$T_1 = -(I - I^{-1})^{-1}(T(-\mu_2)^{-1}T(\mu_2)I + I^{-1}) \quad (1.40)$$

$$T_2 = (I - I^{-1})^{-1}(I^{-1} + I^{-1}T(\mu_1)^{-1}T(-\mu_1)) \quad (1.41)$$

$$T_3 = (I - I^{-1})^{-1}(I + T(-\mu_2)^{-1}T(\mu_2)I) \quad (1.42)$$

$$T_4 = -(I - I^{-1})^{-1}(IT(\mu_1)^{-1}T(-\mu_1) + I^{-1}). \quad (1.43)$$

Now that the whole problem is reduced to solving the eigenvalue problem in (1.39), we can find the eigenvalues $\varepsilon_k/\varepsilon_0$ and eigenvectors X , and hence determine the resonance frequencies and corresponding electric fields generated by the plasmon modes.

1.2.2 Example II: Toroidal Nano-rings

As in the case of two adjacent spheres, plasmon modes in toroidal nano-rings can be studied in toroidal coordinates ([17][18]). The toroidal coordinates can be converted to Cartesian coordinates by the following relations:

$$x = \frac{a \sinh \mu \cos \varphi}{\cosh \mu - \cos \eta}, \quad y = \frac{a \sinh \mu \sin \varphi}{\cosh \mu - \cos \eta}, \quad z = \frac{a \sin \eta}{\cosh \mu - \cos \eta}. \quad (1.44)$$

Figure 1.4 shows the schematic illustration of a toroidal nano-ring. The radius of its circular cross section and the distance to the center of its cross section are defined as

$$R = \frac{a}{\sinh \mu_0}, \quad x_0 = a \coth \mu_0. \quad (1.45)$$

As in the bispherical case, we utilize the scalar potential φ of the displacement field to analyze the plasmon modes in toroidal nano-rings. The problem is reduced to

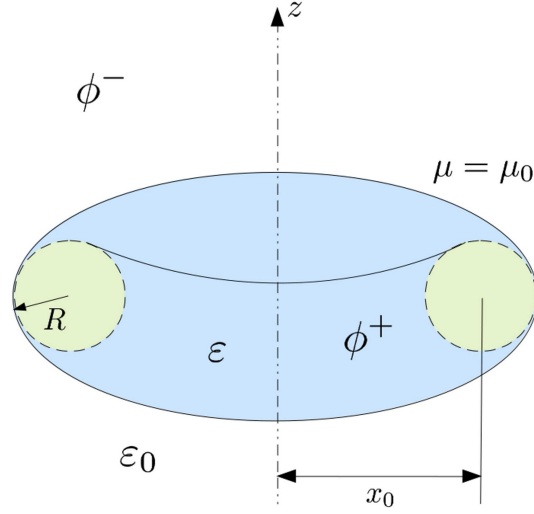


Figure 1.4: Schematic of a toroidal nano-ring.

finding the nonzero solutions to the following homogeneous boundary value problem:

$$\nabla^2 \phi^\pm = 0 \quad (1.46)$$

$$\left. \frac{\phi^+}{\epsilon} \right|_{\mu_0} = \left. \frac{\phi^-}{\epsilon_0} \right|_{\mu_0} \quad (1.47)$$

$$\left. \frac{1}{h_\mu} \frac{\partial \phi^+}{\partial \mu} \right|_{\mu_0} = \left. \frac{1}{h_\mu} \frac{\partial \phi^-}{\partial \mu} \right|_{\mu_0}. \quad (1.48)$$

By using the method of separation of variables, we find the particular solutions of the Laplace equation in toroidal coordinates which satisfy the regularity inside and outside the nano-ring:

$$\phi^+ = \sqrt{\cosh \mu - \cos \eta} \sum_{n=0}^{\infty} \sum_{m=0}^{\infty} A_{mn} \cos m\varphi \cos n\eta Q_{n-\frac{1}{2}}^m(\cosh \mu) \quad (1.49)$$

$$\phi^- = \sqrt{\cosh \mu - \cos \eta} \sum_{n=0}^{\infty} \sum_{m=0}^{\infty} B_{mn} \cos m\varphi \cos n\eta P_{n-\frac{1}{2}}^m(\cosh \mu). \quad (1.50)$$

$P_{n-\frac{1}{2}}^m$ is the half-integer associated Legendre function, and $Q_{n-\frac{1}{2}}^m$ is known as half-integer associated Legendre function of the second kind, where $n = 0, 1, \dots$ and $m = 0, 1, \dots$. As in the bispherical case, there is no way to get one-dimensional

solutions in toroidal coordinates. However, as in the bispherical case, some results still can be obtained. From boundary conditions (1.47) and (1.48) we obtain

$$\varepsilon_0 A_{mn} Q_{n-\frac{1}{2}}^m(\cosh \mu_0) = \varepsilon B_{mn} P_{n-\frac{1}{2}}^m(\cosh \mu_0) \quad (1.51)$$

$$\begin{aligned} & \frac{\sinh \mu_0}{2\sqrt{\cosh \mu_0 - \cos \eta}} \sum_{n=0}^{\infty} \sum_{m=0}^{\infty} A_{mn} \cos m\varphi \cos n\eta Q_{n-\frac{1}{2}}^m(\cosh \mu_0) \\ & + \sqrt{\cosh \mu_0 - \cos \eta} \sum_{n=0}^{\infty} \sum_{m=0}^{\infty} A_{mn} \cos m\varphi \cos n\eta \left. \frac{dQ_{n-\frac{1}{2}}^m}{d\mu} \right|_{\mu_0} \\ & = \frac{\sinh \mu_0}{2\sqrt{\cosh \mu_0 - \cos \eta}} \sum_{n=0}^{\infty} \sum_{m=0}^{\infty} B_{mn} \cos m\varphi \cos n\eta P_{n-\frac{1}{2}}^m(\cosh \mu_0) \\ & + \sqrt{\cosh \mu_0 - \cos \eta} \sum_{n=0}^{\infty} \sum_{m=0}^{\infty} B_{mn} \cos m\varphi \cos n\eta \left. \frac{dP_{n-\frac{1}{2}}^m}{d\mu} \right|_{\mu_0}. \end{aligned} \quad (1.52)$$

By multiplying (1.52) by $\sqrt{\cosh \mu_0 - \cos \eta}$ and using the trigonometric product-to-sum identity, the left-hand side of (1.52) can be rewritten as

$$\begin{aligned} & \frac{\sinh \mu_0}{2} \sum_{n=0}^{\infty} \sum_{m=0}^{\infty} A_{mn} \cos m\varphi \cos n\eta Q_{n-\frac{1}{2}}^m(\cosh \mu_0) \\ & + \cosh \mu_0 \sum_{n=0}^{\infty} \sum_{m=0}^{\infty} A_{mn} \cos m\varphi \cos n\eta \left. \frac{dQ_{n-\frac{1}{2}}^m}{d\mu} \right|_{\mu_0} \\ & - \frac{1}{2} \sum_{n=0}^{\infty} \sum_{m=0}^{\infty} A_{mn} \cos m\varphi [\cos(n-1)\eta + \cos(n+1)\eta] \left. \frac{dQ_{n-\frac{1}{2}}^m}{d\mu} \right|_{\mu_0}. \end{aligned} \quad (1.53)$$

The same manipulation can be applied to the right-hand side of (1.52). We identify the coefficient of $\cos n\eta$ by multiplying $\cos n\eta$ on both sides of (1.52) and integrating over η . Note that now we have to deal with the values of $P_{n-\frac{1}{2}}^m(\cosh \mu_0)$ and $Q_{n-\frac{1}{2}}^m(\cosh \mu_0)$ and their derivatives. The general behaviors of P and Q functions are shown in [17], while tabulated values can be obtained from *Tables of Associated Legendre functions* (Columbia Univ. Press, New York, 1945). Computationally, A. Gil and J. Segura have developed some programs to evaluate Legendre functions and

toroidal harmonics with remarkable accuracy ([20]-[22]). By defining the following coefficients

$$a_{mn} = Q_{n-\frac{1}{2}}^m(\cosh \mu_0) \quad , \quad c_{mn} = P_{n-\frac{1}{2}}^m(\cosh \mu_0) \quad (1.54)$$

$$b_{mn} = \left. \frac{dQ_{n-\frac{1}{2}}^m}{d\mu} \right|_{\mu_0} \quad , \quad d_{mn} = \left. \frac{dP_{n-\frac{1}{2}}^m}{d\mu} \right|_{\mu_0} \quad , \quad (1.55)$$

we obtain

$$\begin{aligned} & \left(\frac{\sinh \mu_0}{2} a_{mn} + \cosh \mu_0 b_{mn} \right) A_{mn} - \frac{1}{2} (b_{mn-1} A_{mn-1} + b_{mn+1} A_{mn+1}) \\ & = \left(\frac{\sinh \mu_0}{2} c_{mn} + \cosh \mu_0 d_{mn} \right) B_{mn} - \frac{1}{2} (d_{mn-1} B_{mn-1} + d_{mn+1} B_{mn+1}) \end{aligned} \quad (1.56)$$

and

$$\varepsilon B_{mn} = \varepsilon_0 \frac{a_{mn}}{c_{mn}} A_{mn}. \quad (1.57)$$

Then we define the following vectors:

$$\vec{A}_m = [A_{m0}, A_{m1}, A_{m2}, \dots, A_{mn}] \quad (1.58)$$

$$\vec{B}_m = [B_{m0}, B_{m1}, B_{m2}, \dots, B_{mn}]. \quad (1.59)$$

Therefore, for a fixed m , (1.56) and (1.57) for all different n can be expressed in the following matrix representation:

$$\varepsilon \vec{B}_m = \varepsilon_0 D \vec{A}_m \quad (1.60)$$

$$T_B \vec{B}_m = T_A \vec{A}_m, \quad (1.61)$$

where

$$T_A = \begin{bmatrix} \frac{\sinh \mu_0}{2} a_{m0} + \cosh \mu_0 b_{m0} & -\frac{1}{2} b_{m1} & & \\ & -\frac{1}{2} b_{m0} & \ddots & \\ & & & -\frac{1}{2} b_{mn} \\ & & -\frac{1}{2} b_{mn-1} & \frac{\sinh \mu_0}{2} a_{mn} + \cosh \mu_0 b_{mn} \end{bmatrix} \quad (1.62)$$

$$T_B = \begin{bmatrix} \frac{\sinh \mu_0}{2} c_{m0} + \cosh \mu_0 d_{m0} & -\frac{1}{2} d_{m1} & & \\ & -\frac{1}{2} d_{m0} & \ddots & -\frac{1}{2} d_{mn} \\ & & & -\frac{1}{2} d_{mn-1} & \frac{\sinh \mu_0}{2} c_{mn} + \cosh \mu_0 d_{mn} \end{bmatrix} \quad (1.63)$$

$$D = \begin{bmatrix} \frac{a_{m0}}{c_{m0}} & & & \\ & \ddots & & \\ & & & \frac{a_{m0}}{c_{mn}} \end{bmatrix}. \quad (1.64)$$

We multiply T_A^{-1} , which can be obtained by using Usmani's method, on both sides of (1.61), and substitute it into (1.60):

$$\boxed{\varepsilon \vec{B}_m = \varepsilon_0 D T_A^{-1} T_B \vec{B}_m = L \vec{B}_m}, \quad (1.65)$$

where

$$L = \varepsilon_0 D T_A^{-1} T_B. \quad (1.66)$$

By solving the eigenvalue problem (1.65), eigenvalues ε_k^m and eigenvectors \vec{B}_m can be found, and hence the resonance frequencies and plasmon fields can be determined.

1.3 Mode Analysis of the Plasmon Resonances in Nanoparticles

The preceding section describes the method for solving the plasmon modes in nanoparticles with simple geometries. However, there are many metallic nanoparticles of interest whose plasmon resonances cannot be analytically obtained, e.g., nanocubes and nanorods. To find the plasmon modes in such nanoparticles, some numerical techniques are employed. As mentioned in the previous section, the numerical analysis is typically performed by using the FDTD technique. Another way

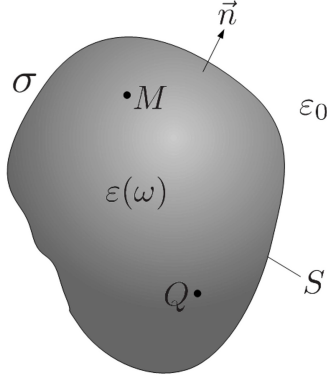


Figure 1.5: The metallic nanoparticle bounded by surface S .

to solve this problem is to use the so-called eigenmode technique [23]. This technique allows us to directly calculate the resonance values of dielectric permittivity and hence the corresponding resonance frequencies by using the appropriate dispersion relation of a metallic nanoparticle. Consider a dielectric object of arbitrary shape with permittivity $\varepsilon(\omega)$ (see Figure 1.5). We are interested in negative values of $\varepsilon(\omega)$ for which a source-free electromagnetic field may exist. It turns out that the electric potential inside and outside the particle can be represented as being generated by a single layer of electric charges σ distributed over the particle boundary S . This single layer of electric charges on S creates the same electric field in free space as the source-free electric field that may exist in the presence of the dielectric particle with negative permittivity. By applying boundary conditions, the following homogeneous boundary integral equation can be derived:

$$\sigma_k(Q) = \frac{\lambda_k}{2\pi} \oint_S \sigma_k(M) \frac{\mathbf{r}_{MQ} \cdot \mathbf{n}_Q}{r_{MQ}^3} dS_M, \quad (1.67)$$

where

$$\lambda_k = \frac{\varepsilon_k - \varepsilon_0}{\varepsilon_k + \varepsilon_0}, \quad (1.68)$$

and $\sigma_k(M)$ represents the surface charges on S that produce the electric field of the k th plasmon mode. All other notations in formula (1.67) have their usual meaning. After λ_k are computed, the resonance frequencies ω_k can be determined by using formula (1.68) and the permittivity dispersion relation:

$$\varepsilon_k = \varepsilon'(\omega_k) = \text{Re}[\varepsilon(\omega_k)]. \quad (1.69)$$

Figures 1.6 and 1.7 present the dispersion relations of gold and silver, respectively, based on the experimental measurements by Johnson and Christy [88].

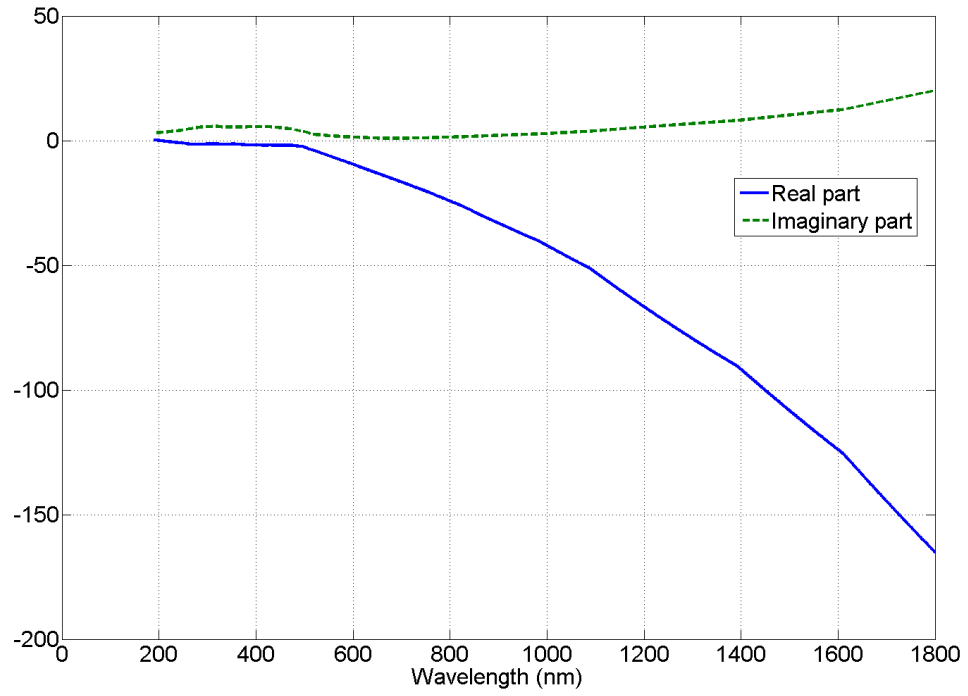


Figure 1.6: Dispersion relation of gold measured by Johnson and Christy.

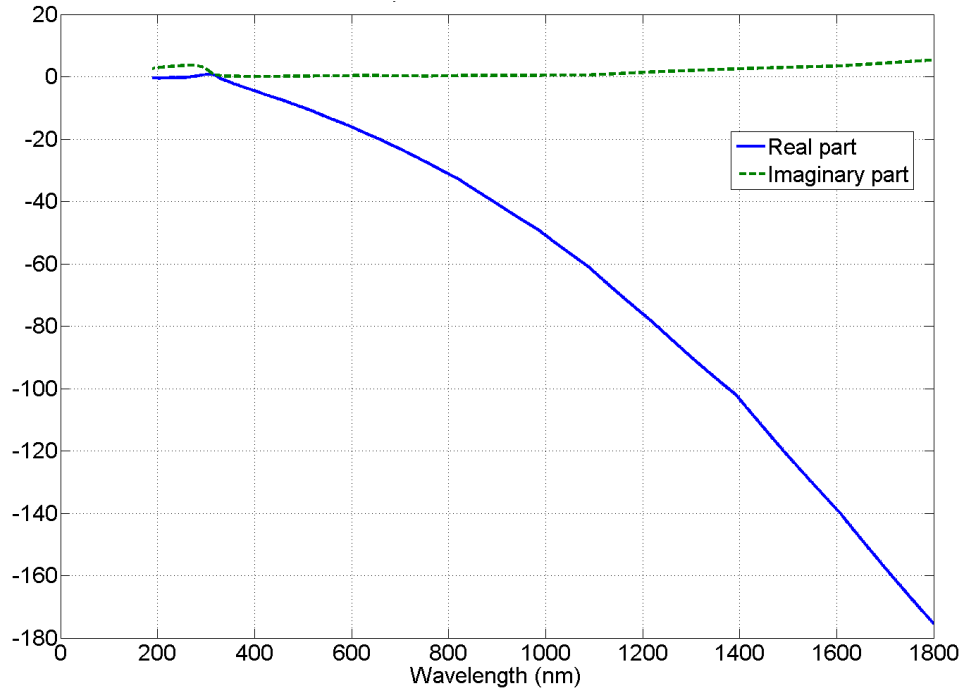


Figure 1.7: Dispersion relation of silver measured by Johnson and Christy.

To this end, one can see that we formulate the plasmon modes in a dielec-

tric nanoparticle as an eigenvalue problem. λ_k is the eigenvalue which reveals the resonance frequency of the k th plasmon mode, while $\sigma_k(M)$ is the eigenfunction which visualizes the corresponding plasmon mode. If the particle boundary S is not smooth, then $\sigma_k(M)$ may have singularities at the corners and the edges of S that may negatively affect the accuracy of numerical computations. In this situation, the dual formulation is employed in which the electric displacement field \mathbf{D}_0 is introduced instead of electric field \mathbf{E}_0 . By the same reasoning as in the derivation of (1.67), we obtain another homogeneous boundary integral equation as follows:

$$\tau_k(Q) = \frac{\lambda_k}{2\pi} \oint_S \tau_k(M) \frac{\mathbf{r}_{QM} \cdot \mathbf{n}_M}{r_{QM}^3} dS_M, \quad (1.70)$$

where $\tau_k(Q)$ has the physical meaning of double layer of electric charges (dipoles) distributed over the boundary S of the particle. It can be seen that the boundary integral equation is adjoint to the integral equation (1.67). For this reason, it has the same spectrum (as expected on the physical grounds). The dipole density $\tau(M)$ is proportional to the discontinuity of double-layer potential across S and, consequently, it is finite even for non-smooth boundaries S . This is the advantage of integral equation (1.70) for numerical computations with non-smooth boundaries S .

The presented discussion can be easily extended to the analysis of electrostatic (plasmon) resonances of several particles located in proximity to one another. In this case, S in integral equation (1.67) must be construed as the union of boundaries of all dielectric particles, while $\sigma_k(M)$ (and $\tau_k(M)$) are defined on this union. In many applications, nanoparticles are located on some dielectric substrates. In this

case, the Green's function in (1.67) must be replaced with the following:

$$\sigma_k(Q) = \frac{\lambda_k}{2\pi} \oint_S \sigma_k(M) \mathbf{n}_Q \cdot \nabla_Q [G(Q, M)] dS_M, \quad (1.71)$$

where

$$G(Q, M) = \frac{1}{r_{MQ}} - \frac{\varepsilon_s - \varepsilon_0}{\varepsilon_s + \varepsilon_0} \frac{1}{r_{M'Q}}. \quad (1.72)$$

Here, ε_s is the permittivity of the substrate, and M' is the image of M with respect to the substrate plane. The idea is based on the method of image charge. It is important to mention that the dielectric substrate is not only a structural part of the design, but it also results in the downward (red) shift of plasmon resonance frequencies.

It is apparent that the mathematical structure of integral equation (1.67) is invariant with respect to the scaling of S , i.e., the scaling of the dimensions of the particle. This leads to the unique property of electrostatic (plasmon) resonances: resonance frequencies depend on particle shape, but they are scale invariant with respect to particle dimensions, provided that they remain appreciably smaller than the free-space wavelength. We summarize this section by presenting the computational results of the eigenmode technique and analytical solution. Figure 1.8 displays the corresponding plasmon modes for the toroids with $x_0/R = 10$, and Figure 1.9 shows the comparison between the resonance permittivities obtained by the eigenmode method and the analytical solution.

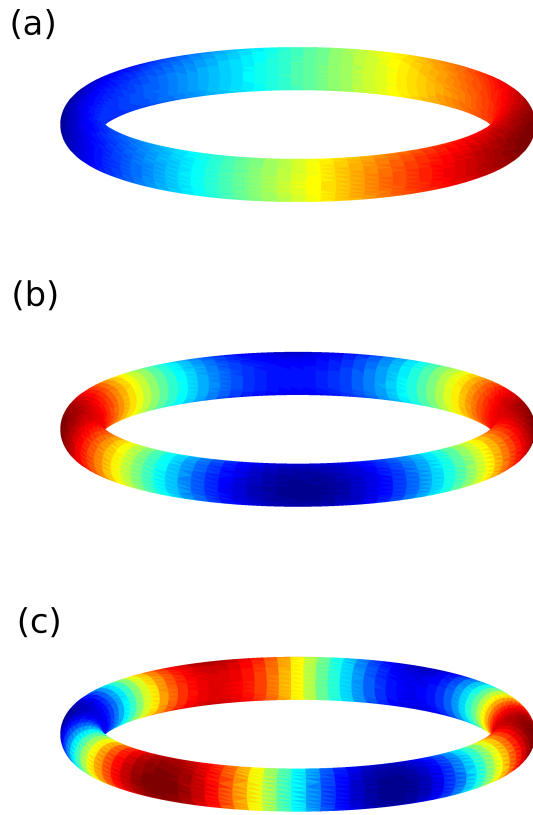


Figure 1.8: Plasmon modes in toroids with $x_0/R = 10$: (a) $n = 0, m = 1$; (b) $n = 0, m = 2$; (c) $n = 0, m = 3$.

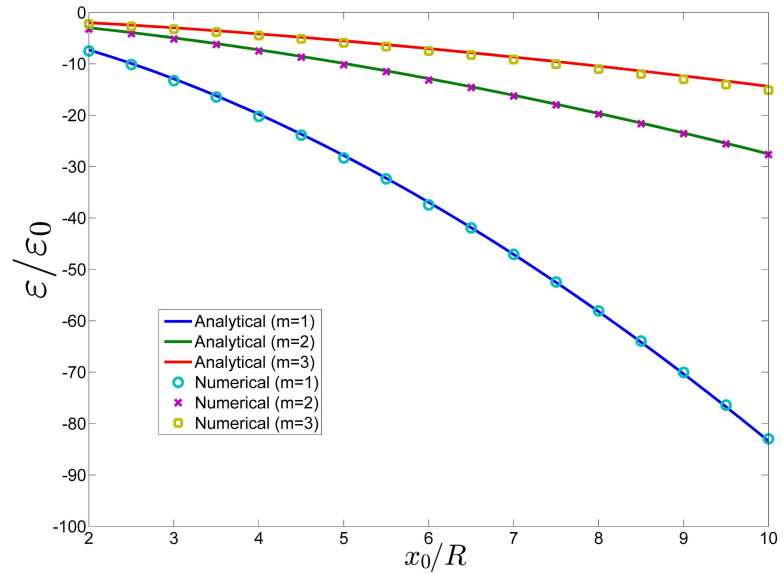


Figure 1.9: Comparison of resonance permittivities calculated by the eigenmode method and analytical solution for mode $m = 1, m = 2, m = 3$ ($n = 0$ for all).

1.4 Excitation of Plasmon Modes in Metallic Nanoparticles

Next, we consider how the plasmon modes can be excited by optical radiation. During the excitation process, the actual boundary charges $\sigma_k(M, t)$ induced on the metallic nanoparticle boundary can be expanded in terms of plasmon modes $\sigma_k(M)$ as

$$\sigma_k(M, t) = \sum_{k=1}^{\infty} a_k(t) \sigma_k(M), \quad (1.73)$$

where $a_k(t)$ is the expansion coefficient corresponding to the k th plasmon mode. It is apparent that the magnitude of this expansion coefficient determines which plasmon modes will be strongly excited. To derive $a_k(t)$, we have to utilize the biorthogonality property of $\sigma(M)$ and $\tau(M)$. Since the nanoparticle is dispersive and exhibits nonlocal-in-time constitutive relation, the frequency domain technique is employed. It has been demonstrated [26] that in the case when the incident field is uniform and has the same frequency ω_k as the resonance frequency of a specific k th plasmon mode, the steady-state value of this expansion coefficient is given by the formula

$$a_k^{ss}(t) = -(\mathbf{E}_0 \cdot \mathbf{p}_k) \frac{\varepsilon'(\omega_k) - \varepsilon_0}{\varepsilon''(\omega_k)} \cos \omega_k t, \quad (1.74)$$

where \mathbf{E}_0 is the electric field of the incident laser radiation, \mathbf{p}_k is the dipole moment of the k th plasmon mode, and $\varepsilon''(\omega_k)$ is the imaginary part of particle dielectric permittivity at frequency ω_k . Formula (1.74) reveals the physical mechanism of coupling of incident laser radiation to the plasmon modes. It shows the resonance magnitude depends on the ratio of real to imaginary parts of dielectric permittivity at the resonance frequency, and the spatial orientation of the incident field with

respect to the dipole moment of the plasmon mode. When the uniformly incident field has different frequency ω_0 , the steady-state value of this expansion coefficient is given by the formula

$$a_k^{ss}(t) = (\mathbf{E}_0 \cdot \mathbf{p}_k) C(\omega_0) \cos(\omega_0 t + \varphi), \quad (1.75)$$

where

$$C(\omega_0) = \sqrt{\frac{[\varepsilon'(\omega_0) - \varepsilon_0]^2 + [\varepsilon''(\omega_0)]^2}{[\varepsilon_k - \varepsilon'(\omega_0)]^2 + [\varepsilon''(\omega_0)]^2}}. \quad (1.76)$$

Formula 1.76 reveals that the quality of plasmon resonances is controlled by the ratio of real to imaginary parts of the particle dielectric permittivity at the resonance frequency. For gold and silver, this ratio is most appreciable when the free-space wavelength is within the ranges of 650-1000 nm and 800-1100 nm (see Figures 1.10 and 1.11) for gold and silver, respectively. For this reason, plasmon resonances in gold and silver nanoparticles can be most efficiently excited in the corresponding frequency ranges. $C(\omega_0)$ is also very instrumental for evaluations of the width of plasmon resonances, which reveals the sharpness of plasmon resonances (see Figure [?]).

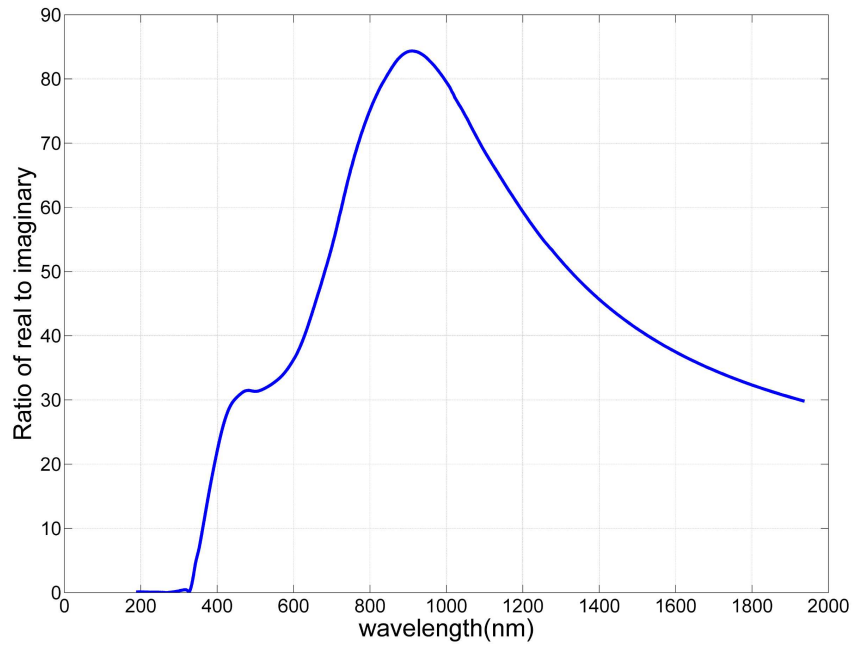


Figure 1.10: The ratio of real to imaginary parts of dielectric permittivity of silver.

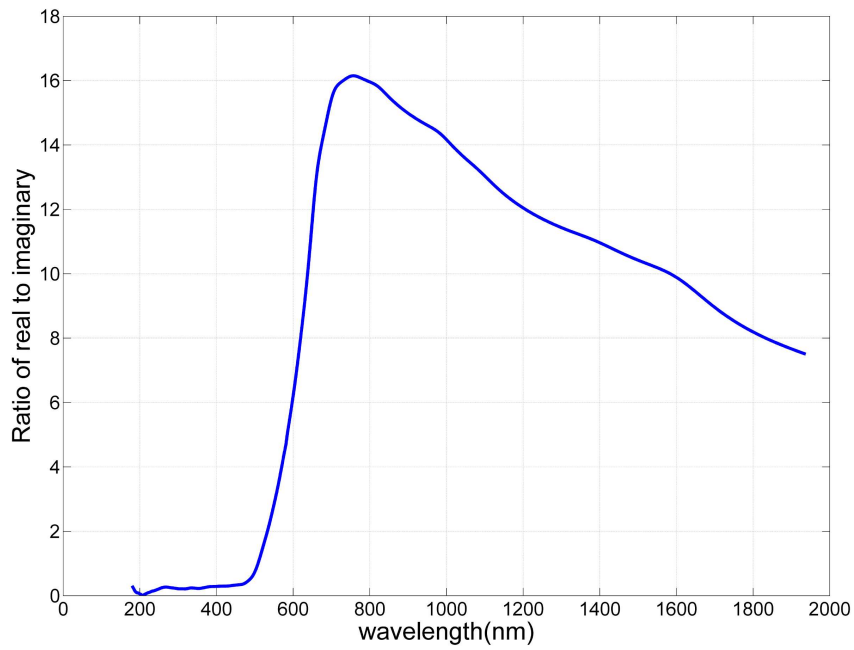


Figure 1.11: The ratio of real to imaginary parts of dielectric permittivity of gold.

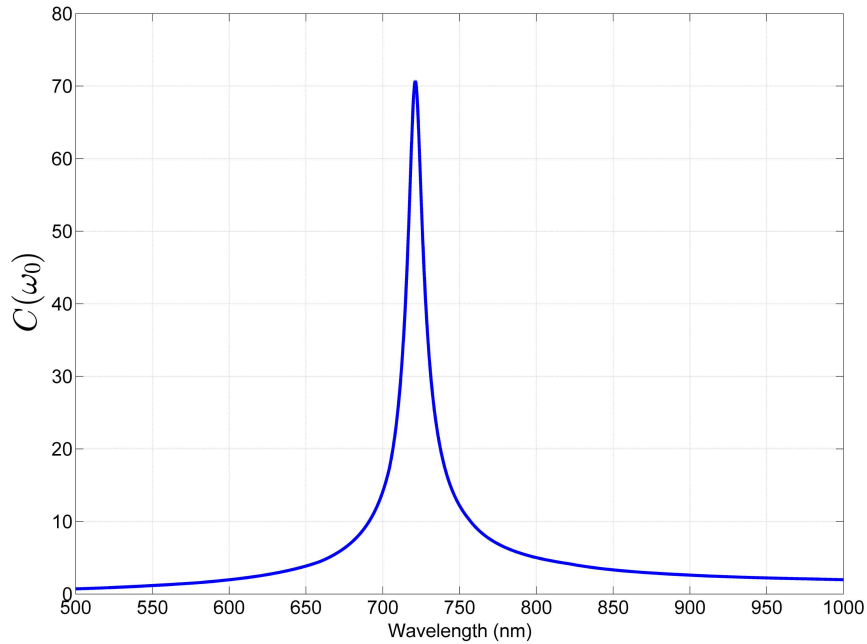


Figure 1.12: Computed $C(\omega_0)$ for spherical nanoshell (outer radius/inner radius = 4/3) with dielectric core permittivity $\varepsilon_c = 11.32$.

1.5 Computation of Extinction Cross Sections of Metallic Nanoparticles Subject to Optical Radiation

Experimentally, the resonance frequencies of metallic nanoparticles are determined by the peak positions in the extinction cross section spectrum. It turns out the eigenmode approach can be extended to calculate the extinction cross sections of resonant metallic nanoparticles subject to optical radiation. Consider an incident plane wave scattered by a nanoparticle of arbitrary shape with permittivity $\varepsilon(\omega)$ surrounded by a homogeneous medium with permittivity ε_0 . It has been demonstrated that the following inhomogeneous boundary integral equation can be derived [28]:

$$\sigma(Q) - \frac{\lambda}{2\pi} \oint_S \sigma(M) \frac{\vec{r}_{MQ} \cdot \vec{n}_Q}{r_{MQ}^3} dS_M = -2\lambda\varepsilon_0 \vec{n}_Q \cdot \vec{e}_{in}(Q), \quad (1.77)$$

where

$$\lambda = \frac{\varepsilon(\omega) - \varepsilon_0}{\varepsilon(\omega) + \varepsilon_0} \quad (1.78)$$

and $\vec{e}_{in}(Q)$ is the incident electric field at point Q . The scattered electric fields can be computed (in zero order) as follows:

$$\vec{E}_0^\pm = -\nabla \left[\frac{1}{4\pi\varepsilon_0} \oint_S \frac{\sigma_0(M)}{r_{MQ}} dS_M \right]. \quad (1.79)$$

The outlined approach can be easily extended to the case when nanoparticles are placed on a dielectric substrate by replacing the free-space Green's function by the one which takes into account the substrate as shown in Sec. 1.3. Subsequently, by using the optical theorem [27], the extinction cross section (ECS) of nanoparticles can be computed. The essence of the optical theorem is that ECS can be expressed in terms of the scattered far field in the forward direction,

$$\sigma_{ext} = \frac{4\pi}{k} \text{Im}[\hat{a}_i \cdot \vec{f}], \quad (1.80)$$

where σ_{ext} stands for the extinction cross section, k is wave number, \hat{a}_i is the unit polarization vector of the incident wave, and \vec{f} is the forward scattering amplitude. It has been shown [28] that ECS can be expressed in terms of dipole moment \vec{p} :

$$\sigma_{ext} = \frac{k}{\varepsilon_0} \text{Im} \left[\frac{\hat{a}_i \cdot (\vec{v} \times \vec{p}) \times \vec{v}}{E_0} \right], \quad (1.81)$$

where \vec{v} is a unit vector in the direction of wave propagation, and \vec{p} is the dipole moment defined as

$$\vec{p} = \oint_S \sigma(M) \vec{r}_{MQ} dS_M. \quad (1.82)$$

The technique has been software implemented and numerous computations have been performed. Figure 1.13 shows the computed extinction cross section of a

single silver nanosphere in vacuum with diameter of 20 nm, and the comparison with Mie theory [63]. It demonstrates the accuracy of our technique and the developed software. Figure 1.14 presents the computed extinction cross section of a single silver nanocube in water environment.

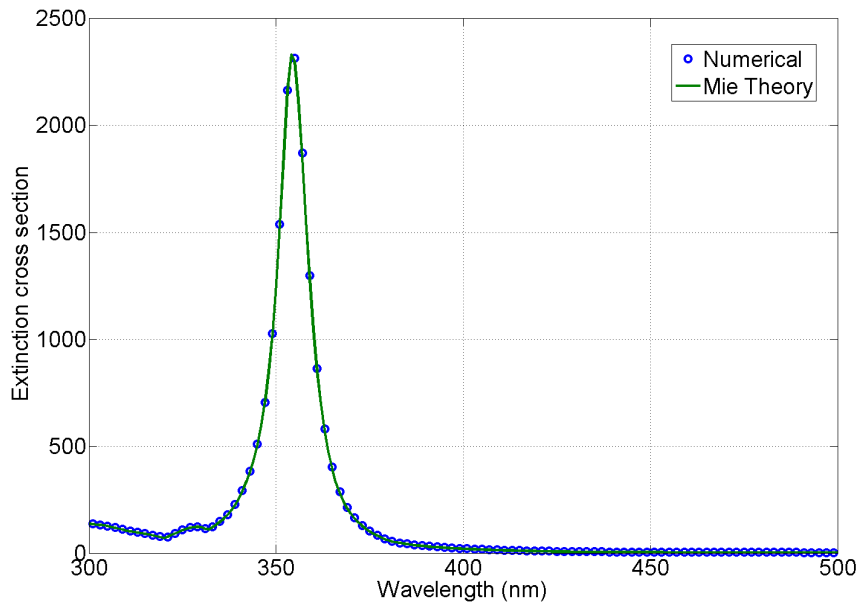


Figure 1.13: The comparison between calculated extinction cross section and Mie theory for a single silver sphere in vacuum environment.

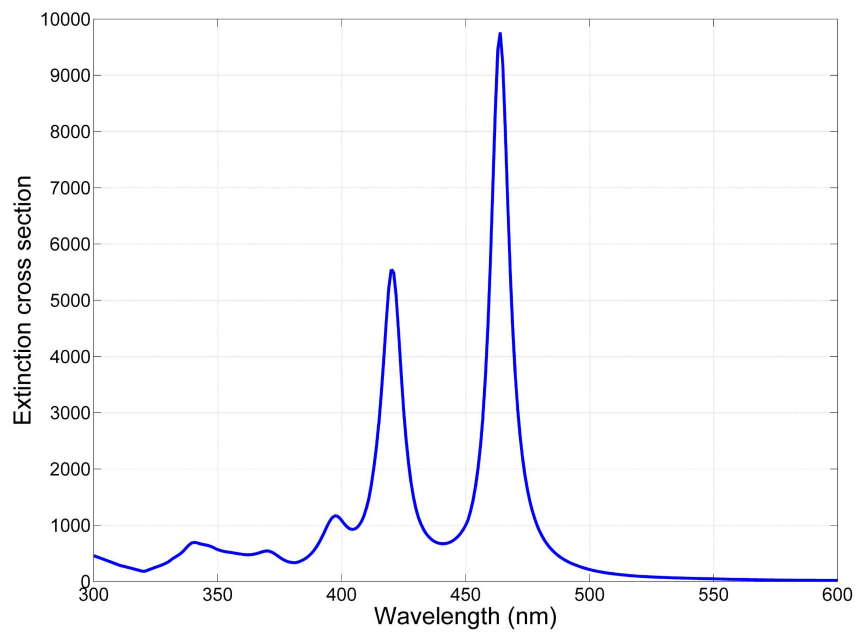


Figure 1.14: The calculated extinction cross section spectrum for a single silver cube in water environment.

1.6 Overview of Dissertation Contents

The modeling of plasmon resonances in metallic nanoparticles discussed in this chapter is the foundation of all numerical calculations and is extensively employed throughout this work. In Chap. 2, we study the surface-enhanced Raman scattering (SERS) enhancement factors of silver nanocube clusters (AgNC). We investigate the dispersion in the SERS enhancement factors of silver dimers (two cubes) on a pre-patterned silicon substrate. Three types of configurations of the dimers, which are edge-to-edge, face-to-edge, and face-to-face are considered. The numerical calculations are performed for different gaps in each configuration of the dimers. Our numerical results are compared to the experimental data collected by Prof. Rabin's group. The results show that the SERS enhancement factors are related to the resonance frequencies of the dimers, which are determined by their geometrical configurations (gap distances and orientations).

In Chap. 3, we deal with the plasmon modes in spheroidal nanoshells. Since nanoparticles with continuous rotational symmetry can preserve the helicity of circularly polarized light, spheroidal nanoshells are good candidates for the application to all-optical magnetic recording. We first derive the analytical solutions for plasmon modes in ellipsoidal nanoshells. From the derived formulas, the resonance frequency of dipolar plasmon modes can be tuned to the favorable frequency region by adjusting the aspect ratio and thickness of the nanoshells. Next, we derive the formulas which indicate how the dipolar plasmon modes in ellipsoidal nanoshells can be excited by uniformly incident field, as well as the electric field generated by dipolar

plasmon modes. Then we consider a special case of the ellipsoidal nanoshells, which is the case of spheroidal nanoshells. We compare the light intensities of the optical spots generated by the circularly polarized plasmon modes in spherical nanoshells and spheroidal nanoshells. The results suggest that the spheroidal nanoshells are more beneficial to all-optical magnetic recording as far as the light focusing and high light intensity are concerned.

In Chap. 4, we study the application of plasmon resonances to heat-assisted magnetic recording (HAMR). In the designs of recording heads for HAMR, the metallic nanostructures are surrounded by many components which may affect their plasmon resonances. In this chapter, we construct a constrained eigenvalue problem for specific boundary integral equations which accounts for the coupling between the surrounding parts and the metallic nanostructures. By using this technique, the resonance frequencies and the corresponding plasmon modes are computed for two metallic nanostructures with different substrates. The effect of heat sink layers on the plasmon resonances is also reported.

Finally, in Chap. 5, we study the radiation corrections of plasmon resonances in nanoparticles. In this chapter, we investigate the red-shifts in resonance frequencies of dipolar plasmon modes in a single silver nanocube with increasing cube size. We first present the numerical modeling of radiation corrections for plasmon resonances in nanoparticles, and demonstrate the consistency of the calculation results with Mie theory and available experimental data. Subsequently, we perform the same calculation for a single silver nanocube and compare the results with experimental measurement. The results show the multiplicity of the dipolar plasmon modes in a

single cube, and these dipolar plasmon modes correspond to the peaks in extinction cross section measurement. The calculation results also suggest that each of the dipolar plasmon modes has different sensitivity to the rounding of the cube corners and edges.

Chapter 2

Application of Plasmon Resonances to Surface-Enhanced Raman Scattering (SERS)

2.1 Introduction

When electromagnetic radiation irradiates an atom or a molecule, the energy may be transmitted, absorbed, or scattered. Based on the energy of the scattered photons, it is divided into two main categories. One is called Rayleigh scattering, in which the scattered photons have the same energy as the incident photons. The largest portion of the scattering is Rayleigh scattering, and it accounts for many natural phenomena, e.g., blue sky and red sunset. The other one is Raman scattering, in which the scattered photons have different energy from the incident photons. If the scattered photons have lower energy, it is known as Stokes Raman scattering. If they have higher energy than the incident radiation, it is called anti-Stokes Raman scattering. Figure 2.1 summarizes the mechanisms of different scattering processes. For Stokes Raman scattering, the light loses energy to various molecular vibrations. For anti-Stokes Raman scattering, the light obtains energy from the molecular vibrations. The Raman effect was first predicted by an Austrian theoretical physicist, Adolf Smekal. A few years later, this effect was experimentally demonstrated by C. V. Raman, who got the Nobel prize for this discovery in 1930. Therefore, this

effect is also referred to as the Smekal-Raman effect. Raman scattering becomes very important because it provides the fingerprint of a sample molecule. However, among the total scattering from a sample molecule, only a very small portion of scattering is Raman scattering. Its signal is so weak ($\sim 10^{-30} \text{ cm}^2$) that a technique for enhancing this signal is necessary.

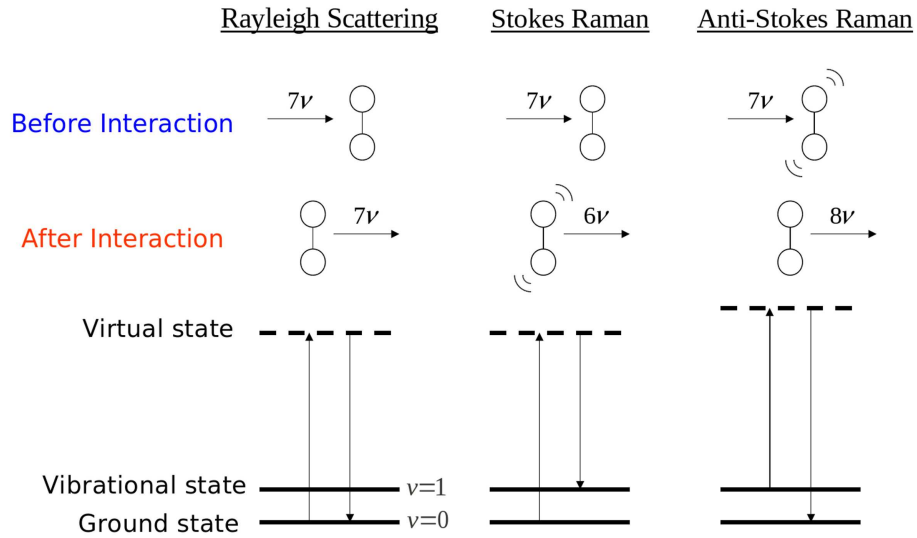


Figure 2.1: Schematic illustration of Raman and Rayleigh scattering.

Surface-enhanced Raman scattering (SERS) is a powerful technique that provides high sensitivity and high specificity for molecular spectroscopy ([29][30]). First, incident radiation excites the plasmon modes in a metallic nanoparticle. Then, the strong localized field created by the plasmon modes interacts with the surrounding molecules. These molecules generate another electric field at Raman frequency which excites the plasmon modes in the metallic nanoparticles once again. Finally, the resulting field from the plasmon resonance is measured. This is, in essence, the mechanism of SERS. A large volume of scientific work has been dedicated to determining the enhancement factor (EF). The molecular SERS signal is amplified and

varies by orders of magnitude from substrate to substrate, site to site, and target molecule to molecule. Because of this technique, the capabilities of detecting single molecule signal have been demonstrated ([31]-[37]).

Recently, a large volume of scientific works have reported the optical properties of small clusters of nanoparticles of well-defined shapes ([38]-[44]), and attributed the SERS phenomena to hot-spots in these nanostructures where molecules are located. It turns out the structural parameter plays an important role in determining resonance frequencies and hence the enhancement factors. In the present work, we start with the numerical calculations of resonance frequency and SERS enhancement factor for a silver nanocube (AgNC) monomer. Subsequently, we perform numerical calculations of resonance frequencies and SERS enhancement factors for AgNC dimers with various configurations within the dimers. After that, the experimental work done by Prof. Rabin's group is introduced, and the results are given in Sec. 2.3. Finally, the comparison between experimental data and calculation results is discussed in Sec. 2.4.

2.2 Mode Analysis of AgNC Clusters

2.2.1 Monomers

We first perform the calculations of plasmon resonance modes for a single AgNC monomer on silicon substrate ($\epsilon = 11.7\epsilon_0$). The AgNC monomer is situated 2 nm above the silicon surface to account for the presence of a native oxide and the molecules. Figure 2.2 shows the calculated charge distribution of the dipolar plas-

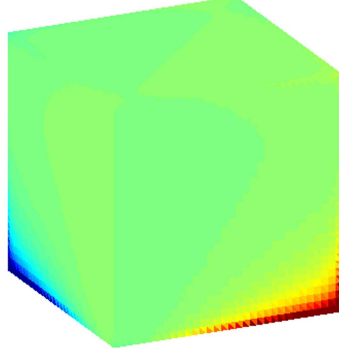


Figure 2.2: Calculated charge distribution for dipolar plasmon mode in AgNC monomer on silicon substrate. Red color and blue color represent the positive charges and negative charges, respectively.

mon mode for the AgNC monomer. The dipolar plasmon mode of the monomer has resonance wavelength of 533 nm, and the direction of its dipole moment is oriented along the diagonal of the bottom/top face. The calculated charge distribution is used to compute the electric field around the nanocube. As mentioned above, the SERS actually contains two stages of enhancement of incident radiation. Based on the two-stage enhancement, we compute the SERS enhancement factor by the following formula:

$$\text{SERS EF} = \frac{|\mathbf{E}(r; \omega_L)|^2}{|\mathbf{E}_0(\omega_L)|^2} \times \frac{|\mathbf{E}(r; \omega_R)|^2}{|\mathbf{E}_0(\omega_R)|^2}. \quad (2.1)$$

The last formula shows the fourth-power dependence of electric field and is widely used in many scientific papers on studying SERS. $|\mathbf{E}_0(\omega)|^2$ is the intensity of the uniform electric field of frequency ω which excites the plasmon resonance (dipole mode) and $|\mathbf{E}(\mathbf{r}; \omega)|^2$ is the intensity of the electric field generated by the plasmon mode at location \mathbf{r} . ω_L and ω_R are the frequencies of the incident laser radiation and Raman scattering light, respectively. Here, we neglect the fact that the excitation

of the plasmon mode by the Raman scattering light is not spatially uniform [45] and the resonance frequencies of plasmon modes may be altered due to the presence of the surrounding molecules ([46][47]). By using the above formula, we consider two cases of incident radiation wavelength and Raman scattering wavelength with different orientations of monomer. A layer of molecules is located 1 nm away from the nanocube. The calculation results are summarized in Table 2.1.

This result suggests that the EFs depend on the incident radiation wavelength, Raman-scattering light wavelength, and polarization with respect to the monomer. The larger enhancement factor for polarization oriented along the diagonal of the bottom/top face might be attributed to larger distance between positive charges and negative charges, which creates larger dipole moment. Table 2.1 shows larger enhancement factor for 514 nm laser light and 560 nm Raman-shifted light. The reason is that these two wavelengths are close to the resonance wavelength. Because of the sharpness of plasmon resonance, the resonance wavelength has to be situated somewhere between the laser wavelength and Raman-shifted wavelength (see Figure 2.3). The optimal case occurs when the resonance wavelength is located at the midpoint between incident radiation and Raman radiation wavelengths [46]. Table 2.1 is in good agreement with experimental work performed in [48] with 514 nm laser and 560 nm Raman-shifted light.

| λ_L (nm) | λ_R (nm) | Cube orientation | SERS EF |
|---------------------|---------------------|---|--------------------|
| 514 | 560 |  | 2.14×10^6 |
| | |  | 1.04×10^6 |
| 633 | 678 |  | 1.78×10^4 |
| | |  | 8.68×10^3 |

Table 2.1: Calculated SERS enhancement factors for AgNC monomer on silicon for different incident wavelength and Raman scattering wavelength with different cube orientations.

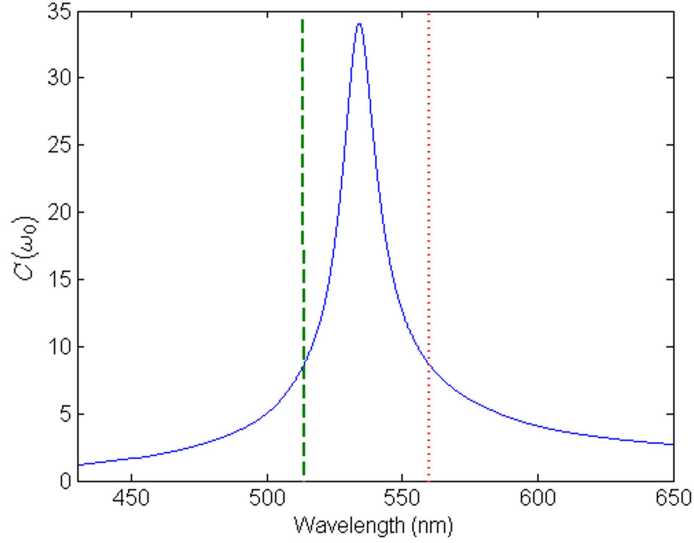


Figure 2.3: Calculated $C(\omega_0)$ for dipolar plasmon mode in AgNC monomer on silicon substrate. Green (dashed) line represents the wavelength of incident laser and red (dot) line represents Raman-shifted wavelength.

2.2.2 Dimers

Next, we consider the case of AgNC dimers. The difference between dimer and monomer is that the dimer has more configurations, including distances of gaps,

orientation of each cube within a dimer, and lateral shift in space of one cube to the other. To simplify this problem, we consider various gap distances in three types of dimer configurations: (1) face-to-face dimers (FF); (2) face-to-edge dimers (FE); and (3) edge-to-edge dimers (EE). Figure 2.4 shows the schematic illustration of these three types of dimer configurations. By solving the eigenvalue problem

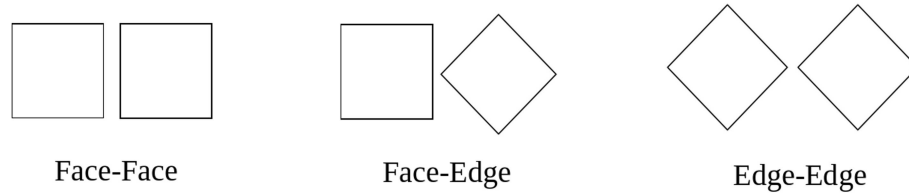


Figure 2.4: Schematic illustration of three configurations of dimers.

for each configuration of dimer, we obtain the resonance wavelengths of the dipolar plasmon modes and the charge distributions with different gap distances. Figure 2.5 shows the charge distributions of dipolar plasmon mode for each configuration of dimer with 4 nm gap. Table 2.2 summarizes the resonance wavelengths of their dipolar plasmon modes with various gap distances. It can be seen that for small gaps, face-to-face dimers have larger resonance wavelengths than face-to-edge dimers and edge-to-edge dimers. However, it is also shown that the resonance wavelengths in face-to-face dimers are very sensitive to the gap distances, compared with the other two cases. As we mentioned, in order to obtain high SERS enhancement factors, the laser wavelengths or Raman-shifted wavelengths should be as close to resonance wavelengths as possible. If we consider 633 nm light source and 678 nm Raman-shifted light, face-to-face dimers should have larger enhancement factors than the other two cases for small gaps. Table 2.3 summarizes the SERS

| | FF | FE | EE |
|----------|---------------------------|---------------------------|---------------------------|
| gap (nm) | resonance wavelength (nm) | resonance wavelength (nm) | resonance wavelength (nm) |
| 3.0 | 604.63 | 577.48 | 569.03 |
| 3.5 | 595.61 | 573.58 | 567.12 |
| 4.0 | 589.08 | 570.52 | 565.35 |
| 4.5 | 583.73 | 568.03 | 563.74 |
| 5.0 | 578.43 | 565.95 | 562.27 |
| 5.5 | 573.13 | 564.19 | 560.95 |
| 6.0 | 567.78 | 562.67 | 559.74 |
| 6.5 | 562.18 | 561.34 | 558.64 |
| 7.0 | 556.32 | 560.17 | 557.63 |
| 7.5 | 550.38 | 559.12 | 556.71 |
| 8.0 | 544.74 | 558.17 | 555.87 |
| 8.5 | 539.46 | 557.32 | 555.08 |
| 9.0 | 534.54 | 556.53 | 554.36 |
| 9.5 | 530.00 | 555.82 | 553.69 |
| 10.0 | 525.79 | 555.16 | 553.07 |

Table 2.2: Calculated resonance wavelengths for 80 nm silver nanocube dimers on silicon substrate.

| | FF | FE | EE |
|----------|--------------------|--------------------|--------------------|
| gap (nm) | SERS EF | SERS EF | SERS EF |
| 3.0 | 6.77×10^6 | 1.19×10^6 | 6.95×10^5 |
| 3.5 | 1.63×10^6 | 6.87×10^5 | 5.01×10^5 |
| 4.0 | 7.71×10^5 | 4.43×10^5 | 3.77×10^5 |
| 4.5 | 4.80×10^5 | 3.10×10^5 | 2.96×10^5 |
| 5.0 | 3.49×10^5 | 2.32×10^5 | 2.40×10^5 |
| 5.5 | 2.75×10^5 | 1.82×10^5 | 2.00×10^5 |
| 6.0 | 2.18×10^5 | 1.49×10^5 | 1.71×10^5 |
| 6.5 | 1.59×10^5 | 1.26×10^5 | 1.48×10^5 |
| 7.0 | 1.02×10^5 | 1.09×10^5 | 1.31×10^5 |
| 7.5 | 5.82×10^4 | 9.62×10^4 | 1.18×10^5 |
| 8.0 | 3.21×10^4 | 8.64×10^4 | 1.07×10^5 |
| 8.5 | 1.79×10^4 | 7.85×10^4 | 9.78×10^4 |
| 9.0 | 1.04×10^4 | 7.22×10^4 | 9.04×10^4 |
| 9.5 | 6.19×10^3 | 6.70×10^4 | 8.42×10^4 |
| 10.0 | 4.07×10^3 | 6.27×10^4 | 7.89×10^4 |

Table 2.3: Calculated SERS enhancement factors for 80 nm silver nanocube dimers on silicon substrate (Incident wavelength = 633 nm; scattered wavelength = 678 nm).

enhancement factors for these three cases with various gap distances. Indeed, the results shows that face-to-face dimers have larger SERS enhancement factors, but their enhancement factors are sensitive to the gap distances. Compared with face-to-face dimers, face-to-edge and edge-to-edge dimers have relatively stable enhancement factors throughout various gap distances, which may be beneficial to SERS signal detection in experiment. Our numerical simulation is complemented by experimental work performed by Rabin *et al.* which is presented in the next section.

2.3 Experimental Method

2.3.1 Preparation of AgNC Clusters on Patterned Substrate

First, square arrays of 200 nm diameter pores on silicon substrate were established by using conventional e-beam lithography. The dry etch was carried out in a reactive ion etching system (Trion Tech.) using a SF₆/O₂ gas mixture (50:10 sccm) at a power of 100 W for 10 s. The etch depth was 90-100nm. The patterned substrate was immersed vertically in a suspension of AgNCs in water and slowly pulled out by means of a motorized stage at the speed of 0.3 mm/h. During the pulling out process, the AgNC clusters fall in the pores of the patterned substrate due to capillary force (see Figure 2.6). Excess AgNCs on the surface were removed by gentle brushing. The substrate was then immersed in a 0.2 mM 4-ABT solution in ethanol for 3 h to coat AgNC clusters with a self-assembled monolayer of thiol molecules (4-aminobenzenethiol, 4-ABT) which served as Raman dyes. Finally, the substrate was rinsed extensively with ethanol and dried under nitrogen. Figure 2.7

presents the patterned substrate and dimers of AgNC in the cavities of the patterned substrate. Each cavity is isolated from the others and can be probed individually by the laser beam of the micro-Raman system and by electron microscopy.

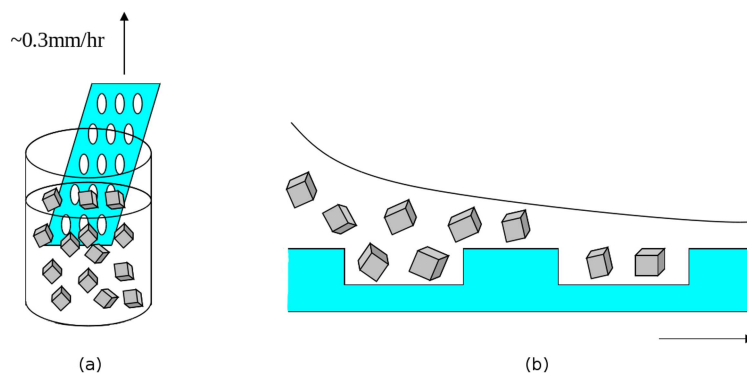


Figure 2.6: Schematic illustration of vertical deposition. With the patterned substrate being slowly pulled out, the AgNC clusters fall into the pores due to capillary force.

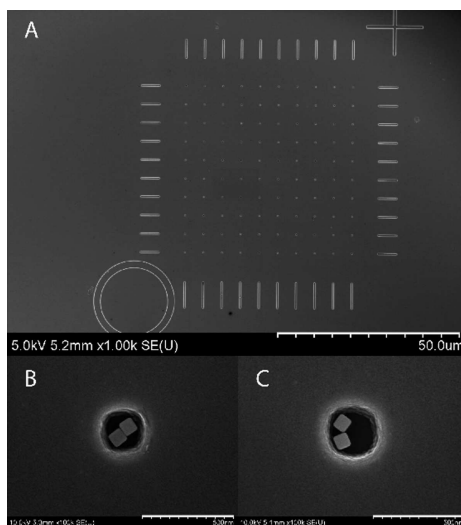


Figure 2.7: (a) SEM image of the patterned substrate before the vertical deposition process; (b) and (c) show dimers of AgNCs (average edge length = 80 nm) that have been formed in the cavities of the patterned substrate.

2.3.2 Identification of the AgNC Clusters

In order to elucidate the parameters playing a significant role in the enhancement of Raman scattering, we investigate the measurement results of a large collection (>200) of AgNC dimers. All dimers consist of two nanocubes, separated by less than 10 nm. The average side length of the cubes is 80 nm. Since the dimer in each cavity usually has different orientation from the three ideal cases, it is necessary to categorize each dimer in these three groups. Figure 2.8 shows a general orientation for one dimer. We first identify the corner of one cube which is closest to a face of the adjacent cube and assign the corner point P. Then we draw a line through point P which is perpendicular to the face of the adjacent cube, and have a segment of the side length a of the cube denoted as d . The θ is the angle between the two adjacent faces from two different cubes which face each other. The assignment of the dimer type as EE, FE, or FF is summarized in Table 2.4. After this assignment, 74 dimers are categorized as edge-to-edge dimers, 42 dimers are categorized as face-to-edge dimers, and 92 dimers are categorized as face-to-face dimers.

| $d > \frac{2a}{3}$ | | $d < \frac{2a}{3}, d' < \frac{2a}{3}$ | |
|---------------------|----|--|----|
| $\theta > 10^\circ$ | EE | $\theta < 10^\circ$ or $\theta > 80^\circ$ | FF |
| $\theta < 10^\circ$ | FF | $10^\circ < \theta < 80^\circ$ | FE |

Table 2.4: Details of assignment of the dimer type as EE, FE, or FF based on geometrical factors.

2.3.3 Raman Spectra Analysis and Calculation of the SERS Substrate Enhancement Factor

The Raman signal intensity is quantified as the integrated peak area for the carbon-sulfur bond stretch of 4-ABT at 1078 cm^{-1} in each spectrum. A reference Raman spectrum of a 1.0 M solution of 4-ABT in 1,5-pentanediol was measured, and the Raman signal intensity per molecule was calculated assuming a cylindrical focal volume of $\phi 2.2\ \mu\text{m} \times 16\ \mu\text{m}$ (Diameter \times Height). The SERS substrate enhancement factor (SSEF) is as defined by Etchegoin *et al.* [49] and calculated by the following formula:

$$\text{SSEF} = \frac{\frac{I_{SERS}}{N_{SERS}}}{\frac{I_{REF}}{N_{REF}}} = \frac{I_{SERS}}{N_{SERS}} \times \frac{N_{REF}}{I_{REF}}, \quad (2.2)$$

where I_{SERS} is the Raman signal intensity for SERS, N_{SERS} is the number of molecules probed for SERS, I_{REF} is the Raman signal intensity for normal Raman spectrum, and N_{REF} is the number of molecules probed for normal Raman setting. N_{REF} is determined based on the focal volume of our Raman system, while a monolayer of 4-ABT molecules with a density of 5 molecules/nm² is assumed on the six {001} facets of the AgNCs [58].

Figure 2.9 shows the SSEFs were collected in a diminishing sorted list for each group. The cumulative distribution function is fitted by so-called Weibull distribution $F_{\text{Weibull}}(x) = 1 - \exp\{-(x/b)\}^c$, where b is the scaling parameter and c is known as the shape parameter ([50][51]). This model presents a quantity which is sensitive to the nanoscale details of the metal structure with a large number of degrees of freedom. The scaling parameter indicates the *average magnitude* of the

enhancement factor that can be achieved, while the shape parameter indicates the *sensitivity* of the enhancement factor to deviations from the optimal cluster configuration. Table 2.5 summarizes the scaling parameter and shape parameter for each type of dimer. As seen in Figure 2.9, the strongest enhancement is observed in EE dimers. This seems to mean that the highest SSEF is associated with a dimer of EE type. However, Table 2.5 suggests that the average enhancement factors of FE dimers are a factor of ~ 2.4 higher than the average enhancement factors of EE dimers. Also, the shape parameters of the SSEF distributions for the EE dimers and FE dimers are indistinguishable, while that of SSEF distributions for the FF dimers has a higher value. This is consistent with the numerical calculation which shows the high sensitivity of SERS enhancement factors to the geometrical factor (gap distances). The ranking of the dimer types based on our analysis of

| | EE dimers | FE dimers | FF dimers |
|-----------------|-------------------|-------------------|-------------------|
| shape parameter | 0.196 ± 0.014 | 0.205 ± 0.017 | 0.284 ± 0.021 |
| scale parameter | 4483 ± 613 | 10812 ± 1510 | 5237 ± 683 |

Table 2.5: Parameters obtained from the Weibull distribution model.

ensemble dimers is $FE > FF > EE$, which is not the ranking suggested by Xia *et al.* ($FF > FE > EE$) [48]. This is not to say there is discrepancy in the two studies. For comparison, we also compare our simulation results with the experimental results from Xia *et al.* [48], where similar dimer configurations have been studied for incident laser radiation wavelength of 514.5 nm and a Raman-shifted radiation wavelength of 560 nm. The results of our computations are shown in Table 2.6 for the FF configuration, and they are consistent with the experimental observation

from the referenced work [48] where a Raman enhancement factor of 2.0×10^7 was obtained.

| gap (nm) | resonance wavelength (nm) | SERS EF |
|----------|---------------------------|--------------------|
| 5 | 589.08 | 5.18×10^5 |
| 5.625 | 583.73 | 8.22×10^5 |
| 6.25 | 578.43 | 1.48×10^6 |
| 6.875 | 573.13 | 3.10×10^6 |
| 7.5 | 567.78 | 7.59×10^6 |
| 8.125 | 562.18 | 1.80×10^7 |
| 8.75 | 556.32 | 1.58×10^7 |
| 9.375 | 550.38 | 6.50×10^6 |
| 10 | 544.74 | 2.98×10^6 |

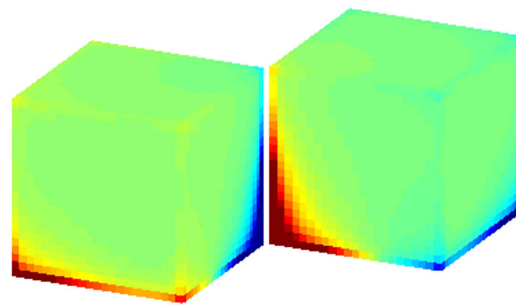
Table 2.6: Calculated resonance wavelengths and SERS enhancement factors for 100 nm silver nanocube face-to-face dimers on silicon (Incident wavelength = 514 nm; scattered wavelength = 560 nm).

Based on Table 2.6, we know that even for the same dimer, the SERS enhancement factor will be different with different excitation wavelength. Since the two studies are carried out using different excitation wavelengths, their SERS enhancement factors are supposed to vary in such a way that affects the ranking of the dimer types.

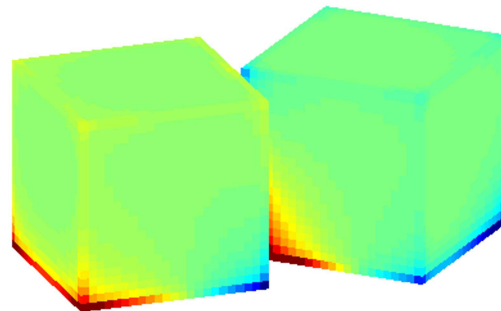
2.4 Conclusion

We explored the dispersion of SERS enhancement factors of silver nanocubes on a patterned silicon substrate. A novel technique has been developed to control the locations of clusters of nanocubes on the substrate. This approach allowed for the acquisition of Raman spectra and microscopy images of individual AgNC dimers without bias. Both numerical calculations and experimental data indicate that the

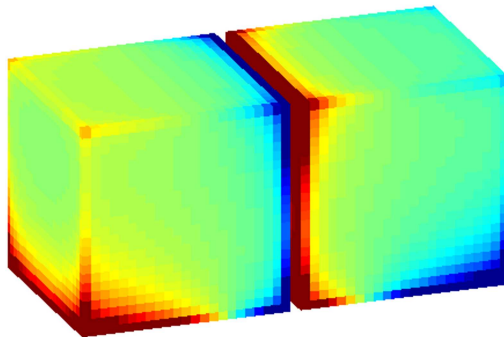
SERS enhancement factors of face-to-face dimers are more sensitive to the deviation from the optimal cluster configuration. Our results also show that the excitation wavelength with respect to resonance wavelengths of dimers plays an important role in determining SERS enhancement factors. The proper tuning of laser wavelength to plasmon resonance wavelength (or the other way around) can be beneficial to SERS enhancement. The key result of this study is that the azimuthal orientation of nanocubes in the dimer affects the dispersion of enhancement factors observed in a large group of dimers. Since most fabrication techniques cannot reproduce a patterned surface at the atomic scale, SERS substrates are destined to have nanoscale structural variations from site to site, as exhibited by the library of structures used in our study. In the real-world applications, the plasmonic structures for SERS substrate made of AgNC dimers have to be designed to achieve high signal enhancements as well as to minimize the heterogeneity of the SSEF. Our study indicates that substrates containing aligned face-to-edge dimers should be considered the most suitable for practical applications, as they display the highest uniformity in their SSEFs and the highest average value of SSEF.



(a)



(b)



(c)

Figure 2.5: Calculated charge distributions for (a) edge-to-edge dimers; (b) edge-to-face dimers; and (c) face-to-face dimers with 4 nm gap. Red color and blue color represent the positive charges and negative charges, respectively.

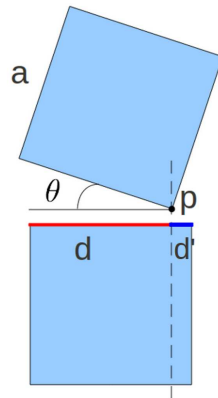


Figure 2.8: Schematic of a general configuration for one dimer.

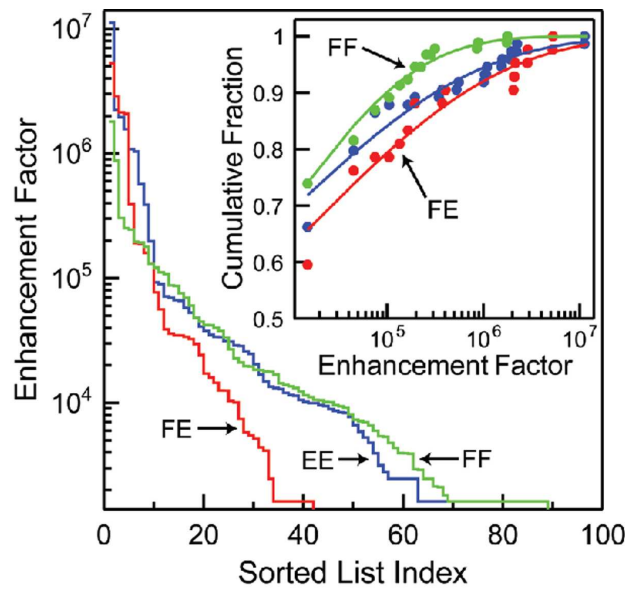


Figure 2.9: SERS substrate enhancement factors for EE dimers (blue), FE dimers (red), and FF dimers (green). Inset: Experimental cumulative fractions and fit to the Weibull distribution model (solid circles, experimental data; solid lines, fit values; the colors have the same meaning as above).

Chapter 3

Application of Plasmon Resonances to All-optical Magnetic Recording

3.1 Overview

Since Rasing *et al.* have recently demonstrated [52] that femtosecond magnetization reversals of 100 μm spots of magnetic media can be achieved by using only circularly polarized laser pulses, a large volume of related research has been reported ([53]-[59]). Circularly polarized light acts as an effective DC magnetic field parallel to the direction of light propagation, whose actual direction is controlled by the helicity of the circularly polarized light. This is a phenomenon resulting from the Inverse Faraday Effect [60]. It is currently believed that these magnetization reversals occur due to the combination of the local laser heating of magnetic media close to the Curie temperature and the simultaneous action of circularly polarized light as a magnetic field with the direction parallel to the light wave vector. Furthermore, right- and left-handed circularly polarized waves act as magnetic fields of opposite directions. This may be explained by the fact that the magnetic field and magnetization are not true vectors but rather axial (or pseudo-) vectors whose directions are reversed as a result of transitions from right- and left-handed coordinate systems. This suggests that right- and left-handed circularly polarized light

waves may break the symmetry in the same way as applied magnetic fields. It is apparent that this all-optical magnetization switching will be technologically feasible in magnetic recording only if the techniques for delivery of nanoscale-focused circularly polarized light are developed.

In the present work, we provide the analytical solution of plasmon resonances in an ellipsoidal nanoshell. The investigation of the properties of dipolar plasmon modes with various aspect ratios, thicknesses, and dielectric cores is presented. We compare the light intensities generated by circularly polarized plasmon modes in a spherical nanoshell and an ellipsoidal nanoshell, and the result shows that the ellipsoidal nanoshell has stronger light enhancement and a more focused light spot, which can serve as a promising design for delivery of circularly polarized light.

3.2 Introduction of Ellipsoidal Harmonics

3.2.1 Ellipsoidal Coordinate System

The potential problems involving the ellipsoidal boundaries can be solved by the use of ellipsoidal coordinates. The ellipsoidal coordinates consist of the following three families of coordinate surfaces: (i) Ellipsoids ($\xi = \text{constant}$)

$$\frac{x^2}{\xi^2} + \frac{y^2}{\xi^2 - h^2} + \frac{z^2}{\xi^2 - k^2} = 1 \quad , \quad k^2 \leq \xi^2 \leq \infty \quad (3.1)$$

(ii) Hyperboloids of one sheet ($\eta = \text{constant}$)

$$\frac{x^2}{\eta^2} + \frac{y^2}{\eta^2 - h^2} + \frac{z^2}{\eta^2 - k^2} = 1 \quad , \quad h^2 \leq \eta^2 \leq k^2 \quad (3.2)$$

(iii) Hyperboloids of two sheets ($\zeta = \text{constant}$)

$$\frac{x^2}{\zeta^2} + \frac{y^2}{\zeta^2 - h^2} + \frac{z^2}{\zeta^2 - k^2} = 1 \quad , \quad 0 \leq \zeta^2 \leq h^2 \quad (3.3)$$

where $k = \sqrt{a^2 - c^2}$, $h = \sqrt{a^2 - b^2}$, and here we choose $a \geq b \geq c$. a , b , and c are the semidiameters of the reference ellipsoid. The entire ellipsoidal coordinate system is based on the choice of a , b , and c . Different choices of (a, b, c) give different ellipsoidal coordinate systems. The following is the relation between ellipsoidal coordinates and Cartesian coordinates:

$$x^2 = \frac{\xi^2 \eta^2 \zeta^2}{h^2 k^2} \quad (3.4)$$

$$y^2 = \frac{(\xi^2 - h^2)(\eta^2 - h^2)(h^2 - \zeta^2)}{h^2(k^2 - h^2)} \quad (3.5)$$

$$z^2 = \frac{(\xi^2 - k^2)(k^2 - \eta^2)(k^2 - \zeta^2)}{k^2(k^2 - h^2)}. \quad (3.6)$$

3.2.2 Lamé Equations and Lamé Functions

Let us consider the Laplace equation in ellipsoidal coordinates. After applying the technique of separation of variables in the ellipsoidal coordinate system, the solution is in the following form:

$$\psi = F(\xi)G(\eta)H(\zeta). \quad (3.7)$$

By substituting 3.7 into the Laplace equation in ellipsoidal coordinates, we end up with the following Lamé equation [62][67][68]:

$$\begin{aligned} (\xi^2 - h^2)(\xi^2 - k^2) \frac{d^2 F(\xi)}{d\xi^2} + \xi(2\xi^2 - h^2 - k^2) \frac{dF(\xi)}{d\xi} \\ + \{(h^2 + k^2)q - p(p+1)\xi^2\} F(\xi) = 0. \end{aligned} \quad (3.8)$$

Exactly the same equations can be obtained for variables η and ζ . The parameters p and q are the separation constants. The solution to the Lamé equation can be found by the use of power series. Then we can get the Lamé functions of the first kind, of degree n and order m , which are denoted by E_n^m . For each degree n , there are $2n+1$ different solutions altogether, labeled by index m . Based on different choices of m and q , there are four different classes of solutions of the Lamé equation: $K(\lambda)$, $L(\lambda)$, $M(\lambda)$, and $N(\lambda)$. The few lowest and most used Lamé functions are listed in the following [62]:

$$\begin{aligned}
E_0^1(\lambda) &= K_0(\lambda) = 1, \\
E_1^1(\lambda) &= K_1(\lambda) = \lambda, \\
E_1^2(\lambda) &= L_1(\lambda) = \sqrt{\lambda^2 - h^2}, \\
E_1^3(\lambda) &= M_1(\lambda) = \sqrt{\lambda^2 - k^2}, \\
E_2^{1,2}(\lambda) &= K_2^\mp(\lambda) = \lambda^2 - \{k^2 + h^2 \mp \sqrt{k^4 + h^4 - k^2 h^2}\}/3, \\
E_2^3(\lambda) &= L_2(\lambda) = \lambda\sqrt{\lambda^2 - h^2}, \\
E_2^4(\lambda) &= M_2(\lambda) = \lambda\sqrt{\lambda^2 - k^2}, \\
E_2^5(\lambda) &= N_1(\lambda) = \sqrt{(\lambda^2 - h^2)(\lambda^2 - k^2)}. \tag{3.9}
\end{aligned}$$

3.2.3 Ellipsoidal Harmonics

Since the Lamé functions of the first kind are regular at the origin and have poles at infinity, the ellipsoidal harmonic which is regular at the origin can be written

in terms of the Lamé product, which is

$$\Theta_n^m(\mathbf{r}) = E_n^m(\xi)E_n^m(\eta)E_n^m(\zeta). \quad (3.10)$$

Correspondingly, the ellipsoidal harmonic which is regular at infinity can be written as

$$\Pi_n^m(\mathbf{r}) = F_n^m(\xi)E_n^m(\eta)E_n^m(\zeta), \quad (3.11)$$

where $F_n^m(\xi)$ is the Lamé function of the second kind, which is derived from the corresponding function of the first kind through

$$F_n^m(\xi) = (2n + 1)E_n^m(\xi) \int_{\xi}^{\infty} \frac{d\xi'}{[E_n^m(\xi')]^2 \sqrt{(\xi'^2 - h^2)(\xi'^2 - k^2)}}. \quad (3.12)$$

When ξ goes to infinity, $F_n^m(\xi)$ is in the expression which corresponds to the $1/r^{n+1}$ term in the spherical coordinate system.

3.3 Boundary Value Problem in an Ellipsoidal Nanoshell

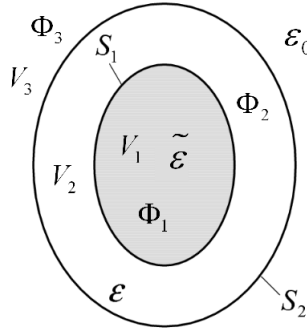


Figure 3.1: Schematic of ellipsoidal shell.

Let us first consider an ellipsoidal shell. We choose the set (a_1, b_1, c_1) to create our normal ellipsoidal coordinates. The inner ellipsoid and outer ellipsoid are

described by the following equations:

$$\frac{x^2}{a_1^2} + \frac{y^2}{b_1^2} + \frac{z^2}{c_1^2} = 1 \quad , \quad \frac{x^2}{a_2^2} + \frac{y^2}{b_2^2} + \frac{z^2}{c_2^2} = 1. \quad (3.13)$$

The semidiameters of the inner ellipsoid are denoted by subscript 1, while those of the outer ellipsoid are denoted by subscript 2. The relations between the semidiameters of the inner ellipsoid and outer ellipsoid are as follows:

$$a_2^2 - a_1^2 = b_2^2 - b_1^2 = c_2^2 - c_1^2 = \delta^2. \quad (3.14)$$

In this case, the shells with so-called ‘‘self-similar boundaries’’ (*i.e.* $\frac{a_1}{a_2} = \frac{b_1}{b_2} = \frac{c_1}{c_2}$) do not exist in the ellipsoidal coordinate system with chosen parameters a_1 , b_1 , and c_1 . Because the plasmon resonances appear at specific negative values of the dielectric permittivity for which source-free electrostatic fields may exist, they can be formulated as the following boundary value problem: find such values of ε for which nonzero solutions of differential equations

$$\nabla^2 \Phi_i = 0 \quad \text{in} \quad V_i \quad (i = 1, 2, 3) \quad (3.15)$$

exist subject to the boundary conditions

$$\tilde{\varepsilon} \frac{\partial \Phi_1}{\partial \xi} = \varepsilon \frac{\partial \Phi_2}{\partial \xi}, \quad \Phi_1 = \Phi_2 \quad \text{on} \quad S1 \quad (3.16)$$

$$\varepsilon \frac{\partial \Phi_2}{\partial \xi} = \varepsilon_0 \frac{\partial \Phi_3}{\partial \xi}, \quad \Phi_2 = \Phi_3 \quad \text{on} \quad S2 \quad (3.17)$$

$$\Phi_3(\infty) = 0, \quad (3.18)$$

where $\tilde{\varepsilon}$ and ε are dielectric permittivities for the core and metallic nanoshell, respectively. Then, the solution to the above boundary value problem can be represented

in terms of the ellipsoidal harmonics [62][67][68]

$$\Phi_1 = A_{nm}E_n^m(\xi)E_n^m(\eta)E_n^m(\zeta) \quad (3.19)$$

$$\Phi_2 = [B_{nm}E_n^m(\xi) + C_{np}F_n^m(\xi)]E_n^m(\eta)E_n^m(\zeta) \quad (3.20)$$

$$\Phi_3 = D_{nm}F_n^m(\xi)E_n^m(\eta)E_n^m(\zeta), \quad (3.21)$$

where A_{nm} , B_{nm} , C_{nm} , and D_{nm} are unknown coefficients of the degree n and order m . By substituting (3.19)-(3.21) into boundary conditions (3.16) and (3.17), we obtain four linear homogeneous equations with four unknown coefficients. The plasmon resonances occur when the nonzero solution to these equations exists, which requires the determinant of these homogeneous equations to be equal to zero. In this way, the following quadratic equation for ε_{nm} can be derived:

$$\begin{aligned} & \varepsilon_{np}^2 [E_n^m(a_1)\dot{E}_n^m(a_2)F_n^m(a_2)\dot{F}_n^m(a_1) - E_n^m(a_1)\dot{E}_n^m(a_1)F_n^m(a_2)\dot{F}_n^m(a_2)] \\ & + \varepsilon_{np}\varepsilon_0 [E_n^m(a_1)\dot{E}_n^m(a_1)F_n^m(a_2)\dot{F}_n^m(a_2) - E_n^m(a_1)E_n^m(a_2)\dot{F}_n^m(a_1)\dot{F}_n^m(a_2)] \\ & + \varepsilon_{np}\tilde{\varepsilon} [E_n^m(a_1)\dot{E}_n^m(a_1)F_n^m(a_2)\dot{F}_n^m(a_2) - \dot{E}_n^m(a_1)\dot{E}_n^m(a_2)F_n^m(a_1)F_n^m(a_2)] \\ & + \varepsilon_0\tilde{\varepsilon} [\dot{E}_n^m(a_1)E_n^m(a_2)F_n^m(a_1)\dot{F}_n^m(a_2) - E_n^m(a_1)\dot{E}_n^m(a_1)F_n^m(a_2)\dot{F}_n^m(a_2)] = 0, \end{aligned} \quad (3.22)$$

where \dot{E}_n^m and \dot{F}_n^m signify first-order differentiations of E_n^m and F_n^m with respect to the argument ξ .

3.3.1 Dipolar Plasmon Modes in an Ellipsoidal Nanoshell

We shall write this quadratic equation for a particular (but important) case of dipolar plasmon modes ($n=1$). It can be shown that only dipolar modes are efficiently excited by incident laser radiation. Again, we look for the solutions to

boundary value problems (3.15)-(3.18) in the form of

$$\begin{aligned}
\Phi_1 &= C_1 E_1^m(\xi) E_1^m(\eta) E_1^m(\zeta), \\
\Phi_2 &= [C_2 E_1^m(\xi) + C_3 F_1^m(\xi)] E_1^m(\eta) E_1^m(\zeta), \\
\Phi_3 &= C_4 F_1^m(\xi) E_1^m(\eta) E_1^m(\zeta).
\end{aligned} \tag{3.23}$$

Then, by substituting (3.23) into boundary conditions (3.16) and (3.17), we obtain four linear homogeneous equations with four unknown coefficients: C_1 , C_2 , C_3 , and C_4 . These linear equations have nonzero solutions only if the determinant of the matrix of these equations is equal to zero. This will give us the solutions in the same form as (3.22) but with $n=1$. After some manipulations and variable substitutions, (3.22) can be rewritten and the quadratic equation for specific values ε_m for which dipolar plasmon modes exist has the form

$$\begin{aligned}
&\varepsilon_m^2 [N_m^{(2)}(1 - f - N_m^{(1)} + fN_m^{(2)})] + \varepsilon_m \varepsilon_0 [(1 - N_m^{(2)})(1 - N_m^{(1)} + fN_m^{(2)})] + \\
&\varepsilon_m \tilde{\varepsilon} [N_m^{(2)}(f + N_m^{(1)} - fN_m^{(2)})] + \tilde{\varepsilon} \varepsilon_0 [(1 - N_m^{(2)})(N_m^{(1)} - fN_m^{(2)})] = 0, \quad (m = 1, 2, 3).
\end{aligned} \tag{3.24}$$

Here, f is the so-called shell ratio. $N_m^{(1)}$ and $N_m^{(2)}$ are the depolarization factors of the ellipsoids, $\xi = a_1$ and $\xi = a_2$, respectively ([63][64]). It can be shown that in the special case of a solid ellipsoid ($a_1 = 0$, $b_1 = 0$, $c_1 = 0$, and $\tilde{\varepsilon} = 0$), (3.24) can be simplified and one can obtain ε_m in the same form as which has been derived in [65] for the solid ellipsoidal nanoparticle. For thin ellipsoidal shells we find that

$$f \approx 1, \quad N_m^{(2)} \approx N_m^{(1)} = N_m, \quad (m = 1, 2, 3), \tag{3.25}$$

and from the quadratic equation (3.24) we derive

$$\varepsilon_m^- \approx -\frac{(1-N_m)\varepsilon_0 + \tilde{\varepsilon}N_m}{(1-f)(1-N_m)N_m}, \quad (m=1,2,3), \quad (3.26)$$

$$\varepsilon_m^+ \approx -\frac{\tilde{\varepsilon}\varepsilon_0(1-f)(1-N_m)N_m}{(1-N_m)\varepsilon_0 + \tilde{\varepsilon}N_m}, \quad (m=1,2,3). \quad (3.27)$$

Quadratic equation (3.24) has two solutions given by formulas (3.26) and (3.27), respectively. This is actually true for any n and this implies that there are two distinct resonance bands for ellipsoidal nanoshells. Having found ε_m^- and ε_m^+ , the corresponding resonance frequencies ω_m^- and ω_m^+ are determined by using the dispersion relation

$$\varepsilon'(\omega_m^-) = \varepsilon_m^-, \quad \varepsilon'(\omega_m^+) = \varepsilon_m^+, \quad (m=1,2,3), \quad (3.28)$$

where ε' is the real part of the nanoshell permittivity. In the particular case of a spheroidal nanoshell ($b_1 = c_1$ and $b_2 = c_2$), we find

$$N_1 = \frac{1-e^2}{2e^3} \left[\ln \frac{1+e}{1-e} - 2e \right], \quad (3.29)$$

$$N_2 = N_3 = \frac{1-N_1}{2}, \quad (3.30)$$

where $e^2 = 1 - b_1^2/a_1^2$. It is clear from formulas (3.26), (3.27), (3.30), and (3.28) that

$$\varepsilon_2^\pm = \varepsilon_3^\pm \quad \text{and} \quad \omega_2^\pm = \omega_3^\pm. \quad (3.31)$$

This means that two plasmon modes can be simultaneously excited at frequencies ω_2^- (or ω_2^+). Due to the rotational symmetry of spheroidal nanoshells it is apparent that these plasmon modes are identical and shifted in space by ninety degrees. Thus, when simultaneously excited by circularly polarized incident light, they form a circularly polarized plasmon mode. It is also clear from formulas (3.26)-(3.30) that the

resonance frequencies of a dipole plasmon mode can be effectively controlled by shell thickness and shell aspect ratio b_1/a_1 . Figures 3.2 and 3.3 present the dependence of permittivities of dipolar plasmon modes on thickness and aspect ratio, respectively. Figure 3.2 shows monotonic increase when decreasing the thickness of the nanoshell, which is consistent with the work in [66].

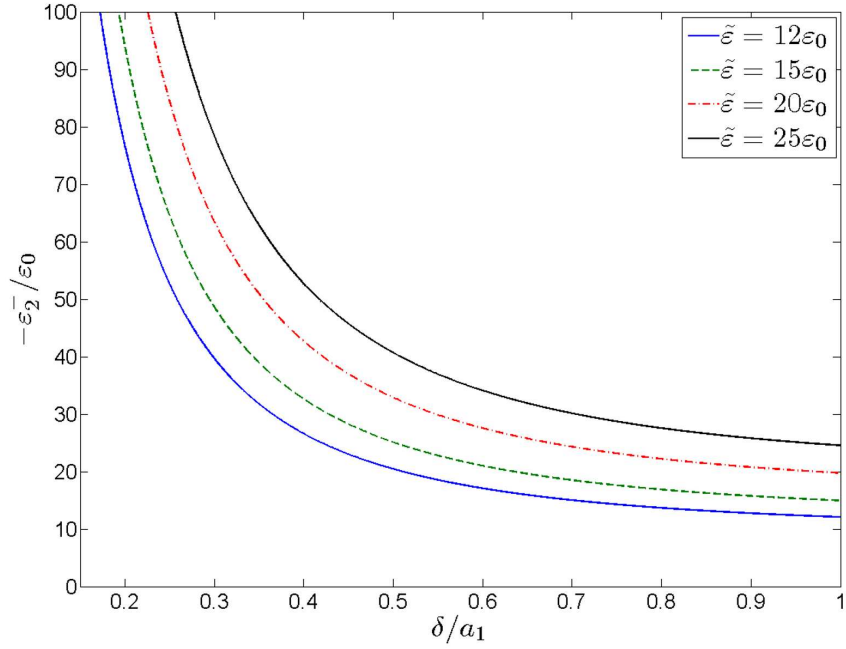


Figure 3.2: Plasmon resonance permittivity ε_2^- vs. shell thickness for various dielectric core permittivities $\tilde{\varepsilon}$.

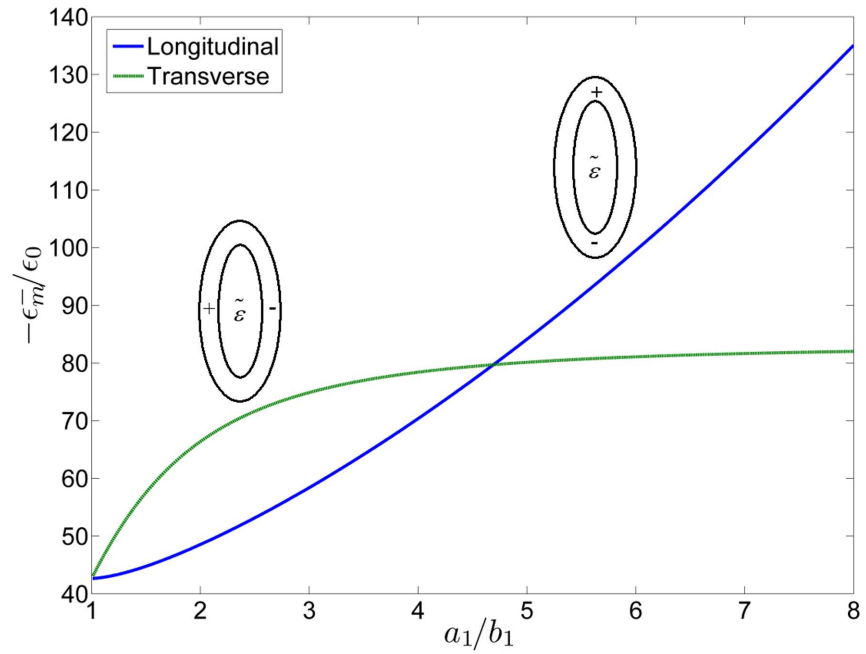


Figure 3.3: Plasmon resonance permittivities of longitudinal dipolar plasmon mode and transverse dipolar plasmon mode vs. aspect ratio for silicon core $\tilde{\varepsilon} = 11.7\varepsilon_0$ and fixed thickness δ/b_1 .

3.3.2 Excitation of the Dipolar Plasmon Modes in an Ellipsoidal Shell

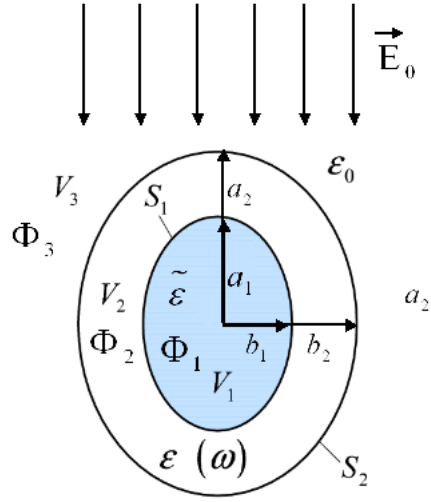


Figure 3.4: Schematic of ellipsoidal shell.

In this section, we present how the dipolar plasmon modes in an ellipsoidal shell are excited and the expressions of electric potential as well as electric field outside the ellipsoidal shell. Conceptually, these calculations are very similar to those performed in [61] for spherical nanoshells. The main difference is that ellipsoidal rather than spherical coordinates are used in the derivations, which makes these derivations more complicated. Let us consider a spatially uniform and time-varying electric field $\mathbf{E}_0(t) = E_0 f(t) \mathbf{e}_i$, where \mathbf{e}_i is a unit vector along one of the three principal axes of the ellipsoidal shell. Each \mathbf{e}_i excites one specific dipole mode, labeled order p . First, we consider the incident field is along the x -direction, which is $\mathbf{E}_0(t) = E_{0x} f(t) \mathbf{e}_x$. In this case, its potential is $\Phi_0(t) = -E_{0x} x f(t)$. Since the medium of the shell is dispersive and exhibits nonlocal-in-time constitutive relation, the frequency domain technique is then employed. Then, the excited electric field

will satisfy (3.15) and the following boundary conditions:

$$\tilde{\varepsilon} \frac{\partial \Phi_1^x}{\partial \xi} - \varepsilon(\omega) \frac{\partial \Phi_2^x}{\partial \xi} = [\tilde{\varepsilon} - \varepsilon(\omega)] \frac{E_{0x}}{hk} \tilde{f}(\omega) \frac{\partial E_1^x(\xi)}{\partial \xi} E_1^x(\eta) E_1^x(\zeta) \quad (3.32)$$

$$\Phi_1^x = \Phi_2^x \quad \text{on} \quad S_1 \quad (3.33)$$

$$\varepsilon(\omega) \frac{\partial \Phi_2^x}{\partial \xi} - \varepsilon_0 \frac{\partial \Phi_3^x}{\partial \xi} = [\varepsilon(\omega) - \varepsilon_0] \frac{E_{0x}}{hk} \tilde{f}(\omega) \frac{\partial E_1^x(\xi)}{\partial \xi} E_1^x(\eta) E_1^x(\zeta) \quad (3.34)$$

$$\Phi_2^x = \Phi_3^x \quad \text{on} \quad S_2, \quad (3.35)$$

where Φ_1^x , Φ_2^x , and Φ_3^x represent the potentials created by the plasmon mode excited by x -direction uniform incident field. $\tilde{f}(\omega)$ is the Fourier transform of $f(t)$. By substituting (3.23) into boundary conditions (3.33) and (3.35), we obtain the inhomogeneous linear equations for C_1 , C_2 , C_3 , and C_4 . The determinant of the matrix of these simultaneous equations is $\Delta[\varepsilon(\omega)]$. Then we are interested in finding the exterior electric field of the ellipsoidal nanoshell. In order to derive the formula for this electric field, we need to find out the coefficient C_4 by using Cramer's rule. For a very thin spheroidal shell, C_4 can be approximated by using Taylor series. In the case of very high permittivity core ($\tilde{\varepsilon} \gg \varepsilon_0$), the exterior electric potential can be expressed as

$$\Phi_3^x(\omega, \xi, \eta, \zeta) = v \frac{E_{0x}}{hk} \tilde{f}(\omega) \tilde{g}_{1x}(\omega) F_1^x(\xi) E_1^x(\eta) E_1^x(\zeta), \quad (3.36)$$

where

$$v = \frac{a_2 b_2 c_2}{3}, \quad \tilde{g}_{1x}(\omega) = \frac{\varepsilon(\omega)}{N_1^{(x)} [\varepsilon(\omega) - \varepsilon_{1x}]}, \quad (3.37)$$

$\varepsilon_{1x} = \varepsilon'(\omega_{1x})$, and $\varepsilon'(\omega_{1x})$ is the real part of the dispersion relation $\varepsilon(\omega_{1x})$ for the dipole mode along the x -direction.

3.3.2.1 On-resonance excitation

Consider that the incident radiation is on resonance frequency, that is,

$$f(t) = \sin \omega_{1x} t, \quad \tilde{f}(\omega) = i\sqrt{\frac{\pi}{2}}[\delta(\omega - \omega_{1x}) - \delta(\omega + \omega_{1x})]. \quad (3.38)$$

In this case, we can find the time-domain expression of Φ_3^x by taking the inverse Fourier transform of the frequency component in (3.36), which is $\tilde{g}_{1x}(\omega)\tilde{f}(\omega)$. Consequently, we obtain the time-domain exterior electric potential

$$\Phi_3^x(t, \xi, \eta, \zeta) = v \frac{E_{0x}}{hk} \frac{1}{N_1^{(x)}} \left(\frac{\varepsilon'(\omega_{1x})}{\varepsilon''(\omega_{1x})} \cos \omega_{1x} t + \sin \omega_{1x} t \right) F_1^x(\xi) E_1^x(\eta) E_1^x(\zeta). \quad (3.39)$$

Finally, the exterior electric field can be obtained by using $\mathbf{E}_3^x(t, \xi, \eta, \zeta) = -\nabla \Phi_3^x$.

3.3.2.2 Off-resonance excitation

Now consider the off-resonance excitation case, that is

$$f(t) = \sin \omega_0 t, \quad \tilde{f}(\omega) = i\sqrt{\frac{\pi}{2}}[\delta(\omega - \omega_0) - \delta(\omega + \omega_0)]. \quad (3.40)$$

Again, we take the inverse Fourier transform of the frequency component in (3.36), and the exterior electric potential will be

$$\Phi_3^x(t, \xi, \eta, \zeta) = v \frac{E_{0x}}{hk} \frac{1}{N_1^{(x)}} C_{1x}(\omega_0) \cos(\omega_0 t + \phi_{1x}) F_1^x(\xi) E_1^x(\eta) E_1^x(\zeta), \quad (3.41)$$

where

$$C_{1x}(\omega_0) = \arctan \left(-\frac{\varepsilon'(\omega_0)^2 + \varepsilon''(\omega_0)^2 - \varepsilon'(\omega_{1x})\varepsilon'(\omega_0)}{\varepsilon'(\omega_{1x})\varepsilon''(\omega_0)} \right). \quad (3.42)$$

Since the circularly polarized incident field is a superposition of two linearly polarized fields, by using the results obtained for linear polarization, we can readily

translate them into results for the circular polarization by using the superposition of two linearly polarized plasmon modes shifted in space and time by 90° .

3.4 Results and Discussion

Figure 3.5 presents the comparison of the light intensity of optical spots produced by circularly polarized dipole plasmon modes in spherical and spheroidal nanoshells at a distance of 5 nm from the nanoshells. The calculations have been performed for the following values of parameters: $a_2/b_2 = 3$, $b_2 = 15$ nm, and $b_1/b_2 = 3/4$, $r_2 = 15$ nm, and $r_1/r_2 = 3/4$. The parameters of the spherical and spheroidal nanoshells were chosen to have the same transverse dimension and shell thickness in order to reveal their nano-focusing and light enhancement under comparable conditions. The specific transverse nanoshell dimensions (of 15 nm) were chosen in our calculations to demonstrate that transverse dimensions (FWHM) of focused light spots below 10 nm can be achieved (see Figure 3.6). Such small light spots may be necessary for the development of future high-data-density storage devices. It is apparent from the presented computational results that spheroidal nanoshells are superior to the spherical nanoshell as far as the enhancement of circularly polarized light intensity and its nanoscale focusing are concerned. This suggests that plasmon resonances in spheroidal nanoshells can be attractive for the implementation of all-optical recording in future magnetic data storage systems.

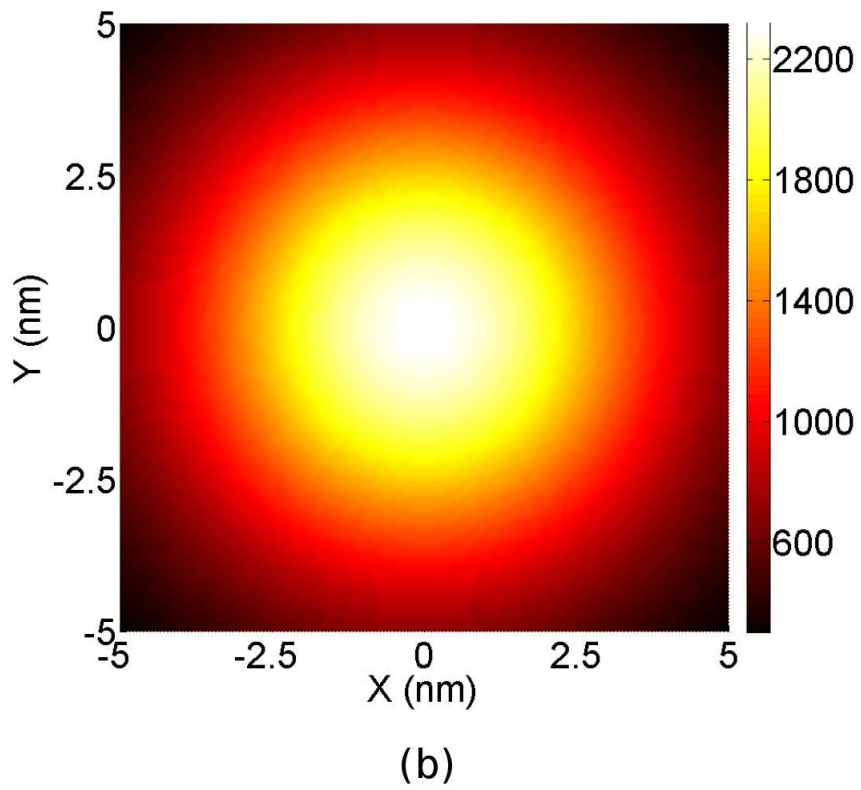
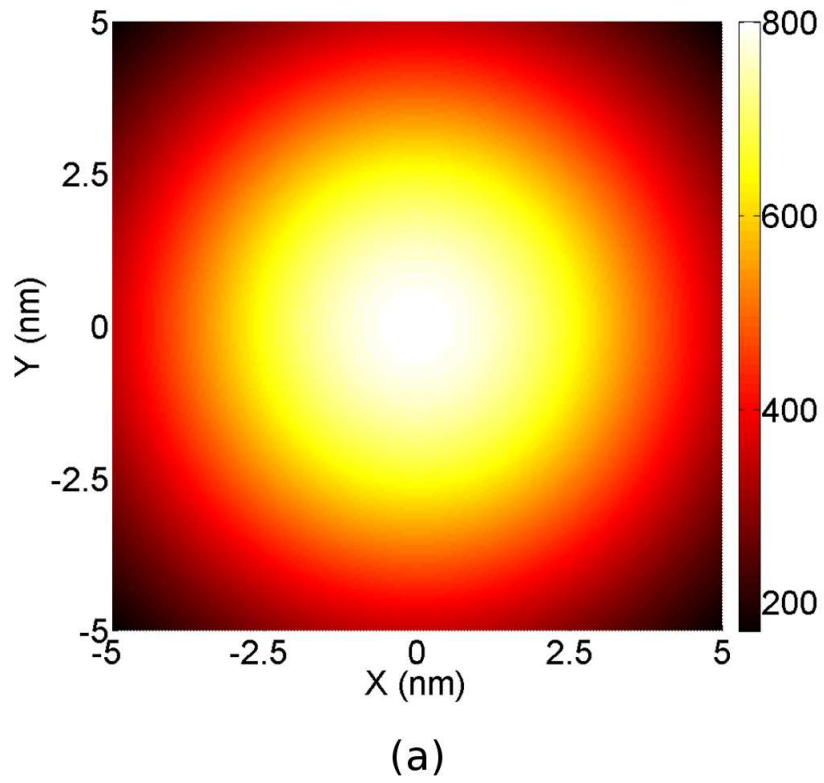


Figure 3.5: Light intensity of optical spots produced by the circularly polarized dipolar plasmon modes in (a) spherical, and (b) spheroidal nanoshells.

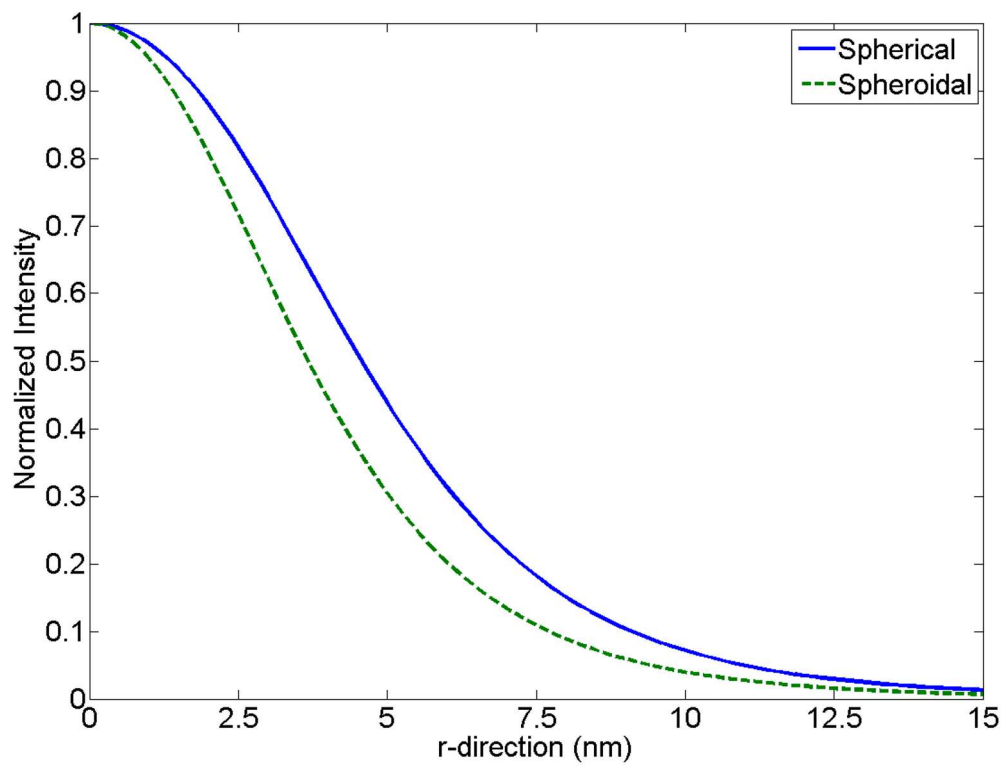


Figure 3.6: Radial variations of normalized light intensities generated by circularly polarized dipolar plasmon modes in spherical and spheroidal nanoshells.

Chapter 4

Application of Plasmon Resonances to Heat-Assisted Magnetic Recording (HAMR)

4.1 Overview

Magnetic storage and magnetic recording have been widely used to store information. They use different patterns of magnetization in a magnetic material to record data and its recorded data is non-volatile. Nowadays, massive data and information are stored in the currently primary magnetic storage media, the hard disk, which is a rigid rapidly rotating platter. This platter (or disc) is divided into many small magnetic regions which have mostly uniform magnetizations. Based on different recording technologies, the direction of these magnetizations can be in-plane or out-of-plane. Currently, two magnetic recording methods are used in hard-drive disk industry. One is longitudinal recording, and the other is perpendicular recording. Compared with perpendicular recording, longitudinal recording is relatively old technology which utilizes the fringing magnetic field to magnetize the magnetic regions such that their magnetization directions are parallel to the disk surface. For the past few years, the orientation of magnetizations was changed to perpendicular to the disk surface, and consequently allows the disks to have higher magnetic recording density. However, the increase of storage density in hard disk drives is still

in demand. Therefore, more and more technologies have been studied and developed to achieve this goal, and some bottlenecks need to be overcome. On the recording material side, as the storage density continues to increase, magnetic grains of the recording layer become superparamagnetic and their magnetic state thermally unstable [69]. This causes the reliability issue of the recording data in the hard disk drives. To tackle this issue, one can use high magnetic anisotropy (k_u) materials as a recording layer to maintain the thermal stability of magnetic domains. Materials like $L1_0$ FePt can support grains of about 2 to 3 nm in diameter [70], and storage densities are up to 155 Pb/m² [71]. However, this means that it will require a magnetic field beyond what can be supplied by a traditional hard disk recording head to switch the magnetizations in the high magnetic anisotropy materials. The solution is to heat the recording media temporarily and locally to reduce its coercivity during the writing process. This is so-called heat-assisted magnetic recording (HAMR), which is currently a focus of considerable research and technological interest in high density magnetic data storage ([72]-[77]). In HAMR, the recording layer is optically heated to reduce the coercivity of the media by using a powerful localized light source. This reveals that one of the main issues of high-density HAMR is to develop the optical sources with nanometer resolution and high intensity. Storage density on the order of 1 Tb/in.² requires an optical spot of about 25 nm×25 nm [78]. Optical energy must be delivered and confined to a spot much smaller than the diffraction limit to avoid collateral heating of adjacent recorded bits. It has been realized that plasmon resonances in metallic nanostructures hold unique promise for the development of such optical sources provided these nanostructures are properly designed.

A variety of metallic nanostructures for generating high light intensity optical spots at the nanoscale have been recently proposed and studied ([79]-[83]). In the designs of recording heads for HAMR, the metallic nanostructures are surrounded by many parts. These parts include dielectric substrates, lubricants, recording layers and heat sink layers (see Figure 4.1), which may affect the plasmon resonances of metallic nanostructures. Consequently, these surrounding parts have to be considered when designing the simulation model in order to predict the resonance frequencies of a metallic nanostructure accurately. Sendur *et al.* have discussed the effect of the recording medium in [84]. In this work, we develop a computational methodology to take into account the effects of two other parts in the recording head design used in HAMR. One is the finite dielectric substrate used to guide the incident light to the metallic nanostructures. The other is the heat sink layer, which is made of plasmonic material to cool down the magnetic recording media during the writing process. The resonance frequencies (wavelengths) of such metallic nanostructures as well as the corresponding plasmon modes can be computed by solving a constrained eigenvalue problem. Finally, the light intensities in free space locations of interest can be evaluated by using the computed surface electric charges on the boundaries of metallic nanoparticles and neighboring dielectric objects.

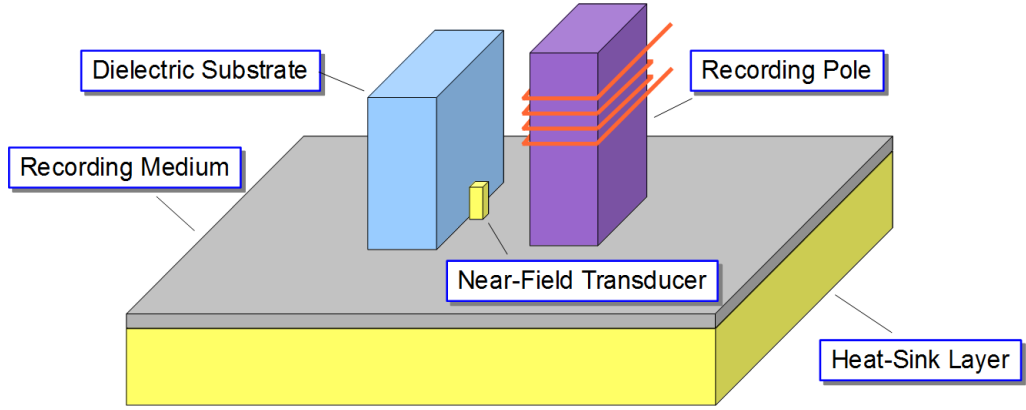


Figure 4.1: Schematic illustration of recording head design in HAMR.

4.2 Constrained Eigenvalue Problem

As presented in sec. 1.3, the resonance values of dielectric permittivity and corresponding resonant plasmon modes for a single particle (or an ensemble of particles) can be computed by solving a homogeneous boundary integral equation. By using the appropriate Green function found by the method of images, this integral equation can be used for the case of nanoparticles placed on dielectric substrates. However, the Green function in (1.72) is derived when the substrate is semi-infinite. This is not the case in the real-world design of the substrates used in the recording head of HAMR. In HAMR, metallic nanoparticles are surrounded by dielectric materials which are finite in size, and this finite substrate may affect the plasmon resonances to a different degree than the semi-infinite substrate. Therefore, the development of a technique for including the surrounding finite dielectric components is required. To start our discussion, first we consider a metallic nanoparticle with boundary S_1 and dielectric permittivity $\varepsilon(\omega)$ located in proximity to a dielectric

object with boundary S_2 and dielectric permittivity $\tilde{\epsilon}$ in free space with dielectric constant ϵ_0 (see Figure 4.2(a)).

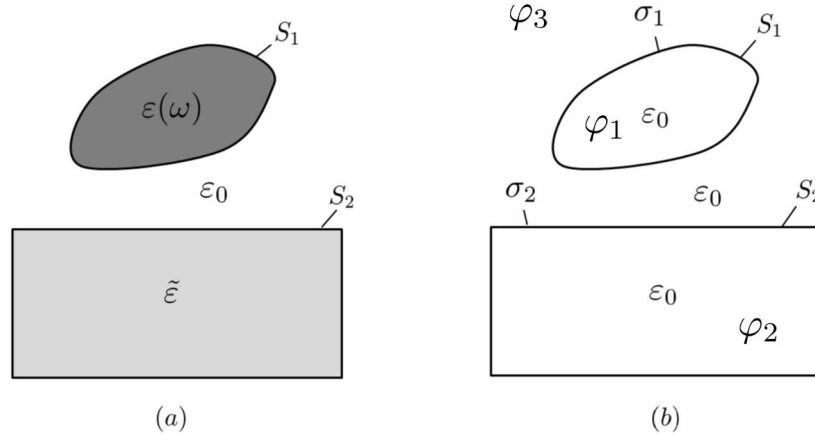


Figure 4.2: (a) The metallic nanoparticle of arbitrary shape with permittivity $\epsilon(\omega)$ located near a dielectric object of arbitrary shape with permittivity $\tilde{\epsilon}$; (b) The equivalent model with surface charges σ_1 and σ_2 distributed in free space.

It can be demonstrated that the electric potentials φ_1 , φ_2 , and φ_3 can be represented as being generated by a single layer of electric charges σ_1 and σ_2 distributed over the boundaries S_1 and S_2 , respectively (see Figure 4.2b) Therefore, the electric potential in free space can be expressed as the follows:

$$\varphi(Q) = \frac{1}{4\pi\epsilon_0} \left[\oint_{S_1} \frac{\sigma_1(M)}{r_{MQ}} dS_M + \oint_{S_2} \frac{\sigma_2(M)}{r_{MQ}} dS_M \right]. \quad (4.1)$$

Then the resulting electric field in free space is the source-free electric field that may exist under the conditions that particle permittivity is negative and the wavelength is large in comparison with particle dimension. Again, by satisfying the boundary conditions on S_1 and S_2 , and by using the same line of reasoning mentioned in sec.

1.3, the following coupled homogeneous boundary integral equations can be derived:

$$\sigma_1(Q_1) = \frac{\lambda}{2\pi} \left[\oint_{S_1} \sigma_1(M) \frac{\mathbf{r}_{MQ_1} \cdot \mathbf{n}_{Q_1}}{r_{MQ_1}^3} dS_M + \oint_{S_2} \sigma_2(M) \frac{\mathbf{r}_{MQ_1} \cdot \mathbf{n}_{Q_1}}{r_{MQ_1}^3} dS_M \right], \quad (4.2)$$

$$\sigma_2(Q_2) = \frac{\tilde{\lambda}}{2\pi} \left[\oint_{S_1} \sigma_1(M) \frac{\mathbf{r}_{MQ_2} \cdot \mathbf{n}_{Q_2}}{r_{MQ_2}^3} dS_M + \oint_{S_2} \sigma_2(M) \frac{\mathbf{r}_{MQ_2} \cdot \mathbf{n}_{Q_2}}{r_{MQ_2}^3} dS_M \right], \quad (4.3)$$

where

$$\lambda = \frac{\varepsilon(\omega) - \varepsilon_0}{\varepsilon(\omega) + \varepsilon_0}, \quad \tilde{\lambda} = \frac{\tilde{\varepsilon} - \varepsilon_0}{\tilde{\varepsilon} + \varepsilon_0}, \quad Q_1 \in S_1, \quad Q_2 \in S_2. \quad (4.4)$$

To realize the software implementation of (4.2) and (4.3), we discretize the integral operators in the above integral equations and obtain the following equations:

$$\vec{X}_1 = \lambda \left[\hat{K}_{11} \vec{X}_1 + \hat{K}_{12} \vec{X}_2 \right], \quad (4.5)$$

$$\vec{X}_2 = \hat{K}_{21} \vec{X}_1 + \hat{K}_{22} \vec{X}_2, \quad (4.6)$$

where matrices \hat{K}_{ij} are discretized versions of the corresponding integral operators in (4.2) and (4.3), and \vec{X}_1 and \vec{X}_2 are the discretized versions of $\sigma_1(Q_1)$ and $\sigma_2(Q_2)$, respectively. After substituting (4.6) into (4.5), we obtain the following eigenvalue problem for λ :

$$\vec{X}_1 = \lambda \left[\hat{K}_{11} + \hat{K}_{12} (\hat{I} - \hat{K}_{22})^{-1} \hat{K}_{21} \right] \vec{X}_1, \quad (4.7)$$

where \hat{I} is the identity matrix. After λ are computed, the resonance frequencies for the metallic nanoparticle can be determined by using formula (4.4) and appropriate dispersion relation

$$\varepsilon_k = \varepsilon'(\omega_k) = \text{Re}[\varepsilon(\omega_k)], \quad (4.8)$$

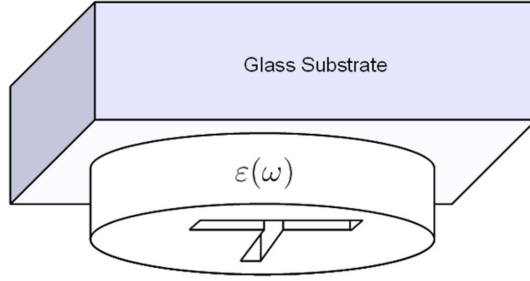
where ω_k is the resonance frequency corresponding to the k th plasmon mode. Once we obtain \vec{X}_1 , the discretized version of $\sigma_2(Q_2)$ can be computed by using the

following relation:

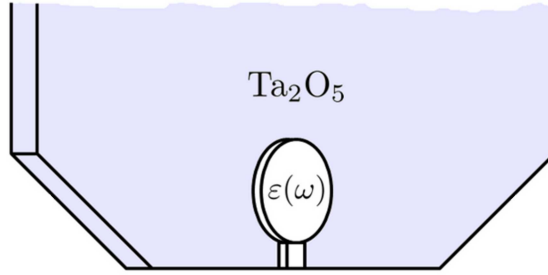
$$\vec{X}_2 = (\hat{I} - \hat{K}_{22})^{-1} \hat{K}_{21} \vec{X}_1. \quad (4.9)$$

4.3 Results Discussion

The numerical technique based on discretization ((4.7) and (4.9)) has been software implemented. To illustrate this method, we perform the calculations for two examples of metallic nanostructures. One is a T-shaped gold aperture, and the other is a lollipop gold nanodisk. These metallic nanostructures are of interest for HAMR development. In the case of the T-shaped aperture, the dielectric substrate, to which the T-shaped aperture is attached (see Figure 4.3a), accounts for the tapered fiber or solid immersion lens which guides the incident light to the T-aperture nanofilm. The lollipop nanodisk was proposed by Challener *et al.* [76], in which a planar waveguide is used to deliver the laser light to the lollipop nanodisk (see Figure 4.3b).



(a)



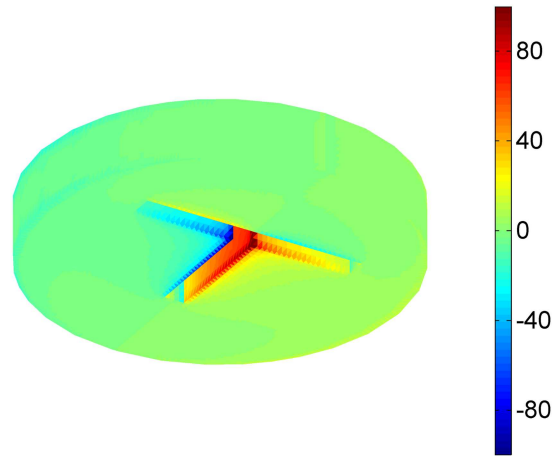
(b)

Figure 4.3: (a) Metallic nanofilm with T-shaped aperture attached on glass substrate ($\tilde{\epsilon} = 2.25\epsilon_0$); (b) Lollipop metallic nanodisk placed next to Ta_2O_5 substrate ($\tilde{\epsilon} = 4.6\epsilon_0$)

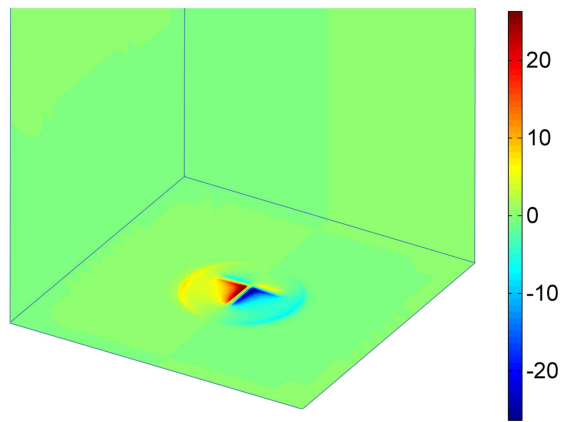
4.3.1 T-shaped Apertures

First, we perform the calculations of plasmon modes in T-aperture nanofilms. The geometry parameters for the T-aperture nanofilms have been chosen in such a way to locate its resonance frequency (dipolar mode) at the favorable frequency regions for gold and silver. After testing different choices of these parameters, the length of the horizontal leg is chosen to be 110 nm, the length of the vertical leg 60 nm, and the widths of both legs 10 nm, whereas the thickness and the diameter

of the T-aperture nanofilm is chosen to be 30 nm and 180 nm, respectively. After solving the eigenvalue problem in (4.7), we identify the dipolar plasmon mode in the T-aperture nanofilms. Figure 4.4a shows the computed surface charge distribution of the dipole plasmon mode in T-shaped apertures, and Figure 4.4b presents the computed surface charges distributed on the glass substrate by using discretized equation (4.9). The positive and negative charges are represented by red and blue colors, respectively. The resonance value of dielectric permittivity for this mode in such structure is $\varepsilon = -34.61\varepsilon_0$, which corresponds to the resonance wavelengths of 920 nm and 839 nm for gold and silver, respectively [113]. The corresponding ratios of $\varepsilon'(\omega)$ to $\varepsilon''(\omega)$ are equal to 14.84 and 78.34 for gold and silver T-aperture nanofilms, respectively.



(a)



(b)

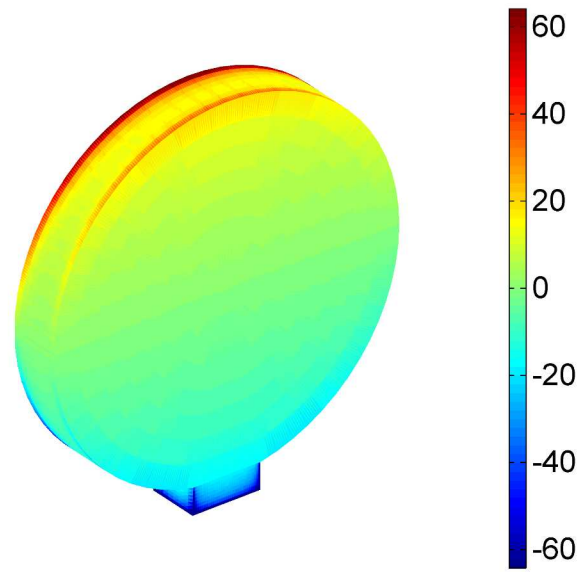
Figure 4.4: (a) Plasmon mode for T-shaped aperture; (b) Surface charges distributed on glass substrate.

4.3.2 Lollipop Nanodisks

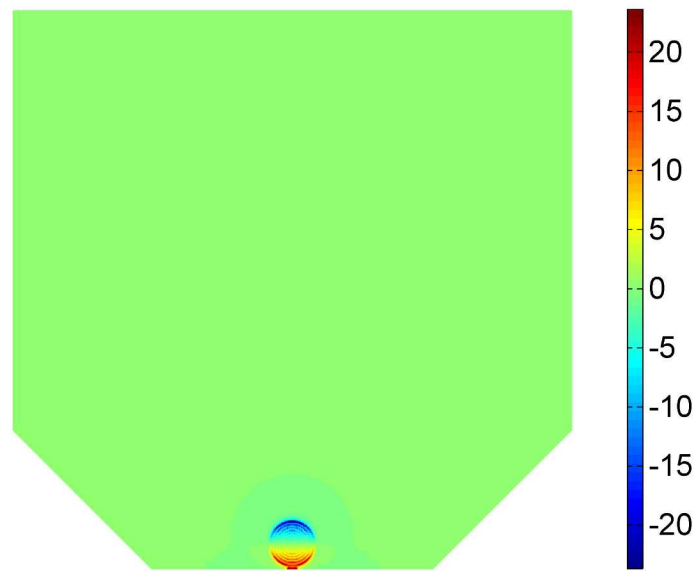
Next, we perform the same analysis for lollipop nanodisks. In this calculation, the diameter of the lollipop nanodisk is chosen to be 200 nm, whereas the thickness of the lollipop nanodisk is set to be 30 nm. The length and the width of

the peg are designed to be 15 nm and 40 nm, respectively. Figure 4.5 shows the charge distribution of the dipole plasmon mode in the lollipop nanodisk and its image charges on the Ta₂O₅ substrate. The resonance value of dielectric permittivity is $\varepsilon = -24.87\varepsilon_0$ and its dipole moment is along the lollipop axis. The resonance wavelengths of this plasmon mode are 809 nm and 723 nm for gold and silver, respectively, and their corresponding ratios of $\varepsilon'(\omega)$ to $\varepsilon''(\omega)$ are equal to 15.86 and 73.27.

In order to excite these two dipolar plasmon modes, the incident electric fields have to be collinear to the direction of their dipole moments [26]. If we assume that the incident electric fields are uniform and parallel to the dipole moments of these two dipolar plasmon modes, the steady-state charges on metallic nanoparticles and their substrates can be found and used to compute the light intensities 15nm below the bottom face of a T-aperture and 15nm below the peg of a lollipop disk (see Figure 4.6). In the case of T-aperture gold nanofilm, its optical spot has the dimension of 30 nm in x -direction and 40 nm in y -direction, while in the lollipop gold nanodisk case, it is 60 nm in x -direction and 40 nm in y -direction. These results suggest that in the absence of heat sink layers, both structures produce well-localized optical spots with high light intensity enhancements.

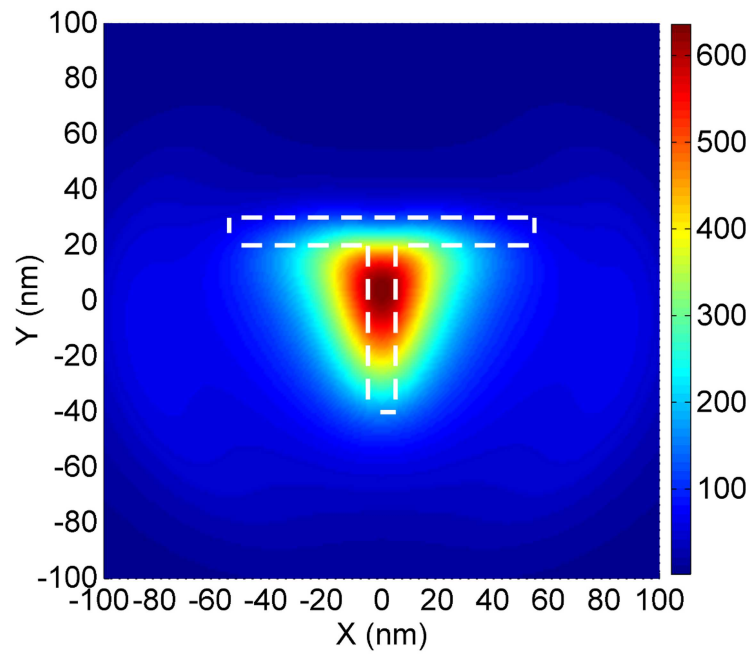


(a)

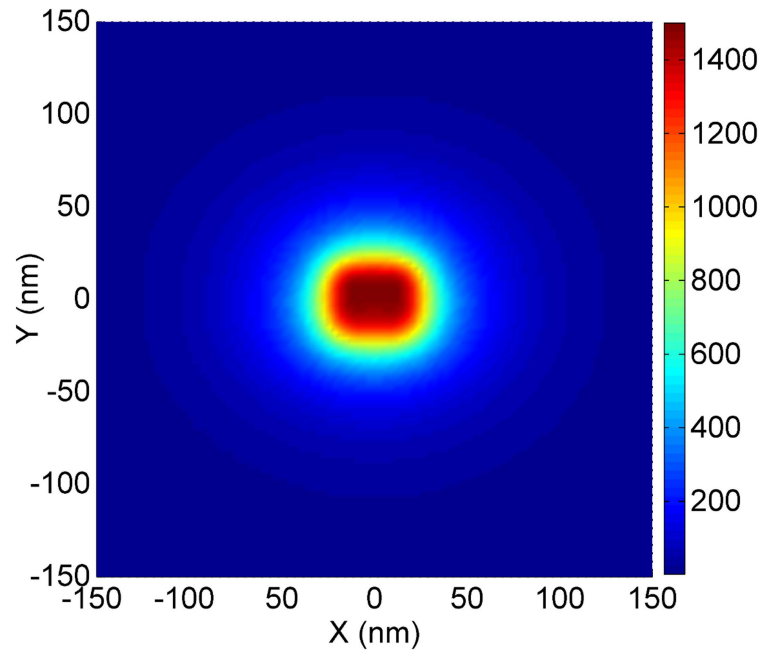


(b)

Figure 4.5: (a) Plasmon mode for lollipop metallic nanodisks; (b) Surface charges distributed on Ta_2O_5 substrate.



(a)



(b)

Figure 4.6: Light intensity enhancement generated by the plasmon mode in (a) T-shaped gold aperture and (b) lollipop gold nanodisk at the distance of 15 nm below.

4.4 Effect of Heat Sink Layers

As mentioned before, the operational principle of HAMR is to apply heat on the magnetic media to facilitate the recording process. The period of this heating has to be very short such that the media will not be overheated and burned. In order to protect the media and maintain its durability, a heat sink layer is utilized to achieve fast cooling for the recording media [85]. It turns out the noble metals such as copper and gold are good candidate for this layer since they have high thermal conductivities ([76][86]). However, these noble metals are also known as plasmonic materials, such that their presence may have some coupling with the metallic nanoparticles, and consequently, affect their plasmon resonances especially when they are brought close together. For this reason, it is important to consider the presence of heat sink layers when studying their plasmon resonances. To study the effect of the heat sink layer, we place heat sink layers 25 nm away from the bottom faces of the metallic nanoparticles (see Figure 4.7). The plasmonic plates have the dimensions of 2000 nm×2000 nm×50 nm to simulate the situation in real-world HAMR designs. In these simulations, the boundary S_1 in formula (4.2) and (4.3) is construed as the union of two boundaries.

In the case that both metallic particles and heat sink layers are gold, the resonance values of dielectric permittivities change to $\varepsilon = -37.86\varepsilon_0$ and $\varepsilon = -28.43\varepsilon_0$ for T-shaped aperture and lollipop nanodisk, respectively, which shift their resonance wavelengths to 956 nm and 850 nm. This red-shift in resonance wavelength is a result of the coupling between the near-field transducer and the heat sink layer.

It is worthwhile to point out that the above results can be applied to the case when nanoparticles are gold and heat sink layers are copper. Figure 4.8 shows the experimental data of the real parts of the dielectric permittivities of gold and copper [113], and it reveals that for the optical frequency range, copper has almost identical dispersion relation for the real part of permittivity as gold. Consequently, the differences of the computed resonance wavelengths between using gold and copper for metallic nanoparticles and heat sink layers are negligible (10 ~ 15 nm).

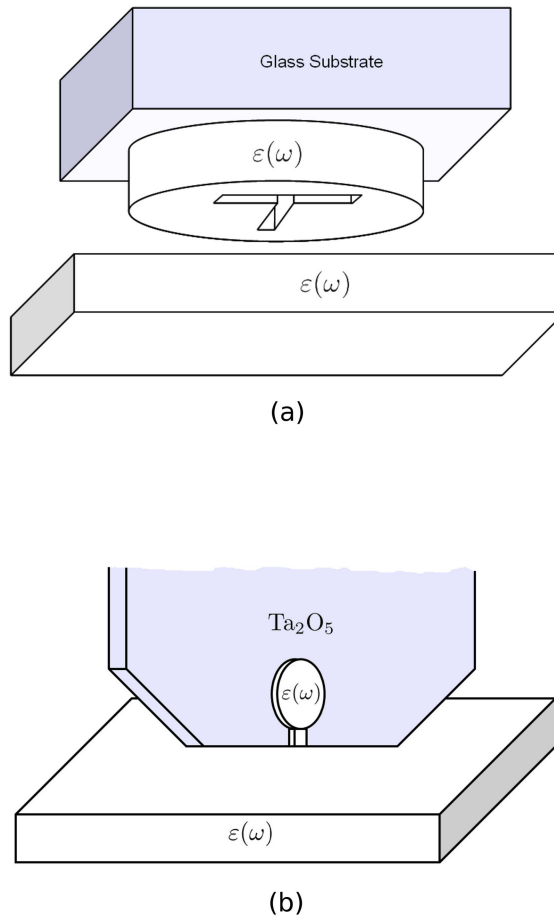


Figure 4.7: (a) T-shaped perforated metallic nanofilms with plasmonic metal as heat sink; (b) Lollipop metallic nanodisks with plasmonic metal as heat sink.

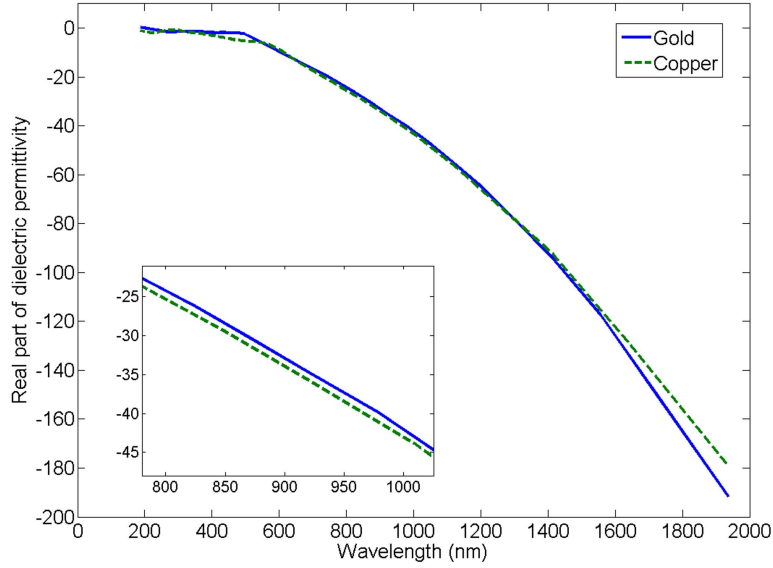


Figure 4.8: Dispersion relations of real parts of dielectric permittivities for gold and copper given by [113].

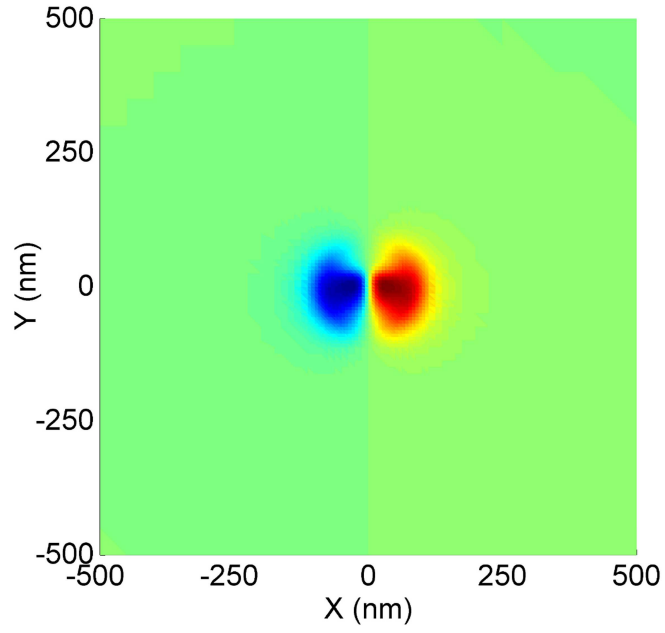
Finally, the electric fields are computed by using the surface charges distributed on transducers, dielectric substrates, and heat sink layers. Figure 4.9 shows the induced charges on heat sink layers in both cases. Notably, they have the opposite charge polarities to the charges on the near-field transducers themselves, which significantly affect the light intensities of their optical spots. For T-apertures, the surface charges on the heat sink layer produces the electric fields that further enhance the light intensities in the side regions, but diminish the light intensity in the center region (see Figure 4.10a). On the other hand, for the lollipop nanodisks, these charges on heat sink layers further increase the light intensity without changing the profile of its optical spot (see Figure 4.10b). This suggests that the presence of heat sink layers is beneficial for lollipop transducer designs but detrimental for the aperture-type near-field transducers.

Here, we would like to make the following remarks on our results. Notably, our

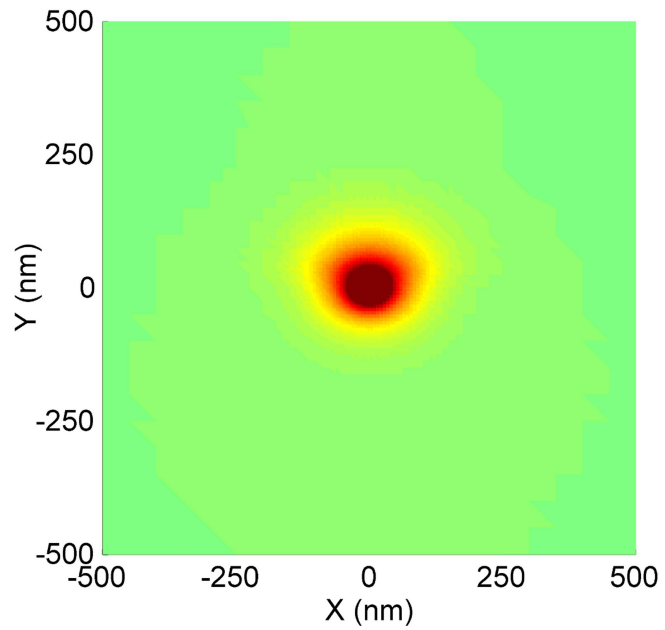
simulation model does not include the magnetic media. However, magnetic properties of recording media do not affect plasmon resonances much in nanoparticles because these resonances are electrostatic in nature. This can be demonstrated by comparing the resonance wavelength computed for lollipop nanodisks in this work and the simulation work performed by Challener *et al.* [76]. Figures 4.10a and b are computed by the steady-state electric charges as a result of excitation by uniform electric fields. However, the incident light guided to the metallic nanoparticles is not exactly uniform. Furthermore, the presence of the magnetic media also introduces the reflection of incident light to the metallic nanoparticles. Both of the non-uniformity and the reflection may affect the overall excitation conditions of the plasmon resonances in metallic nanoparticles, which would result in different strengths of steady-state electric charges, and consequently, different light intensities. Therefore, the excitation conditions of the plasmon modes in such nanostructures needs to be further studied.

4.5 Conclusions

In summary, we developed a technique to solve the plasmon resonance problems in metallic nanostructures located nearby some dielectric objects with arbitrary shapes. The plasmon resonance problem for such structures has been formulated as a constrained eigenvalue problem for specific coupled boundary integral equations. By using this technique, we compute the resonance wavelengths as well as corresponding plasmon modes for two metallic nanostructures. In the absence of



(a)

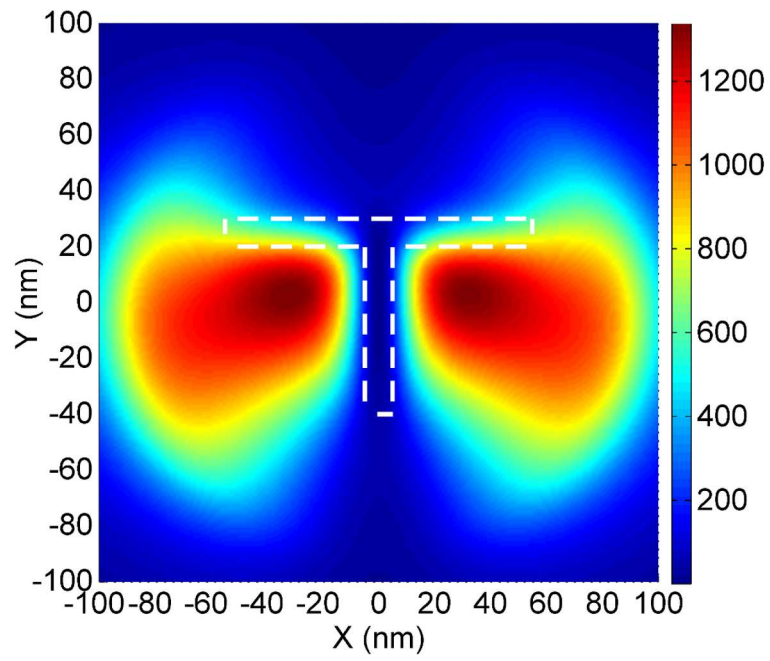


(b)

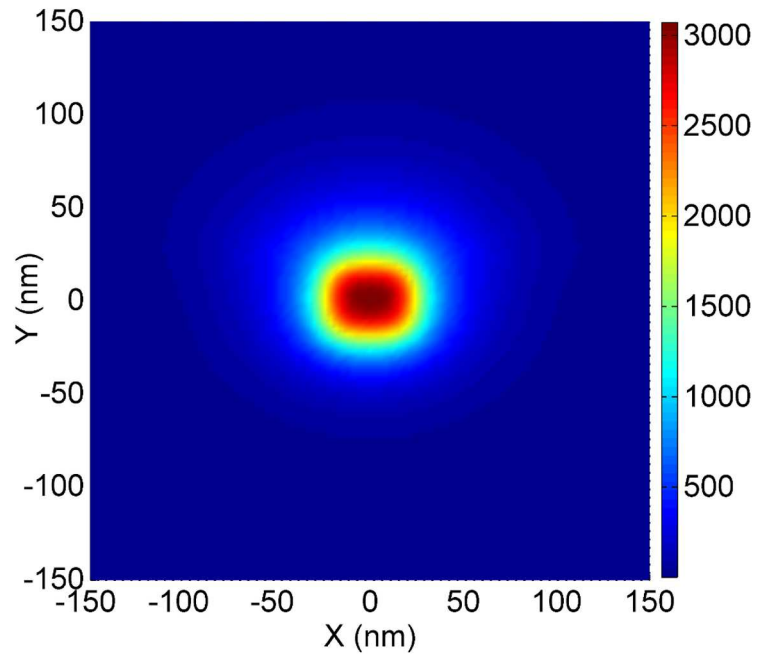
Figure 4.9: Surface charges distributed on heat sink layers for (a) T-aperture case and (b) lollipop disk case.

heat sink layers, both metallic nanostructures produce well-localized optical spots with high light intensity enhancements. When the heat sink layers are placed in the

simulation model, their resonance wavelengths are red-shifted by $\sim 4\%$ and $\sim 5\%$ for T-shaped gold apertures and lollipop gold nanodisks, respectively. In addition to the red-shift in the resonance wavelengths, the surface charges induced on heat sink layers affect light intensities of optical spots. Our computational results suggest that the metallic nanoparticles with protruding parts may be more suitable for HAMR than aperture-type nanoparticles as far as the capability of light focusing and enhancement is concerned.



(a)



(b)

Figure 4.10: Light intensity enhancement calculated at (a) 15 nm below the bottom face of T-shaped gold aperture and (b) 15 nm below the peg of lollipop gold nanodisk in the presence of gold heat sink layers.

Chapter 5

Radiation Corrections for Plasmon Resonances in Nanoparticles

5.1 Introduction

In Chap. 1, we have introduced the two conditions for plasmon resonances to occur in metallic nanoparticles: 1) the wavelengths of the incident radiation are appreciably larger than the geometric dimensions of the metallic nanoparticles and 2) the dielectric permittivity of nanoparticles is negative at these wavelengths. These resonances occur for special negative values of the nanoparticle permittivity (*i.e.*, resonance permittivities). The problem of computing these negative resonance values of the permittivity is framed as an eigenvalue problem for equation (1.67). This approach reveals that within the electrostatic approximation the resonance values of the nanoparticle permittivity (and, consequently, the resonance wavelengths) depend only on the shape of the nanoparticles but not their dimensions. When the dimensions of a nanoparticle are increased, the quasistatic condition does not strictly hold, and retardation (wave) effects manifest themselves. In this situation, the accuracy of the electrostatic approximation may be compromised and appropriate radiation corrections for the calculation of resonance permittivities are needed. The retardation effects were first found by Mie in his analytical solution of Maxwell's equations for spherical particles. By using the perturbation technique, the radiation corrections can be derived for arbitrary shape of the nanoparticles [93]. In

this chapter, we first demonstrate the accuracy of these radiation corrections by comparing some computational results with theoretical prediction and experimental data. Subsequently, we extend this method by computing multiple dipolar plasmon modes observed in nanocubes. We find that different dipolar modes have different sensitivities to the increase of size. Furthermore, we explore the sensitivities to the cube size for the primary dipolar modes (highest resonance wavelength) in sharp-corner cubes and round-corner cubes. Finally, the radiation corrections are performed for nanocube face-to-face dimers for various “gap-to-cube edge length” ratios, which could be used for the deduction of gap distances between nanoparticles from extinction cross section measurements.

5.2 Second-Order Corrections

5.2.1 Theoretical Modeling

The radiation corrections can be mathematically treated as perturbations with respect to a small parameter β , which is defined as the ratio of particle dimensions (their diameters) to the free-space wavelengths:

$$\beta = \omega \sqrt{\mu_0 \varepsilon_0} d, \quad (5.1)$$

where d is the nanoparticle diameter, *i.e.*, the maximum distance between any two points M and Q on S . According to perturbation theory, the resonance permittivities are expressed as a series in β :

$$\varepsilon_k = \varepsilon_k^{(0)} + \beta \varepsilon_k^{(1)} + \beta^2 \varepsilon_k^{(2)} + \dots \quad (5.2)$$

Apparently, when d is small or ω is small (or λ is large), β vanishes and only the zero-order term exists, which recovers the electrostatic approximation. It has been demonstrated that the first-order radiation correction $\varepsilon_k^{(1)}$ is equal to zero for any shape of nanoparticle [93]. For the second-order radiation correction $\varepsilon_k^{(2)}$ the following formula has been derived [93]:

$$\varepsilon_k^{(2)} = \frac{(\varepsilon_0 - \varepsilon_k^{(0)}) \oint_S \tau_k^{(0)} \vec{n}_Q \cdot \vec{a}_k(Q) dS_Q}{\oint_S \tau_k^{(0)} \vec{n}_Q \cdot \vec{E}_k^{(0)}(Q) dS_Q}, \quad (5.3)$$

where $\vec{E}_k^{(0)}(Q)$ and $\vec{a}_k(Q)$ are defined as

$$\vec{E}_k^{(0)}(Q) = \frac{1}{4\pi\varepsilon_0} \oint_S \sigma_k^{(0)}(M) \frac{\vec{r}_{MQ}}{r_{MQ}} dS_M \quad (5.4)$$

$$\vec{a}_k(Q) = \frac{\varepsilon_0 - \varepsilon_k^{(0)}}{8\pi\varepsilon_0} \oint_S \frac{[\vec{n}_M \times \vec{E}_k^{(0)}(M)] \times \vec{r}_{MQ}}{r_{MQ}} dS_M. \quad (5.5)$$

Thus, the procedure of computing the second-order radiation corrections $\varepsilon_k^{(2)}$ for resonance values of nanoparticle permittivities is the following. First, boundary integral equations (1.35) and (1.33) are solved to find $\varepsilon_k^{(0)}$ and corresponding $\sigma_k^{(0)}(Q)$ and $\tau_k^{(0)}(Q)$. Subsequently, using $\sigma_k^{(0)}(Q)$ and formulas (5.4) and (5.5), $\vec{E}_k^{(0)}(Q)$ and $\vec{a}_k(Q)$ are computed. Finally, using formula (5.3), $\varepsilon_k^{(2)}$ is calculated. As soon as $\varepsilon_k^{(2)}$ is found, the resonance values of the nanoparticle permittivity are computed as follows:

$$\varepsilon_k = \varepsilon_k^{(0)} + \beta^2 \varepsilon_k^{(2)}. \quad (5.6)$$

Since ε_k is a function of frequency, the resonance frequencies of the plasmon modes occur at the frequencies where the following condition is satisfied (see Figure 5.1):

$$F(\omega_k) = \varepsilon'(\omega_k) - \beta(\omega_k)^2 \varepsilon_k^{(2)} = \varepsilon_k^{(0)}. \quad (5.7)$$

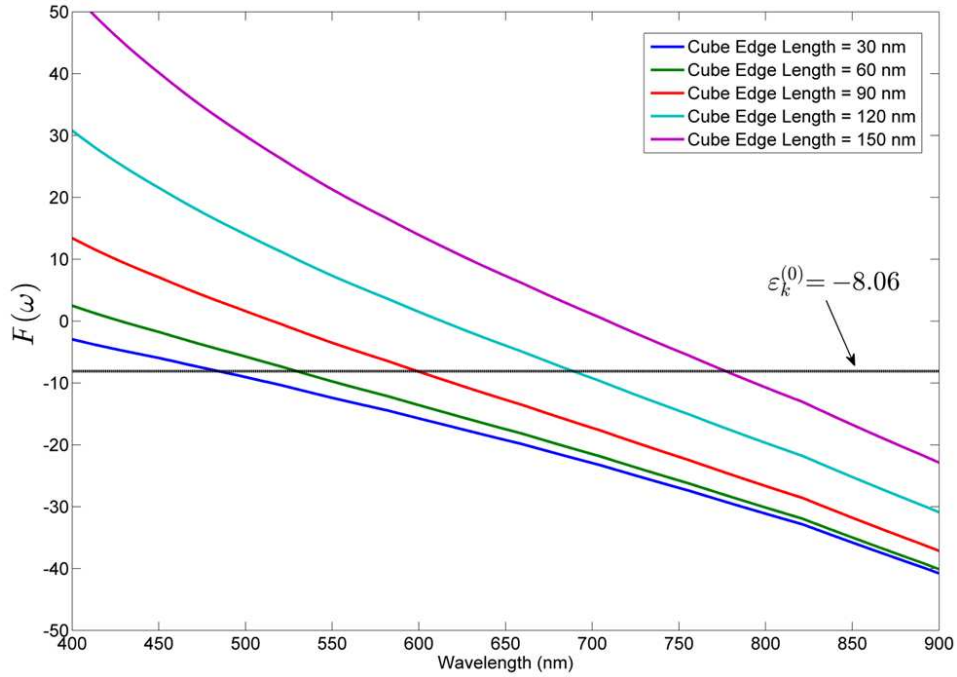


Figure 5.1: Determination of resonance wavelengths for radiation correction in formula (5.7) of a dipolar plasmon mode (Mode D1) in a single silver cube with various cube sizes.

5.2.2 Samples of Numerical Simulation Results

The preceding section succinctly details a computational method for determination of plasmon resonance frequencies of nanoparticles given their shape and dispersion relation $\varepsilon(\omega)$. First, the numerical simulation is performed for a single spherical particle with 5120 triangular patches in water environment. The computational results are compared with the results calculated by Mie theory. According to Mie theory, the corrected resonance dielectric permittivity can be expressed in the following equation:

$$\varepsilon_1 = -(2 + \frac{3}{5}\beta^2)\varepsilon_0 = -(2 + \frac{3}{5}\omega^2\mu_0\varepsilon_0d^2)\varepsilon_0, \quad (5.8)$$

where d is the diameter of the spherical nanoparticle. Figures 5.2 and 5.3 present the comparison between our method and Mie theory for spherical nanoparticles

in water. It is evident from Figure 5.2 that the resonance permittivity is decreased quadratically as the diameter is increased. Due to the dispersion relation of gold and silver, a decrease in the resonance permittivity results in a small redshift in the resonance wavelength of these metallic nanoparticles as their diameter increases. The calculation results also match values of plasmon resonance wavelengths for spherical nanoparticles of different diameters calculated in V. Myroshnychenko *et al.* [95].

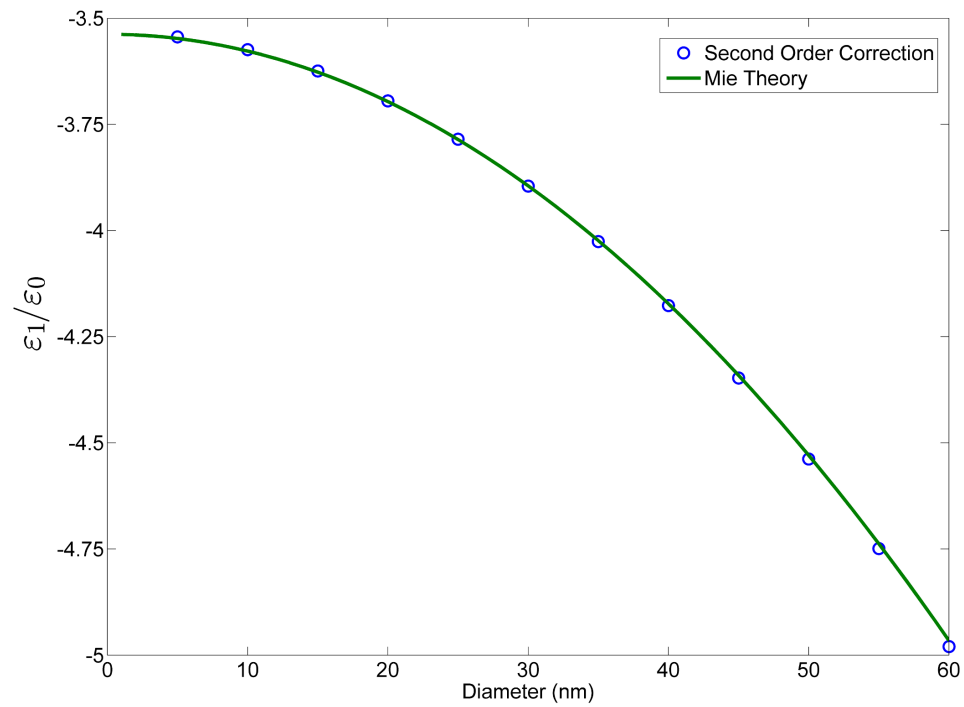


Figure 5.2: Comparison between the calculation of the resonance permittivity of the dipole plasmon modes using second-order radiation corrections (open circles) and Mie theory (solid line) for spherical nanoparticles in water as a function of nanosphere dimension.

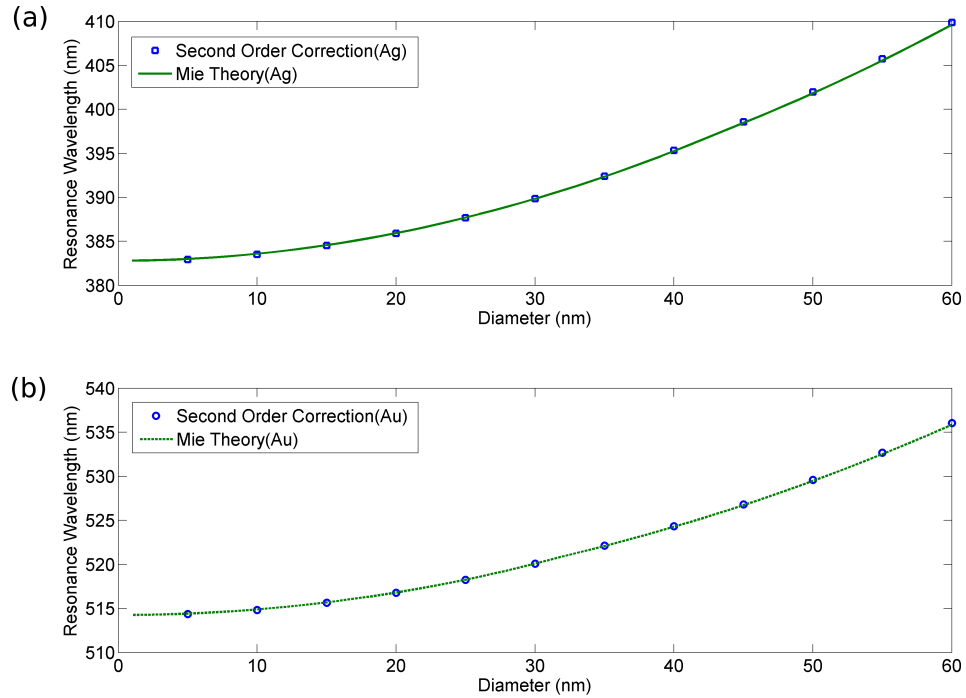


Figure 5.3: Comparison of the calculated dipole plasmon resonance wavelength of spherical nanoparticles in water computed by using second-order radiation corrections (open circles) and Mie theory (solid line). Data presented for (a) silver and (b) gold dispersion relations.

Next, we discuss the accuracy of this method in modeling a number of particle shapes with increasing complexity. Table 5.1, 5.2, and 5.3 present the results of computations of second-order radiation corrections for resonance wavelengths of dipole plasmon modes of gold nanorings placed on a glass substrates, silver nanocubes immersed in water and silver nanocubes placed on glass substrates, respectively. The complex permittivities of silver and gold have been obtained from the literature [113], and the dielectric constants of water and glass substrate were set to $1.77\epsilon_0$ and $2.25\epsilon_0$, respectively. It is evident from the presented data that the second-order radiation corrections result in a better agreement with experimental data than the results based on purely electrostatic analysis. These examples illustrate that a variety of plasmonic systems can be analyzed using the eigenvalue approach, including

but not limited to dense and hollow objects, objects with planar and non-planar surfaces, objects with sharp and rounded edges and corners, and objects immersed in infinite and semi-infinite dielectric media.

| Resonance Wavelength (nm) | Ring 1 (Thickest) | Ring 2 | Ring 3 (Thinnest) |
|---------------------------|----------------------|--------|----------------------|
| Electrostatic Approach | 940 | 1102 | 1159 |
| Second-Order Corrections | 987 | 1156 | 1214 |
| Experimental Data [96] | 1000 | 1180 | 1350 |

Table 5.1: Comparison for resonance wavelengths of gold nanorings placed on glass substrate.

| Resonance Wavelength (nm) | High-Frequency Mode | Low-Frequency Mode |
|---------------------------|---------------------|--------------------|
| Electrostatic Approach | 405 | 454 |
| Second-Order Corrections | 420 | 478 |
| Experimental Data [97] | 432 | 500 |

Table 5.2: Comparison for resonance wavelengths of silver nanocubes immersed in water.

| Resonance Wavelength (nm) | High-Frequency Mode | Low-Frequency Mode |
|---------------------------|---------------------|--------------------|
| Electrostatic Approach | 383 | 421 |
| Second-Order Corrections | 410 | 443 |
| Experimental Data [97] | 395 | 457 |

Table 5.3: Comparison for resonance wavelengths of silver nanocubes placed on glass substrate.

5.3 Dipolar Plasmon Modes in Silver Nanocubes

5.3.1 Experimental Measurement

A more detailed examination of the radiation correction theory is performed by comparing calculated results with experimental data collected from ensembles of silver nanocubes in aqueous suspensions. For this purpose, silver nanocubes were synthesized by the polyol reduction method ([99][100]). Until recently, fine control of the size of the resulting silver nanocubes has been a challenging task [101, 102]. Silver nanocubes have been synthesized by the polyol reduction process, in a similar fashion to the recent report by Tao *et al.* [114] 1,5-Pentanediol (Fluka, 97% and Acros, 98%), CuCl_2 (Sigma Aldrich), AgNO_3 (Alfa Aesar, 99.995%) and polyvinylpyrrolidone 55K (Sigma Aldrich) were used as received. The glassware was cleaned thoroughly before use. 15 mg CuCl_2 were dissolved in 2.5 mL pentanediol (PDOH) and the solution was aged for 10 days. 100 mg AgNO_3 were dissolved in 5 mL PDOH and 20 μL of the aged CuCl_2 solution were added. This mixture was sonicated for 90 min to yield a light orange solution (Ag solution). Separately, 200 mg polyvinylpyrrolidone (PVP) were dissolved in 10 mL PDOH (PVP solution). In a round-bottom flask, 5 mL of PDOH were heated in an oil bath set to 190°C. The Ag solution was injected in 125 μL aliquots at regular intervals. The PVP solution was added dropwise between injections at a rate of $\sim 160 \mu\text{L min}^{-1}$. The size of the nanocubes was controlled by adjusting the number of Ag solution injections and the time intervals between injections.

In this synthesis protocol, control over the mean size of the nanocubes is achieved

by adjusting the timing of the additions of the silver ions and the polymeric surfactant to the reaction mixture. We successfully prepared monodispersed nanocube suspensions for cubes 50 to 150 nm in edge length. Larger mean sizes of silver cubes could be achieved, yet the size distribution is thus far unsatisfactory for those preparations. The monodispersed silver nanocubes were characterized by scanning electron microscopy (SEM) and by UV-vis-NIR absorption in aqueous suspensions (see Figure 5.4). SEM images of the silver nanoparticles indicate that the vast majority of the particles in the as-made suspension have a cubic shape and a common size (Fig. 5.4a). The optical absorption spectrum of the nanocubes in water displays a number of absorption maxima in the wavelength range of 300 to 900 nm. Absorption maxima were determined by fitting each spectrum to a sum of 2 to 6 Lorentzian peak functions using Origin8. As shown in Fig. 5.4d, the location of these absorption maxima is size-dependent. An increase in the size, and thus in the contribution of retardation effects, leads to a red shift in the absorption maxima [103]. In particular, the absorption band with the longest wavelength shifts from ~ 450 nm to ~ 750 nm as the mean size of the cubes increases from 50 nm to 150 nm. This absorption peak becomes broad and relatively less pronounced as the cube size increases. The interpretation of the spectra of plasmonic nanocubes has not been consistent across the literature because of the scarcity of size controlled samples, the spectral sensitivity to the sharpness of the corners of the cubes, and the need to include radiation effects in theoretical modeling ([100],[102],[107]-[110]).

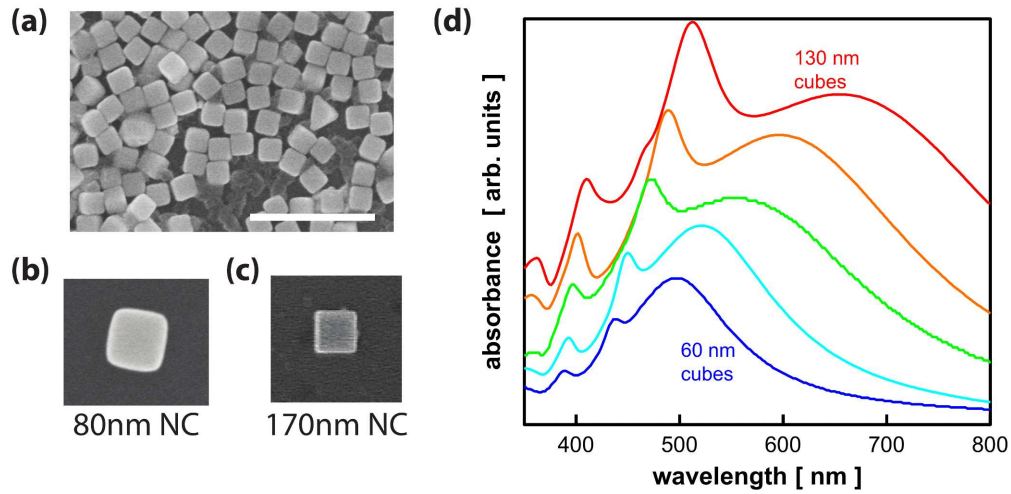


Figure 5.4: (a-c) SEM image of nanocubes. (a) An ensemble of silver nanocubes. Scale bar: 500 nm. (b) A small nanocube with rounded corners. (c) A large nanocube with sharp corners. (d) Absorption spectra of five types of silver nanocubes (in water). As the size of the nanocube increases, the absorbance peaks due to plasmon resonances shift to longer wavelengths.

5.3.2 Numerical Simulation

Theoretical modeling demonstrates that plasmonic resonance modes supported by the silver nanocubes are the origin of the features seen in the absorption spectra. The peaks (maxima) in the extinction spectra are identified with the resonance wavelengths of different plasmon modes. These values, and their dependence on cube size can be predicted theoretically as long as radiation corrections are included. We calculate $\varepsilon_k^{(0)}$, $\sigma_k^{(0)}$, and $\tau_k^{(0)}$ for the numerous plasmon resonance modes of metal nanocubes in the quasistatic approximation. Several of these modes are dipolar in nature, while the rest are of higher multipole characteristics. As will be shown, it is sufficient to consider just the dipolar modes to understand the absorption spectra of nanocubes suspended in water. For each dipolar mode, the dipole moment was calculated by using

$$\vec{p}_k^{(0)} = \oint_s \vec{r}_Q \sigma_k^{(0)}(Q) dS_Q. \quad (5.9)$$

It is important to mention that, to calculate the dipole moment strength of each plasmon mode, $\sigma_k^{(0)}$ and $\tau_k^{(0)}$ have to be properly normalized [93]. We identified the resonance modes with the strongest dipole moments. In the case of silver NCs in water, these plasmon resonances, denoted as D1-D8, occur at 468, 427, 405, 399, 398, 375, 339, and 332 nm, respectively. In Table 5.5, the surface charge density distributions ($\sigma_k^{(0)}(Q)$) corresponding to each of the eight modes are displayed. It can be appreciated that these modes can couple strongly to electromagnetic wave excitations due to the antisymmetric (dipolar) distribution of charges along one of the main axes of the cubic system. These dipole plasmon modes mostly coincide with the modes presented in other works [105, 106], except for mode “D3”. This inconsistency on the charge distribution for mode “D3” may originate from different number of patches used for cube in the calculations. As shown in Tables 5.4 and 5.5, by using a larger number of patches for the cube, more detailed oscillation of the charges along the cube edges is revealed.

Mesh Elements = 864

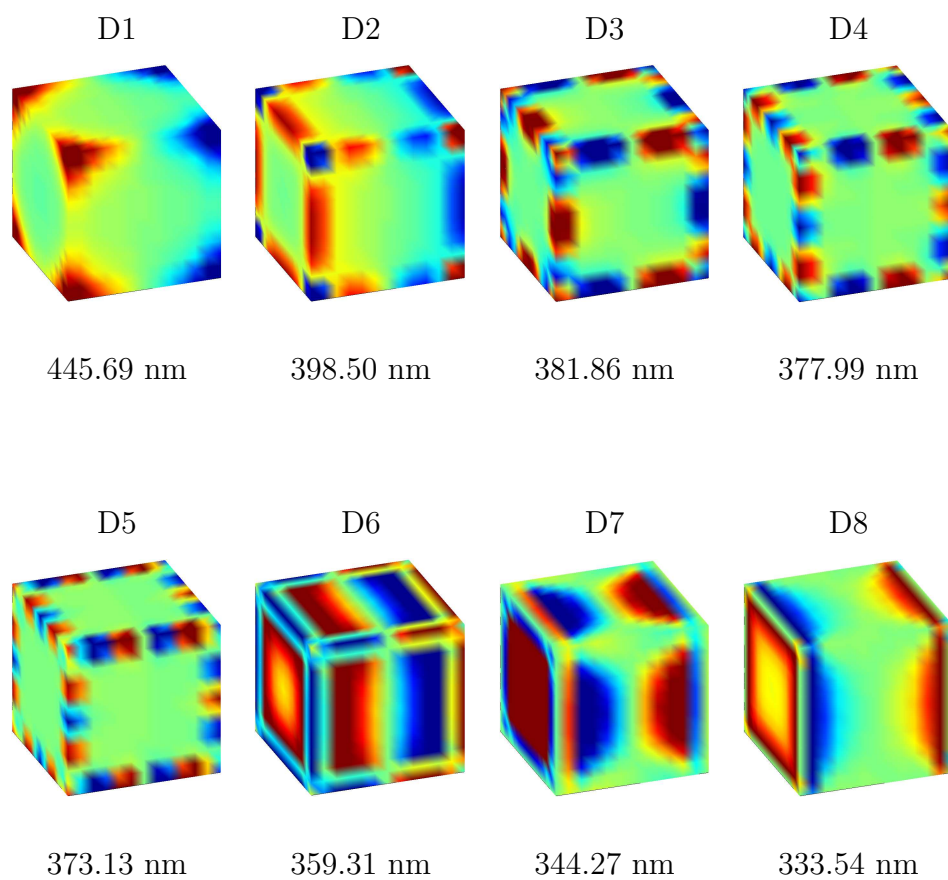
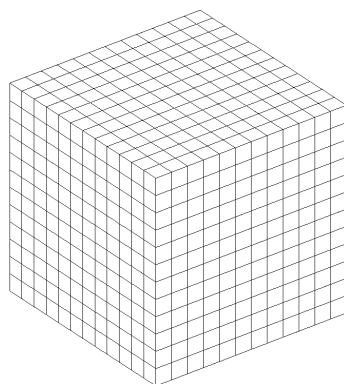


Table 5.4: Calculated surface charge distributions for the eight strongest dipole plasmon modes and the corresponding resonance wavelengths for a single silver cube in water with 864 square patches.

Mesh Elements = 38400

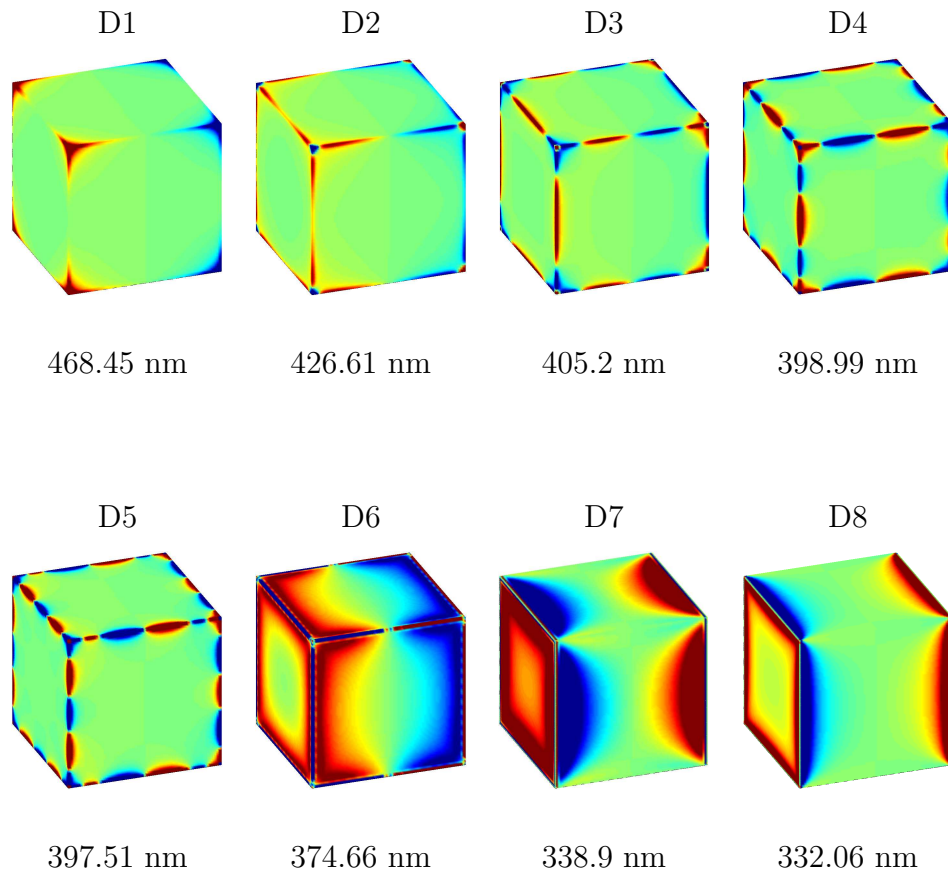
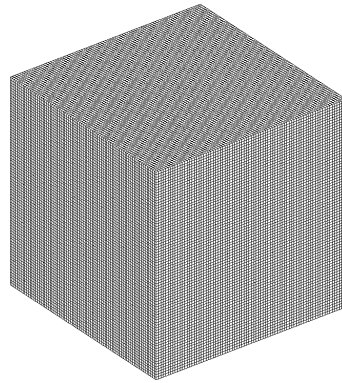


Table 5.5: Calculated surface charge distributions for the eight strongest dipole plasmon modes and the corresponding resonance wavelengths for a single silver cube in water with 38400 square patches.

By using Eqs. (5.3)-(5.7), the second-order corrections for the resonance wavelengths of all these eight dipolar plasmon modes are computed. The experimental and computational results for the resonance wavelengths of the five strongest dipole plasmon modes in Table 5.5 are compared in Figure 5.5.

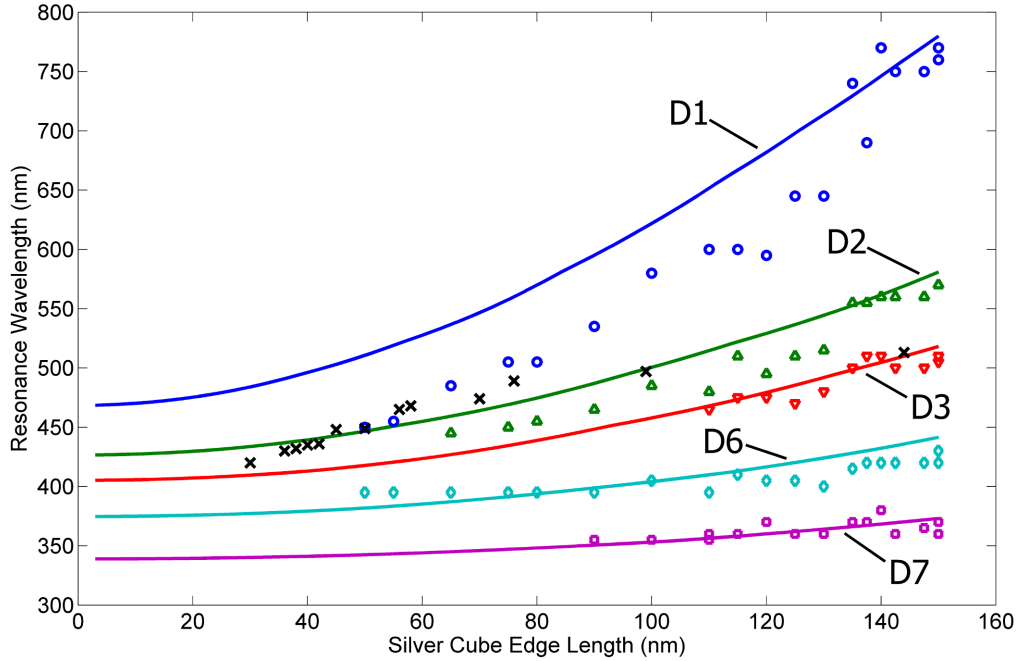


Figure 5.5: Comparison between calculated (solid lines) and measured (open symbols) resonance wavelengths for five dipole plasmon modes of silver nanocubes. The solid symbols is experimental data for the major plasmon resonance wavelength from [101] and [102]

5.4 Results and Discussions

Figure 5.5 shows an overall good agreement between the predictions of the outlined radiation correction theory and the experimental data. Considering the experimental error associated with determining the resonance wavelength from the extinction spectra, particularly for overlapping absorption peaks, the size depen-

dence of the plasmon resonance wavelengths in silver nanocubes was determined exceedingly well through the calculations without the need for fitting parameters. In our computational results, mode “D4”, “D5”, and “D8” also contribute to the peaks at 400 nm and 340 nm; however, their contributions are less pronounced due to their weaker dipole moments (see Table 5.6). In Fig. 5.5, a non-linear relationship between wavelength and cube size is revealed both experimentally and computationally. Previously, a linear relationship between the major plasmon resonance wavelength and the cube size was hypothesized based on results from a narrow range of sizes [101]. Here, we show that a quadratic relationship between the resonance *permittivity* and the cube size is adequate to reproduce the experimental results. There is no one function that can relate the plasmon resonance wavelength to particle size, because of its dependence on the dispersion of the material.

| Mode | $\varepsilon_k^{(0)}/\varepsilon_0(\text{water})$ | $2\pi c/\omega_k^{(0)}(\text{water})$ | $ p_k^{(0)} (\text{relative})$ |
|------|---|---------------------------------------|--------------------------------|
| D1 | -8.0602 | 468.45 nm | 0.9103 |
| D2 | -5.8599 | 426.61 nm | 1.0000 |
| D3 | -4.7187 | 405.20 nm | 0.6305 |
| D4 | -4.3716 | 398.99 nm | 0.2749 |
| D5 | -4.2901 | 397.51 nm | 0.1849 |
| D6 | -3.1001 | 374.66 nm | 0.5928 |
| D7 | -1.0630 | 338.90 nm | 0.6030 |
| D8 | -0.6858 | 332.06 nm | 0.3915 |

Table 5.6: Calculated resonance permittivities, resonance wavelengths, and dipole moments for dipolar modes D1-D8.

Further examination of the data suggests that there is some discrepancy between the resonance values determined computationally and experimentally for plasmon mode “D1”, the mode with the longest resonance wavelength and the most pronounced size dependence. The discrepancy is systematic, with the numerical calculations predicting higher wavelength values than the measured values. The discrepancy is less severe for larger cube dimensions. The sensitivity of the resonance wavelength value to the corner geometry of the nanocubes is a plausible explanation for these observations [108]. The corner geometry (*i.e.*, sharpness of the corners) cannot be entirely controlled during the chemical process of nanocube growth. Because the silver nanoparticles first nucleate as spherical seeds and their faceted structures only develop at a later stage, syntheses of smaller silver nanocubes

tend to result in particles with more rounded corners, as evidenced by SEM microscopy (Fig. 5.4(b) and 5.4(c)). We anticipate that the corner geometry will have the maximum influence on the properties of mode “D1” because the charge density associated with this mode is the highest at the corners of the cube (see Table 5.5) [107]. To test this explanation, the computation of the resonance wavelength of the dipole plasmon modes was performed for nanocubes with smoothed (“rounded”) corners and edges. The computational results for nanocubes with rounded corners do indeed shift towards shorter wavelengths and this blue-shift is appreciably higher for mode “D1” than for the other plasmon modes (Fig. 5.6). Thus, better agreement between the radiation corrections and the experimental data can be achieved by considering the radius of curvature of the corners in addition to the cube size. This analysis also explains the small shift (~ 10 nm) we have observed in the absorption peak attributed to mode “D1” after extended storage of the nanocube suspensions in air. Similar spectral shifts have been reported, experimentally and theoretically, for a range of plasmonic nanoparticles whose corners were intentionally rounded or truncated [103, 108, 109, 97].

Furthermore, the sensitivities of the first and second peaks to the sharpness of the edges and corners provide the explanations of the broadening and diminishing of the peak for mode “D1”, and the enhancing of the peak for mode “D2” in Figure 5.4d due to the non-uniformity of the corner sharpness in ensemble nanocubes. It can be remarked that Figures 5.5 and 5.6 suggest that the radiation corrections are quite accurate if overall nanocube dimensions (*i.e.*, their diameters) do not exceed one-half of a resonance wavelength. It is also evident from Figures 5.3, 5.5, and

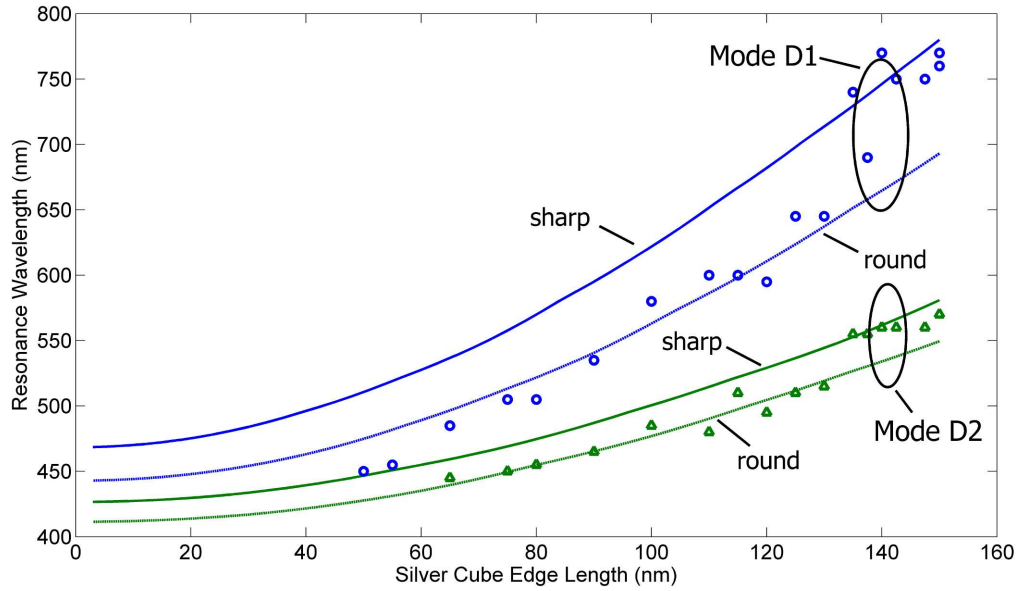


Figure 5.6: The fitting of experimental data by computational results for nanocubes with ideal sharp corners and for cubes with rounded corners.

5.6 that resonance wavelengths increase (red-shift) with the increase in nanoparticle dimensions. This may have a positive effect because the ratio of the real to imaginary parts of the permittivities of gold and silver is the largest in the 600 nm to 900 nm wavelength range and this larger ratio leads to stronger pronounced plasmon resonances [111].

The presented radiation corrections may be quite useful for the calculation of resonance wavelengths for metallic nanoparticle clusters. The overall dimensions of such clusters may be comparable with the resonance wavelengths and requiring the inclusion of retardation effects in modeling their plasmonic response. Since nanoparticle clusters are used in various applications, for instance, in SERS studies, reliable and efficient simulation tools may impact progress in these fields. As an example, we discuss here the computational results for resonance wavelengths of face-to-face nanocube dimers on a glass substrate. SERS studies for utilizing dimers have been

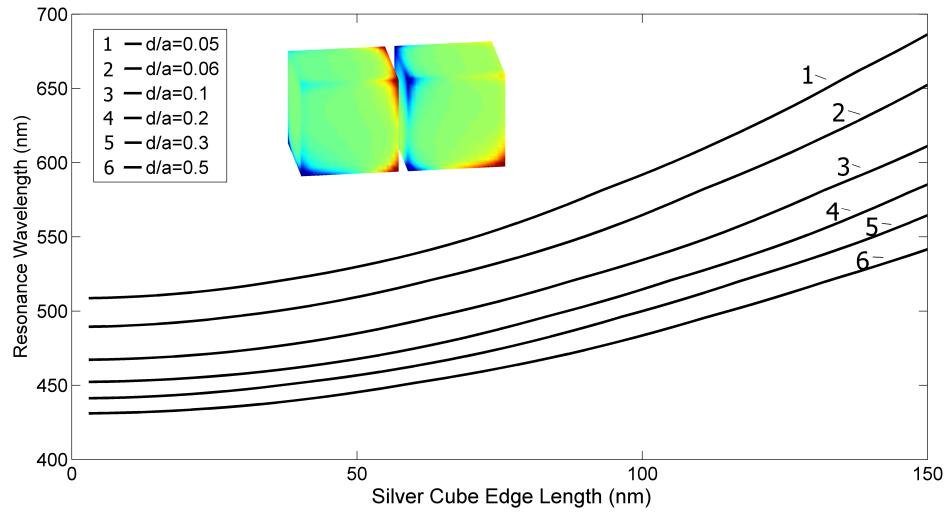


Figure 5.7: Calculated resonance wavelengths of main dipole mode for face-to-face dimers with various cube sides and gaps.

carried out in previous work [112]. Figure 5.7 presents the results of computations for various nanocube edge lengths and various “gap-to-cube side” ratios. This figure reveals that the resonance wavelengths are quite sensitive to this ratio. The computational data from Figure 5.7 may be useful for the extraction of nanocube separation from extinction cross section measurements of resonance wavelengths.

The radiation corrections for computing the negative resonance values of the permittivity of metallic nanoparticles have been presented. These radiation corrections have been tested by comparing the calculation results for a single sphere with known analytical solutions, and for a single nanoring and a single nanocube with available experimental data. The performed comparison suggests that the radiation corrections are quite accurate when nanoparticle dimensions are less than one-half of a resonance wavelength. Furthermore, it has been observed that the calculations for the nanocubes with rounded corners show better agreement with the experimental data than those for the nanocubes with sharp corners. Finally, the resonance wave-

lengths for face-to-face silver nanocube dimers with different sizes placed on a glass substrate are reported. These computational data may be useful for the deduction of gap distances, or serving as a reference for choosing gap distances for the dimers during their synthesizing process. This suggests that the radiation corrections can be used to gauge the size of plasmonic nanoparticles as well as shape deviations based on spectroscopy data, for example, during the optimization of a synthetic route.

Chapter 6

Conclusion and Future Work

In conclusion, throughout this work, we have explored various applications of plasmon resonances in metallic nanoparticles. These applications include, surface-enhanced Raman scattering (SERS), all-optical magnetic recording, and heat-assisted magnetic recording (HAMR). For SERS application, the plasmonic structures are designed to obtain high SERS signals. The strength of the signals of Raman-shifted light depend on the resonance wavelengths of the plasmonic structures, which are associated with the geometric configurations of the dimers. Consequently, the plasmonic structures for SERS substrate have to be designed to achieve high signal enhancements as well as to minimize the heterogeneity of the SSEF. In our case, we demonstrated that face-to-edge dimers should be considered the most suitable for practical application, since they displayed high uniformity of signal enhancement and the largest average magnitude of this enhancement.

For all-optical magnetic recording applications, we pointed out that for the particles with rotational symmetry, there exist two identical dipolar plasmon modes but rotated in space by 90 degree, whose plasmon resonance frequencies are identical. They formed the so-called circularly polarized dipolar plasmon modes which result in the enhancement of the circularly polarized light and preserve the circularly polarized nature. We provided the analytical solution of the plasmon modes for

spheroidal nanoshells, and compared the light intensity enhancement generated by their circularly polarized dipolar plasmon modes with the one generated by spherical nanoshells. We found that spheroidal nanoshells are superior to spherical nanoshells as far as the circularly polarized light enhancing and focusing are concerned.

In Chap. 4, we developed a computational methodology to calculate the resonance wavelengths of metallic nanostructures in the proximity of a dielectric object with arbitrary shape. We demonstrated this method by considering two examples of metallic nanostructures used in HAMR, T-aperture gold nanofilms and lollipop gold nanodisks. In the absence of the heat sink layers, both structures produced well-focused optical spots with high light intensities. However, in the presence of heat sink layers, the induced charges on the heat sink layers change the light intensities of their optical spots. From our calculation results, the presence of heat sink layers may be detrimental to the aperture-type of metallic nanostructures but beneficial for the metallic nanostructures with protruding parts, which has to be considered when designing the metallic nanoparticles for HAMR application.

In Chap. 5, we studied the peaks in optical absorption spectrum collected from ensembles of silver nanocubes with various sizes in aqueous suspensions by using radiation correction technique. We identified the first strongest eight dipolar plasmon modes in single silver nanocube by using eigenmode technique, and we performed the radiation correction calculations for these dipolar plasmon modes. It has been revealed that the dipolar plasmon modes in single nanocube are enough to understand the measured absorption spectrum. We also found out that by considering different radii of the curvature of cube corners, the better agreement between

radiation corrections and the experimental data can be achieved.

Future Work

In the calculation in Chap. 2, we assume that the resonance frequencies of plasmon modes are not affected by the presence of the surrounding molecules, and the excitation of the plasmon modes from the Raman-shifted light is not spatially uniform. Therefore, the shifts in resonance frequencies of plasmon modes due to the presence of surrounding molecules have to be studied. For non-uniform excitation of plasmon modes from Raman-shifted light, we have modeled the excitation of plasmon modes from Raman-shifted light by considering the molecules as point-like dipoles in Appendix A,. However, we only performed this calculation for a single nanocube located on a silicon substrate. More calculations for different nanoparticles and comparison with experimental data are needed to test the accuracy of this model.

In Chap. 4, we developed a computational methodology to calculate the resonance wavelengths of metallic nanostructures in the proximity of a dielectric object with arbitrary shape. It can be seen that this technique can be extended to solve the plasmon modes of a metallic nanostructures surrounded by multiple dielectric objects, including recording medium and recording head. In this case, one has to perform the matrix inversion for more than one fully-populated matrix. This process makes the whole calculation costly and a more efficient way to compute the inversion of a matrix is needed to speed up this part of calculation.

Appendix A

Non-Uniform Excitation of Plasmon Resonances by a Single Molecule

In Chap. 2, we studied the SERS enhancement factors for silver nanocube clusters, including monomers and dimers. As mentioned in Chap. 2, the SERS enhancement contains two stages of enhancement of incident radiation. First, incident radiation excites the plasmon modes in metallic nanoparticles. Then, the strong localized field generated by the plasmon modes interacts with the surrounding molecules. These molecules generate another electric field at Raman frequency which excites the plasmon modes in the metallic nanoparticles again. Finally, the total resulting field at Raman frequency from the nanoparticle is then measured. In the numerical calculation in Chap. 2, we assume that the excitation of the plasmon modes from the Raman scattering light generated by the molecules is spatially uniform. However, this is not true, although the overall calculation results are consistent with the experimental work. To investigate the issue of the non-uniform excitation from the molecules, first we consider a molecule located at point m close to the boundary of a metallic nanoparticle. We model the molecule as a point-like dipole with dipole moment \mathbf{p} , which is defined by

$$\mathbf{p}(m) = \beta \mathbf{E}_L(m), \quad (\text{A.1})$$

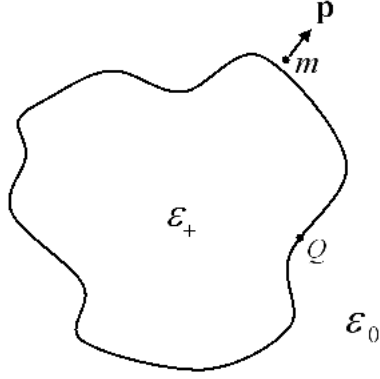


Figure A.1: A molecule nearby a metallic nanoparticle

where β is the polarizability of the molecule and $\mathbf{E}_L(m)$ is the local field at point m . According to [115], the polarizability β of a molecule can be expressed as

$$\beta = \beta_0 + \beta_\nu \sin \omega_\nu t, \quad (\text{A.2})$$

where β_0 is the equilibrium polarizability, β_ν is a constant for one specific vibrational mode in the molecule, and ω_ν is the frequency of this vibration. Now we consider the local field at point m is time-varying and sinusoidally oscillating with frequency ω_0 . Therefore, (A.1) is rewritten as

$$\mathbf{p}(m, t) = \beta \mathbf{E}_L(m, t), \quad (\text{A.3})$$

$$= (\beta_0 + \beta_\nu \sin \omega_\nu t) \mathbf{E}_L(m) \sin \omega_0 t, \quad (\text{A.4})$$

$$= \beta_0 \mathbf{E}_L(m) \sin \omega_0 t + \beta_\nu \mathbf{E}_L(m) \sin \omega_\nu \sin \omega_0 t, \quad (\text{A.5})$$

$$= \beta_0 \mathbf{E}_L(m) \sin \omega_0 t + \frac{1}{2} \beta_\nu \mathbf{E}_L(m) (\cos \omega_s t - \cos \omega_{ast}), \quad (\text{A.6})$$

where $\omega_s = \omega_\nu - \omega_0$ and $\omega_{as} = \omega_\nu + \omega_0$. (A.6) shows the dipole moments for Rayleigh scattering, Stokes Raman scattering, and Anti-Stokes Raman scattering, respectively. Here, since we are only interested in the Stokes Raman shift, we define its dipole moment as follows:

$$\mathbf{p}_s(m, t) = \frac{1}{2}\beta_\nu \mathbf{E}_L(m) \cos \omega_s t. \quad (\text{A.7})$$

In frequency domain, it becomes

$$\tilde{\mathbf{p}}_s(m, \omega) = \frac{1}{2}\beta_\nu \mathbf{E}_L(m) \sqrt{\frac{\pi}{2}} [\delta(\omega - \omega_s) + \delta(\omega + \omega_s)], \quad (\text{A.8})$$

$$= \frac{1}{2} \sqrt{\frac{\pi}{2}} \beta_\nu \mathbf{E}_L(m) \tilde{f}(\omega). \quad (\text{A.9})$$

In this way, the near-zone field [27] generated by this dipole moment can be written as

$$\tilde{\mathbf{E}}^m(Q, \omega) = \frac{1}{4\pi\epsilon_0 r_{mQ}^3} \{3\mathbf{r}_{mQ}[\mathbf{r}_{mQ} \cdot \tilde{\mathbf{p}}_s(m, \omega)] - \tilde{\mathbf{p}}_s(m, \omega)\}. \quad (\text{A.10})$$

This $\tilde{\mathbf{E}}^m(Q, \omega)$ describes the field at point Q on the metallic particle generated by the molecule located at position m . This is the field that excites the plasmon modes of the metallic nanoparticle at the second stage. According to [26], the expansion coefficient of each plasmon mode in the particle by any excitation source is in the following form:

$$\tilde{a}_k(\omega) = \frac{2\epsilon_0\lambda_k[\epsilon(\omega) - \epsilon_0]}{2\epsilon_0\lambda_k + [\epsilon(\omega) - \epsilon_0](\lambda_k - 1)} \oint_S \tilde{\mathbf{E}}_n^{(0)}(Q, \omega) \tau_k(Q) dS_Q,$$

where $\tilde{\mathbf{E}}_n^{(0)}(Q, \omega)$ is the normal component of the incident field (of any type) at point Q . By substituting $\tilde{\mathbf{E}}_n^{(0)}(Q, \omega)$ with $\tilde{\mathbf{E}}_n^m(Q, \omega)$, we obtain the following formula:

$$\begin{aligned}
\tilde{a}_k(\omega) &= \frac{2\epsilon_0\lambda_k[\epsilon(\omega) - \epsilon_0]}{2\epsilon_0\lambda_k + [\epsilon(\omega) - \epsilon_0](\lambda_k - 1)} \oint_S \tilde{\mathbf{E}}_n^{(0)}(Q, \omega) \tau_k(Q) dS_Q \\
&= \frac{(\epsilon(\omega) - \epsilon_0)(\epsilon_k - \epsilon_0)}{\epsilon_k - \epsilon(\omega)} \times \\
&\quad \oint_S \frac{1}{4\pi\epsilon_0 r_{mQ}^3} \{3\mathbf{r}_{mQ}[\mathbf{r}_{mQ} \cdot \tilde{\mathbf{p}}_s(m, \omega)] - \tilde{\mathbf{p}}_s(m, \omega)\} \cdot \mathbf{n}_Q \tau_k(Q) dS_Q \\
&= \frac{\beta_\nu(\epsilon_k - \epsilon_0)}{8\pi\epsilon_0} \sqrt{\frac{\pi}{2}} G(m) \tilde{g}_k(\omega) \tilde{f}(\omega), \tag{A.11}
\end{aligned}$$

where

$$\tilde{g}_k(\omega) = \frac{\epsilon(\omega) - \epsilon_0}{\epsilon_k - \epsilon(\omega)}, \quad G_k(m) = \oint_S \frac{1}{r_{mQ}^3} \{3\mathbf{r}_{mQ}[\mathbf{r}_{mQ} \cdot \mathbf{E}_L(m)] - \mathbf{E}_L(m)\} \cdot \mathbf{n}_Q \tau_k(Q) dS_Q. \tag{A.12}$$

It can be seen that $G_k(m)$ is a geometric factor which depends on the location of the molecule, and $\mathbf{E}_L(m)$ is the electric field created by the dipole mode at the molecule's location. Note that τ_k is for any mode k in the nanoparticle. For this reason, in the second stage, this molecule can not only excite dipole modes, but also non-dipole modes of the metallic nanoparticle. In order to obtain $\tilde{a}_k(\omega)$ in time domain, we take the inverse Fourier transform of (A.11) and obtain the following equation:

$$a_k(t) = \frac{1}{\sqrt{2\pi}} \int_{-\infty}^{\infty} \tilde{a}_k(\omega) e^{-i\omega t} d\omega \tag{A.13}$$

$$= \frac{\beta_\nu(\epsilon_k - \epsilon_0)}{16\pi\epsilon_0} G(m) \underbrace{\int_{-\infty}^{\infty} \tilde{g}_k(\omega) \tilde{f}(\omega) e^{-i\omega t} d\omega}_A. \tag{A.14}$$

Then, A can be derived as the following:

$$A = \int_{-\infty}^{\infty} \tilde{g}_k(\omega) \tilde{f}(\omega) e^{-i\omega t} d\omega \quad (\text{A.15})$$

$$= \int_{-\infty}^{\infty} \frac{\epsilon(\omega) - \epsilon_0}{\epsilon(\omega) - \epsilon_k} [\delta(\omega - \omega_s) + \delta(\omega + \omega_s)] e^{-i\omega t} d\omega \quad (\text{A.16})$$

$$\begin{aligned} &= \frac{\epsilon'(\omega_s) + i\epsilon''(\omega_s) - \epsilon_0}{\epsilon_k - \epsilon'(\omega_s) - i\epsilon''(\omega_s)} [\cos \omega_s t - i \sin \omega_s t] \\ &\quad - \frac{\epsilon'(\omega_s) - i\epsilon''(\omega_s) - \epsilon_0}{\epsilon_k - \epsilon'(\omega_s) - i\epsilon''(\omega_s)} [\cos \omega_s t + i \sin \omega_s t] \\ &= \frac{2\{[\epsilon'(\omega_s) - \epsilon_0][\epsilon_k - \epsilon'(\omega_s)] - [\epsilon''(\omega_s)]^2\} \cos \omega_s t + 2\epsilon''(\omega_s)[\epsilon_k - \epsilon_0] \sin \omega_s t}{[\epsilon_k - \epsilon'(\omega_s)]^2 + [\epsilon''(\omega_s)]^2} \\ &= 2C(\omega_s) \cos(\omega_s t - \theta_s), \end{aligned} \quad (\text{A.17})$$

where

$$C(\omega_s) = \sqrt{\frac{[\epsilon'(\omega_s) - \epsilon_0]^2 + [\epsilon''(\omega_s)]^2}{[\epsilon_k - \epsilon'(\omega_s)]^2 + [\epsilon''(\omega_s)]^2}}. \quad (\text{A.18})$$

Finally, we obtain the $a_k(t)$.

$$a_k(t) = \frac{\beta_\nu(\epsilon_k - \epsilon_0)}{8\pi\epsilon_0} G_k(m) C(\omega_s) \cos(\omega_s t - \theta_s) \quad (\text{A.19})$$

$$= A_k(m, \omega_s) \cos(\omega_s t - \theta_s). \quad (\text{A.20})$$

It can be seen that, for a specific molecule, the amplitude of $A_k(m, \omega_s)$ depends on the location of the molecule, the frequency of the Raman scattering radiation, and which plasmon mode is excited. To test this derivation result, we consider again a single silver nanocube (cube edge length = 80 nm) located on a silicon substrate. The wavelength of the incident radiation is at 633 nm, and the Raman shift of a specific molecule subject to this incident radiation is at 678 nm. We assume the uniform incident field $\mathbf{E}_0 = 1\mathbf{e}_x$ at the first stage of excitation and the $\beta_\nu = 1$. We compute the $A_k(m, \omega_s)$ for dipole mode (533 nm), quadrupole mode (508 nm), and octupole mode (458 nm), with different locations of the molecule. Figures A.2-A.13

present the charge distributions and the corresponding computed $A_k(m, \omega_s)$ at different planes of location of the molecule for the dipole mode, quadrupole mode, and octupole. These results show that, after considering the second-stage excitation, the dipole mode still has the strongest expansion coefficient, and hence the strongest light intensity enhancement, while the contributions from the higher-order plasmon modes are less pronounced. This suggests that the SERS enhancement factor may be primarily dominated by dipolar plasmon modes. As one can see, $A_k(m, \omega_s)$ is large mostly at the locations near the corners, while for other positions of the molecules, their $A_k(m, \omega_s)$ are not strong. In other words, only at certain locations can this molecule efficiently excite the plasmon modes. These results may provide more physical foundation in understanding single-molecule SERS (SMSERS) ([116][117]). Furthermore, the blinking SERS signal has been observed at room temperature (RT) and suppressed by cooling to 77 K and recovered by warming to RT. Accordingly, the blinking is thermally activated, e.g., by diffusion of molecules between different sites on Ag particles. Based on our results, these sites are possibly attributed to the “hot-spots” (where the electric charges concentrate) in the metallic nanoparticles ([118]-[121]).

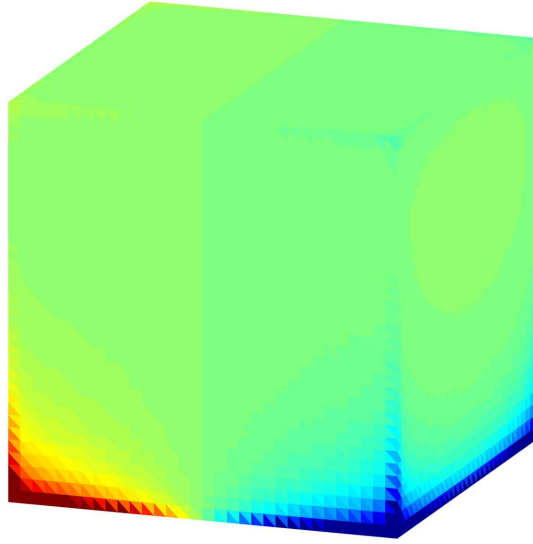


Figure A.2: Charge distribution for dipole mode.

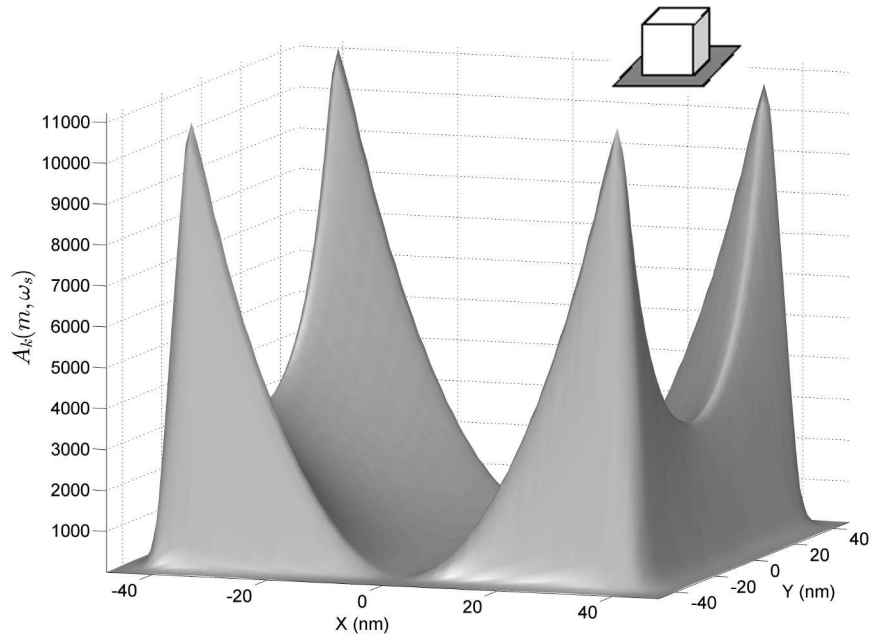


Figure A.3: Computed $A_k(m, \omega_s)$ on xy -plane for dipole mode.

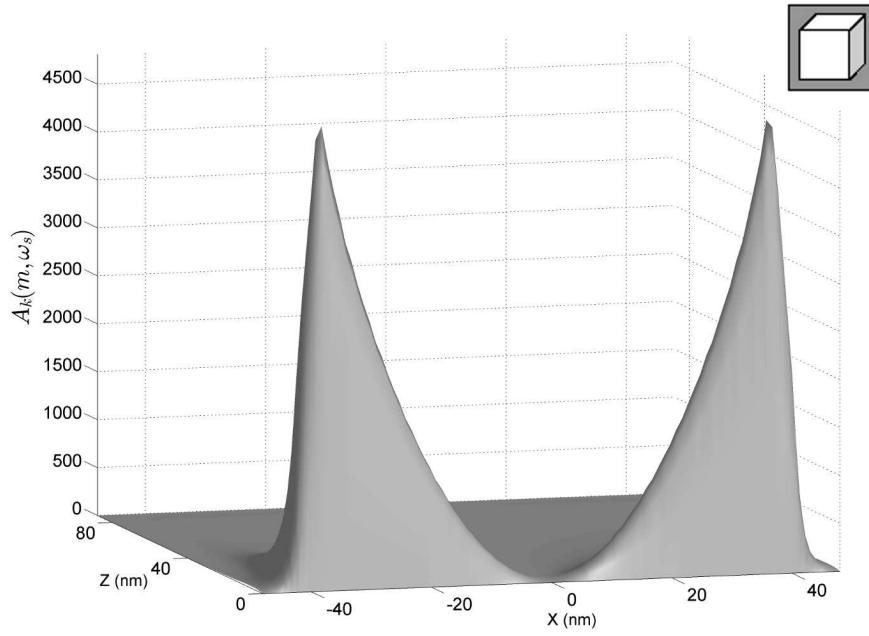


Figure A.4: Computed $A_k(m, \omega_s)$ on xz -plane for dipole mode.

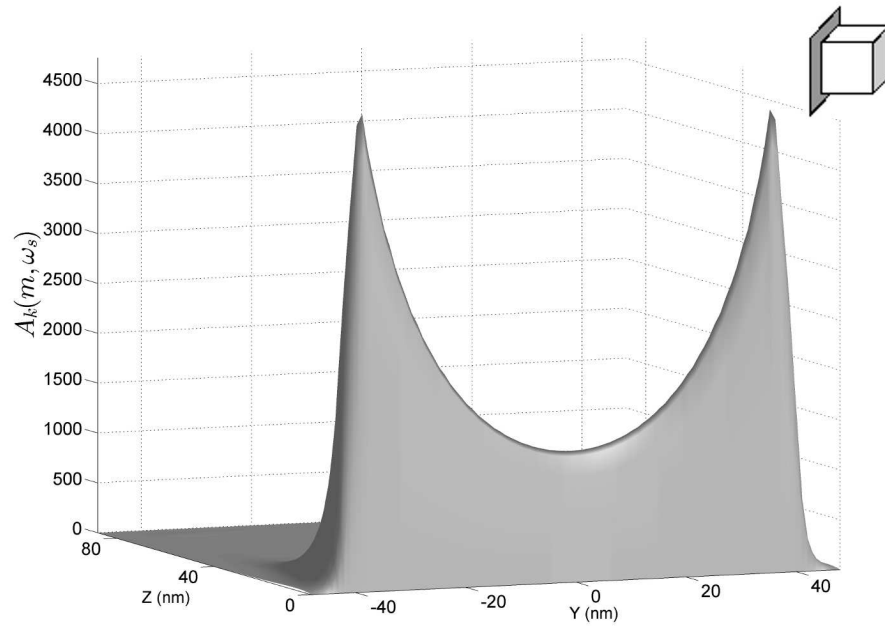


Figure A.5: Computed $A_k(m, \omega_s)$ on yz -plane for dipole mode.

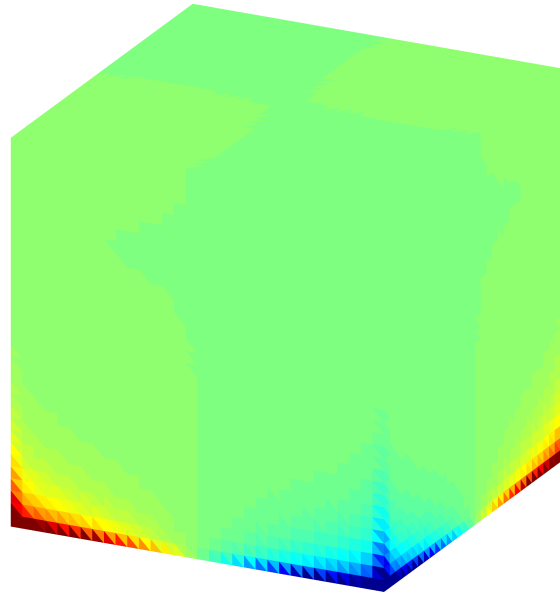


Figure A.6: Charge distribution for quadrupole mode.

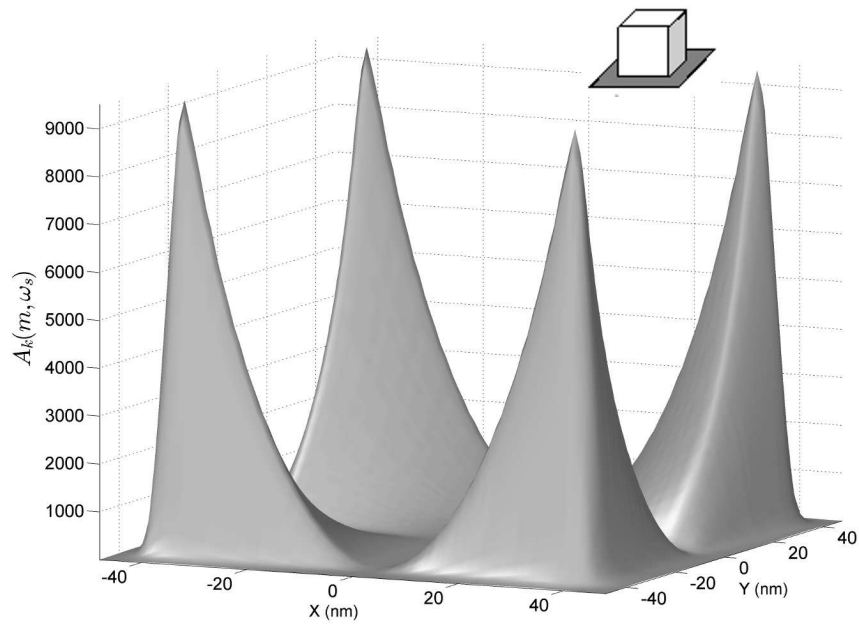


Figure A.7: Computed $A_k(m, \omega_s)$ on xy -plane for quadrupole mode.

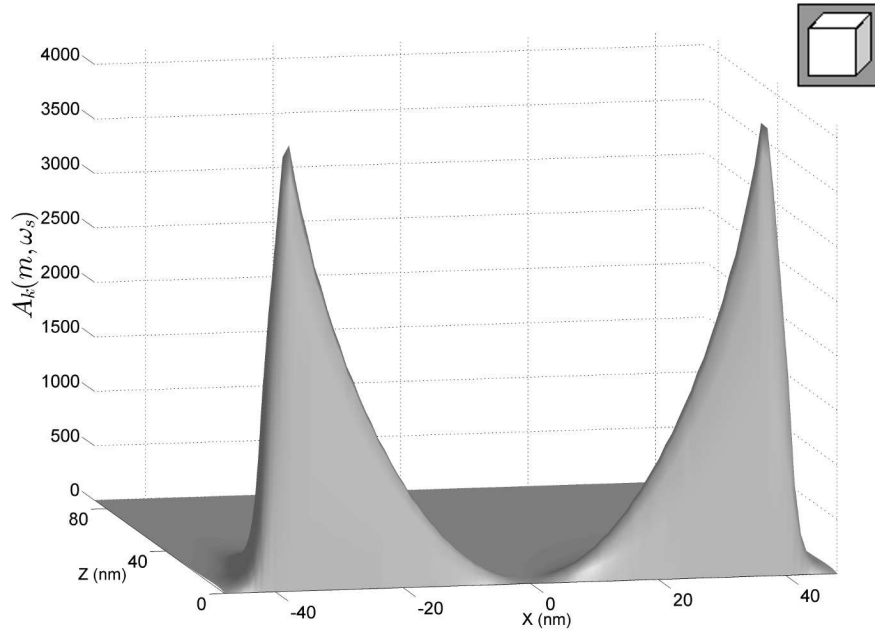


Figure A.8: Computed $A_k(m, \omega_s)$ on xz -plane for quadrupole mode.

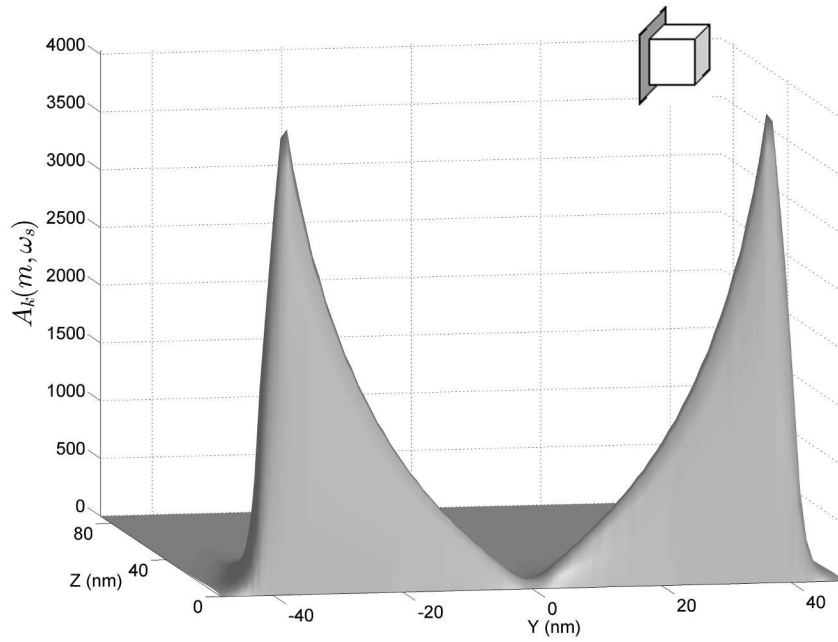


Figure A.9: Computed $A_k(m, \omega_s)$ on yz -plane for quadrupole mode.

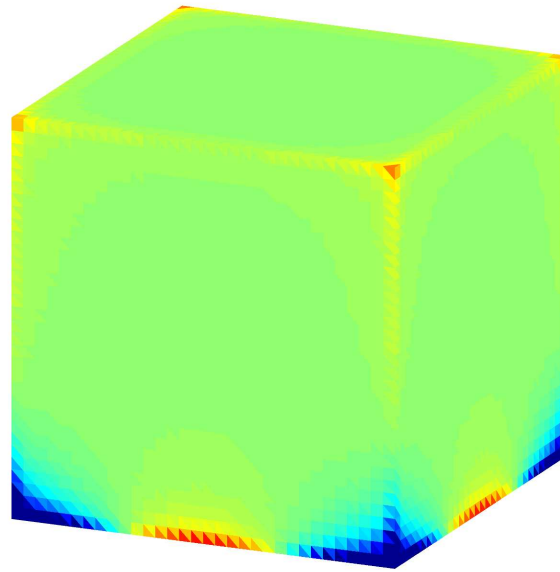


Figure A.10: Charge distribution for octupole mode.

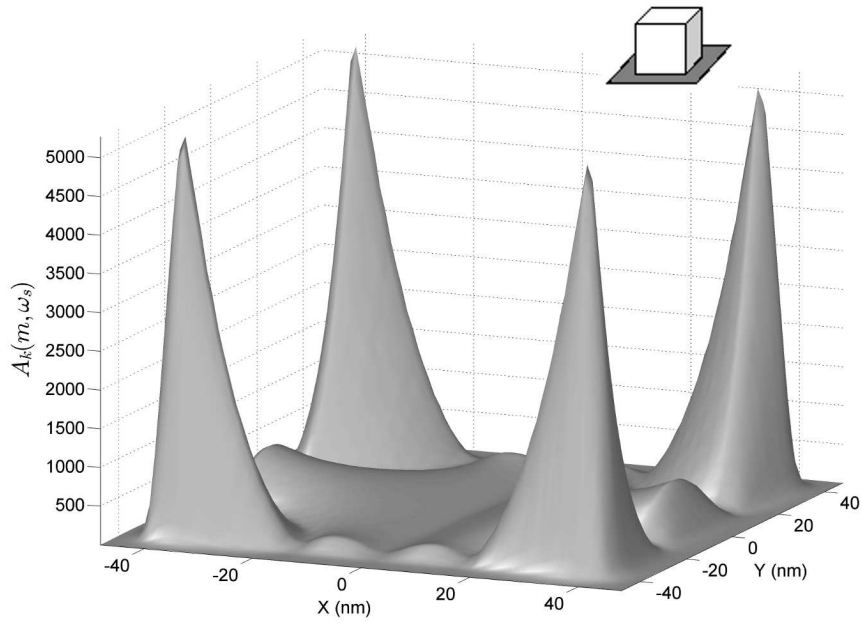


Figure A.11: Computed $A_k(m, \omega_s)$ on xy -plane for octupole mode.

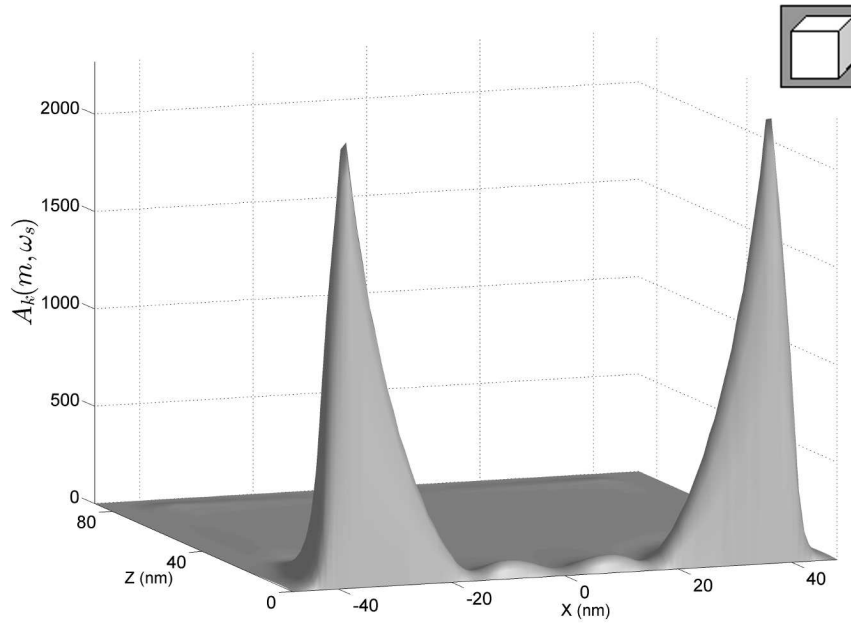


Figure A.12: Computed $A_k(m, \omega_s)$ on xz -plane for octupole mode.

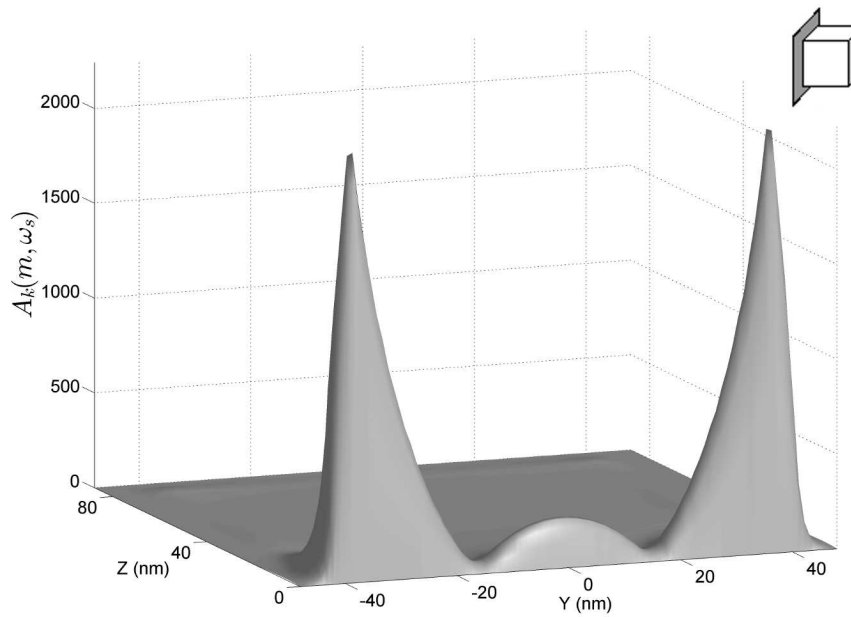


Figure A.13: Computed $A_k(m, \omega_s)$ on yz -plane for octupole mode.

Bibliography

- [1] I. D. Mayergoyz, *Plasmon Resonances in Nanoparticles.*, World Scientific, 2013.
- [2] T. J. Silva and S. Schultz, *Rev. Sci. Instrum.* **67**, 715 (1996).
- [3] R. M. Stockle, Y. D. Suh, V. Deckert, and R. Zenobi, *Phys. Lett.* **318**, 131 (2000).
- [4] J. C. Hulteen, D. A. Treichel, M. T. Smith, M. L. Duval, T. R. Jensen, and R. P. Van Duyne, *J. Phys. Chem. B* **103**, 3854 (1999).
- [5] R. Elghanian J. J. Storhoff, R. C. Mucic, R. L. Letsinger, and C. A. Mirkin, *Science* **277**, 1078 (1997).
- [6] S. Schultz, D. R. Smith, J. J. Mock, and D. A. Schultz, *Proc. Natl. Acad. Sci. U.S.A.* **97**, 996 (2000).
- [7] J. P. Kottmann, O. J. F. Martin, D. R. Smith, and S. Schultz, *Chem. Phys. Lett.* **341**, 1 (2001).
- [8] M. Moskovits, *Rev. Mod. Phys.* **57**, 783 (1985).
- [9] S. Nie and S. R. Emory, *Science* **275**, 1102 (1997).
- [10] H. Xu, E. J. Bjerneld, M. Kall, and L. Borjesson, *Phys. Rev. Lett.* **83**, 4357 (1999).
- [11] J. R. Krenn, A. Dereus, J. C. Weeber, E. Bourillot, Y. Lacroute, J. P. Goudonnet, G. Schider, W. Gotschy, A. Leitner, F. R. Aussenegg, and C. Girard, *Phys. Rev. Lett.* **82**, 2590 (1999).
- [12] J. C. Weeber, A. Dereux, C. Girard, J. R. Krenn, and J. P. Goudonnet, *Phys. Rev. B* **60**, 9061 (1999).
- [13] T. Yatsui, M. Kouroggi, and M. Ohtsu, *Appl. Phys. Lett.* **79**, 4583 (2001).
- [14] J. Tominnaga, C. Mihalcea, D. Buchel, H. Fukuda, T. Nakano, N. Atoda, H. Fuji, and T. Kikukawa, *Appl. Phys. Lett.* **78**, 2417 (2001).
- [15] J. Tominnaga, T. Nakano, and N. Atoda, *Proc. SPIE* **3467**, 282 (1999).

- [16] L. Men, J. Tominnaga, Q. C. H. Fuji, and N. Atoda, *Proc. SPIE* **4085**, 204 (2001).
- [17] P. Moon and D. E. Spencer, *Field Theory Handbook, Including Coordinate Systems, Differential Equations, and Their Solutions, 2nd ed* (New York: Springer-Verlag, 1988)
- [18] P. Morse and H. Feshbach, *Methods of Theoretical Physics, Part I* (McGraw-Hill, 1953).
- [19] R. A. Usmani, *Comp. Math. Applic.* **27**, No. 8, 59-66 (1994).
- [20] A. Gil and J. Segura, *Comp. Phys. Comm.* **105**, 273-283 (1997).
- [21] J. Segura and A. Gil, *Comp. Phys. Comm.* **124**, 104-122 (2000).
- [22] A. Gil and J. Segura, *Comp. Phys. Comm.* **139**, 186-191 (2001).
- [23] I. D. Mayergoyz, D. R. Fredkin, and Z. Zhang, *Phys. Rev. B* **72**, 155412 (2005).
- [24] O. D. Kellogg, *Foundations of Potential Theory* (McGraw-Hill, New York, 1929).
- [25] S. G. Mikhlin, *Mathematical Physics, and Advanced Course* (North-Holland, Amsterdam, 1970).
- [26] I. D. Mayergoyz, Z. Zhang, and G. Miano, *Phys. Rev. Lett.* **98**, 147401 (2007).
- [27] J. D. Jackson, *Classical Electrodynamics.*, New York: Wiley, 1999.
- [28] I. D. Mayergoyz and Z. Zhang, *IEEE Trans. Magn.* **43**, No. 4, 1681-1684 (2007).
- [29] J. P. Camden, J. A. Dieringer, J. Zhao, R. P. Van Duyne, *Acc. Chem. Res.* **41**, 1653-1661 (2008).
- [30] K. Kneipp, H. Kneipp, I. Itzkan, R. R. Dasari, M. S. Feld, *J. Phys.: Condens. Matter* **14**, R597-R624 (2002).
- [31] K. Kneipp, Y. Wang, H. Kneipp, L. T. Perelman, I. Itzkan, R. R. Dasari, M. S. Feld, *Phys. Rev. Lett.* **78**, 1667-1670 (1997).
- [32] S. Nie, S. R. Emory, *Science* **275**, 1102-1106 (1997).

- [33] H. X. Xu, E. J. Bjerneld, M. Kall, L. Borjesson, *Phys. Rev. Lett.* **83**, 4357-4360 (1999).
- [34] A. Weiss, G. Haran, *J. Phys. Chem. B* **105**, 12348-12354 (2001).
- [35] J. P. Camden, J. A. Dieringer, Y. M. Wang, D. J. Masiello, L. D. Marks, G. C. Schatz, R. P. Van Duyne, *J. Am. Chem. Soc.* **130**, 12616-12617 (2008).
- [36] J. A. Dieringer, R. B. Lettan, K. A. Scheidt, R. P. Van Duyne, *J. Am. Chem. Soc.* **129**, 16249-16256 (2007).
- [37] E. Blackie, E. C. Le Ru, M. Meyer, M. Timmer, B. Burkett, P. Northcote, P. G. Etchegoin, *Phys. Chem. Chem. Phys.* **10**, 4147-4153 (2008).
- [38] W. Li, P. H. C. Camargo, L. Au, Q. Zhang, M. Rycenga, Y. Xia, *Angew. Chem., Int. Ed.* **49**, 164-168 (2010).
- [39] C. E. Talley, J. B. Jackson, C. Oubre, N. K. Grady, C. W. Hollars, S. M. Lane, T. R. Huser, P. Nordlander, N. J. Halas, *Nano Lett.* **5**, 1569-1574 (2005).
- [40] P. H. C. Camargo, M. Rycenga, L. Au, Y. Xia, *Angew. Chem., Int. Ed.* **48**, 2180-2184 (2009).
- [41] D. -S. Kim, J. Heo, S. -H. Ahn, S. W. Han, W. S. Yun, Z. H. Kim, *Nano Lett.* **9**, 3619-3625 (2009).
- [42] S. C. Yang, H. Kobori, C. L. He, M. H. Lin, Y. H. Chen, C. C. Li, M. Kanehara, S. Gwo, *Nano Lett.* **10**, 632-637 (2010).
- [43] H. Wei, F. Hao, Y. Z. Huang, W. Z. Wang, P. Nordlander, H. X. Xu, *Nano Lett.* **8**, 2497-2502 (2008).
- [44] P. H. C. Camargo, C. M. Cobley, M. Rycenga, Y. Xia, *Nanotechnology* **20**, 434020 (2009).
- [45] T. J. Davis, D. E. Gómez, K. C. Vernon, *Phys. Rev. B* **81**, 045432 (2010)
- [46] A. D. McFarland, M. A. Young, J. A. Dieringer, R. P. Van Duyne, *J. Phys. Chem. B* **109**, 11279-11285 (2005).
- [47] K. M. Mayer, F. Hao, S. Lee, P. Nordlander, J. H. Hafner, *Nanotechnology* **21**, 255503 (2010).

- [48] P. H. C. Camargo, L. Au, M. Rycenga, W. Y. Li, Y. Xia, *Chem. Phys. Lett.* **484**, 304-308 (2010).
- [49] E. C. Le Ru, E. Blackie, M. Meyer, P. G. Etchegoin, *J. Phys. Chem. C* **111**, 13794-13803 (2007).
- [50] D. N. P. Murthy, M. Xie, R. Jiang, *Weibull Models*, John Wiley and Sons, Inc.: Hoboken, NJ (2004).
- [51] H. Rinne, *Weibull Distribution: A Handbook*, CRC Press: Boca Raton, FL (2008).
- [52] C. D. Stanciu, F. Hansteen, A. V. Kimel, A. Kirilyuk, A. Tsukamoto, A. Itoh, and Th. Rasing, *Phys. Rev. Lett.* **99**, 047601 (2007).
- [53] A. I. Kirilyuk, A. V. Kimel, and Th. Rasing, *IEEE Trans. Magn.* **44**, No. 7, 1905-1910 (2008).
- [54] Y. Hashimoto, S. Kobayashi, and H. Munekata, *Phys. Rev. Lett.* **100**, 067202 (2008).
- [55] A. Rebei and J. Hohlfeld, *Phys. Lett. A* **372**, 1915-1918 (2008).
- [56] Y. Zhang and J. Bai, *Phys. Lett. A* **372**, 6294-6297 (2008).
- [57] K. Vahaplar, A. M. Kalashnikova, A. V. Kimel, D. Hinzke, U. Nowak, R. Chantrell, A. Tsukamoto, A. Itoh, A. Kirilyuk, and Th. Rasing, *Phys. Rev. Lett.* **103**, 117201 (2009).
- [58] Y. Zhang, Y. Okuno, and X. Xu, *Optik* **121**, 2062-2066 (2010).
- [59] Z. Jin, H. Ma, D. Li, G. Ma, M. Wang, and C. Zhao, *J. Appl. Phys.* **109**, 073109 (2011).
- [60] R. Hertel, *J. Magn. Magn. Mater.* **303**, L1-L4 (2006).
- [61] I. D. Mayergoyz, Z. Zhang, P. McAvoy, G. Lang, D. Bowen, C. Krafft, *J. Appl. Phys.* **105**, 07B904 (2009).
- [62] W. E. Byerly, *An elementary treatise on Fourier's series and spherical, cylindrical, and ellipsoidal harmonics, with applications to problems in mathematical physics*, Boston: Ginn Company, 1893.

- [63] C. F. Bohren and D. R. Huffman, *Absorption and Scattering of Light by Small Particles*. (New York: Wiley, 1983).
- [64] L. D. Landau, E. M. Lifschitz, *Electrodynamics of Continuous Media, 2nd ed.*, (Oxford: Pergamon Press, 1984).
- [65] I. D. Mayergoyz, D. R. Fredlkin, and Z. Zhang, *Phys. Rev. B* **72**, 155412 (2005).
- [66] N. Hooshmand, P. K. Jain, and M. A. El-Sayed, *J. Phys. Chem. Lett.* **2**, 374-378 (2011).
- [67] E. W. Hobson, *The Theory of Spherical and Ellipsoidal Harmonics*, Cambridge [Eng.] The University Press, 1931.
- [68] P. M. Morse, H. Feshbach, *Methods of Theoretical Physics*, vol. 1 and 2, McGraw-Hill, New York, 1953.
- [69] P. L. Lu and S. H. Charap, *J. Appl. Phys.* **75**, 5768-5770 (1994).
- [70] D. Weller and A. Moser, *IEEE Trans. Magn.* **35**, 4423-4439 (1999).
- [71] M. H. Kryder *et al.*, *Proc. IEEE* **96**, 1810-1835 (2008).
- [72] T. W. McDaniel, *J. Phys.: Condens. Matter* **17**, R315 (2005).
- [73] H. F. Hamann, Y. C. Martin, and H. K. Wickramasinghe, *Appl. Phys. Lett.* **84**, 810 (2004).
- [74] W. A. Challener, T. W. McDaniel, C. C. Mihalcea, K. R. Mountfield, K. Pelhos, and I. K. Sendur, *Jpn. J. Appl. Phys., Part 1* **42**, 981 (2003).
- [75] F. Tawa, S. Hasegawa, and W. Odajima, *J. Appl. Phys.* **101**, 09H503 (2007).
- [76] W. A. Challener, *et al.*, *Nature Photonics*, Vol. **3**, 220 (2009).
- [77] C. Peng, *J. Appl. Phys.*, Vol. **112**, 043108 (2012).
- [78] N. Zhou, E. C. Kinzel, and X. Xu, *Appl. Optics* **50**, No. 31 (2011).
- [79] Z. Zhang and I. D. Mayergoyz, *J. Appl. Phys.* **103**, 07F510 (2008).
- [80] A. V. Itagi, D. D. Stancil, J. A. Bain, and T. E. Schlesinger, *Appl. Phys. Lett.*, vol. **83**, 4474-4476 (2003).

- [81] K. Endur, W. Challener, and C. Peng, *J. Appl. Phys.*, vol. 96, 2743-2752 (2004).
- [82] Y. C. Chen, J. Y. Fang, C. H. Tien, and H. P. D. Shieh, *Opt. Lett.*, vol. 31, 655-657 (2006).
- [83] E. X. Jin and X. Xu, *Appl. Phys. Lett.*, vol. 86, 111106 (2005).
- [84] K. Sendur, W. Challener, and C. Peng, *J. Appl. Phys.*, vol. 96, No. 5, 2743-2752 (2004).
- [85] M. H. Kryder, E. C. Gage, T. W. McDaniel, W. A. Challener, R. E. Rottmayer, G. Ju, Y. Hsia, and M. F. Erden, *Proc. IEEE*, Vol. 96, No. 11, 1810-1835 (2008).
- [86] B. Xu, Y. T. Toh, C. W. Chia, J. Li, J. Zhang, K. Ye, and C. An, *IEEE Trans. Magn.*, Vol. 48, No. 5, 1789-1793 (2012).
- [87] I. D. Mayergoyz, Z. Zhang, and G. Miano, *Phys. Rev. Lett.* 98, 147401 (2007).
- [88] P. B. Johnson and R. W. Christy, *Phys. Rev. B* 6, 4370 (1972).
- [89] I. D. Mayergoyz, and Z. Zhang, *IEEE Trans. Magn.*, Vol. 43, No. 4, 1681-1684 (2007).
- [90] Ouyang, F.; Isaacson, M. *Philos. Mag. B* **1989**, 60, 481-492.
- [91] Ouyang, F.; Isaacson, M. *Ultramicroscopy* **1989**, 31, 345-350.
- [92] Fredkin, D. R.; Mayergoyz, I. D. Resonance Behavior of Dielectric Objects (Electrostatic Resonances). *Phys. Rev. Lett.* **2003**, 91, 253902.
- [93] Mayergoyz, I. D.; Fredkin, D. R.; Zhang, Z. Electrostatic (Plasmon) Resonances in Nanoparticles. *Phys. Rev. B* **2005**, 72, 155412.
- [94] Bohren, C. F.; Huffman, D. R. *Absorption and Scattering of Light by Small Particles*, John Willy, New York, 1983.
- [95] Myroshnychenko, V.; Rodriguez-Fernandez, J.; Pastoriza-Santos, I.; Funston, A. M.; Novo, C.; Mulvaney, P.; Liz-Marzan, L. M.; García de Abajo, F. J. *Chem. Soc. Rev.* **2008**, 37, 1792-1805.
- [96] Aizpurua, J.; Hanarp, P.; Sutherland, D. S.; Käll, M.; Bryant, G. W.; García de Abajo, F. J. Optical Properties of Gold Nanorings. *Phys. Rev. Lett.* **2003**, 90, 057401.

- [97] Sherry, L. J.; Chang, S. H.; Schatz, G. C.; Van Duyne, R. P.; Wiley, B. J.; Xia, Y. N. Localized surface plasmon resonance spectroscopy of single silver nanocubes. *Nano Lett.* **2005**, 5, 2034-2038.
- [98] Jackson, J. D. *Classical Electrodynamics*, John Wiley, New York, 1999.
- [99] Sun, Y.; Xia, Y. Shape-Controlled Synthesis of Gold and Silver Nanoparticles. *Science* **2002**, 298, 2176.
- [100] Tao, A.; Sinsersuksakul, P.; Yang, P. Polyhedral Silver Nanocrystals with Distinct Scattering Signatures. *Angewandte Chemie International Edition* **2006**, 45, 4597-4601.
- [101] Zhang, Q.; Li, W.; Moran, C.; Wen, L.; Chen, J.; Xia, Y. Facile Synthesis of Ag Nanocubes of 30 to 70 nm in Edge Length with CF_3COOAg as a Precursor. *Chem. Eur. J.* **2010**, 16, 10234-10239.
- [102] Zhang, Q.; Li, W.; Moran, C.; Zeng, J.; Chen, J.; Wen, L.; Xia, Y. Seed-Mediated Synthesis of Ag Nanocubes with Controllable Edge Lengths in the Range of 30-200 nm and Comparison of Their Optical Properties. *J. Am. Chem. Soc.* **2010**, 132, 11372-11378.
- [103] Kelly, K. L.; Coronado, E.; Zhao, L. L.; Schatz, G. C. The optical properties of metal nanoparticles: The influence of size, shape, and dielectric environment. *J. Phys. Chem. B* **2003**, 107, 668-677.
- [104] Fuch, R. Theory of the Optical Properties of Ionic Crystal Cubes. *Phys. Rev. B* **1975**, 11, 1732-1740.
- [105] Zhang, S.; Bao, K.; Halas, N. J.; Xu, H.; Nordlander, P. Substrate-Induced Fano Resonances of A Plasmonic Nanocube: A Route to Increased-Sensitivity Localized Surface Plasmon Resonance Sensors Revealed. *Nano Lett.* **2011**, 11, 1657-1663.
- [106] Cortie, M. B.; Liu, F.; Arnold, M. D.; Niidome, Y. Multimode Resonances in Silver Nanocuboids. *Langmuir* **2012**, 28, 9103-9112.
- [107] Grillet, N.; Manchon, D.; Bertorelle, F.; Bonnet, C.; Broyer, M.; Cottancin, E.; Lerme, J.; Hillenkamp, M.; Pellarin, M. Plasmon Coupling in Silver Nanocube Dimers: Resonance Splitting Induced by Edge Rounding. *ACS Nano* **2011**, 5, 9450-9462.
- [108] McMahon, J. M.; Wang, Y.; Sherry, L. J.; Van Duyne, R. P.; Marks, L. D.; Gray, S. K.; Schatz, G. C. Correlating the Structure, Optical Spectra, and

- Electrodynamics of Single Silver Nanocubes. *J. Phys. Chem. C* **2009**, 113, 2731-2735.
- [109] McLellan, J. M.; Siekkinen, A.; Chen, J. Y.; Xia, Y. N. Comparison of the surface-enhanced Raman scattering on sharp and truncated silver nanocubes. *Chem. Phys. Lett.* **2006**, 427, 122-126.
- [110] Sosa, I. O.; Noguez, C.; Barrera, R. G. Optical properties of metal nanoparticles with arbitrary shapes. *J. Phys. Chem. B* **2003**, 107, 6269-6275.
- [111] Mayergoyz, I. D.; Zhang, Z.; Miano, G. Analysis of Dynamics of Excitation and Dephasing of Plasmon Resonance Modes in Nanoparticles. *Phys. Rev. Lett.* **2007**, 98, 147401.
- [112] Lee, S. Y.; Hung, L.; Lang, G. S.; Cornett, J. E.; Mayergoyz, I. D.; Rabin, O. Dispersion in the SERS Enhancement *ACS Nano* **2010**, 4, 5763-5772.
- [113] Johnson, P. B.; Christy, R. W. Optical-Constants of Noble Metals. *Phys. Rev. B* **1972**, 6, 4370-4379.
- [114] Gao, B.; Arya, G.; Tao, A. R. Self-Orienting Nanocubes for the Assembly of Plasmonic Nanojunctions. *Nature Nanotech.* **2012**, 7, 433-437.
- [115] N. B. Colthup, L. H. Daly, and S. E. Wiberley, *Introduction to Infrared and Raman Spectroscopy*, 3rd ed. (Academic Press, New York, 1990).
- [116] S. Nie and S. R. Emory, *Science* (Washington, D. C.) **275**, 1102-1106 (1997).
- [117] K. Kneipp, Y. Wang, H. Kneipp, L. T. Perelman, I. Itzkan, R. R. Dasari and M. S. Feld, *Phys. Rev. Lett.* **78**, 1667-1670 (1997).
- [118] K. L. Wustholz, A-I. Henry, J. M. Bingham, S. L. Kleinman, R. G. Freeman, M. J. Natan, R. P. Van Duyne, *Proceedings of SPIE-The International Society for Optical Engineering*, 7394-739403 (2009).
- [119] J. A. Dieringer, K. L. Wustholz, D. J. Masiello, J. P. Camden, S. L. Kleinman, G. C. Schatz, R. P. Van Duyne, *J. Am. Chem. Soc.*, **131**, 849-854 (2009).
- [120] J. A. Dieringer, R. B. Lettan II, K. A. Scheidt, and R. P. Van Duyne, *J. Am. Chem. Soc.*, **129**, 16249-16256 (2007).
- [121] S. L. Kleinman, E. Ringe, N. Valley, K. L. Wustholz, E. Phillips, K. A. Scheidt, G. C. Schatz, and R. P. Van Duyne, *J. Am. Chem. Soc.*, **133**, 4115-4122 (2011).